



UNIVERSITÄT  
BAYREUTH



D I S S E R T A T I O N

**Structural, electronic and dynamical  
properties of H-bonded systems  
at high pressure**

zur Erlangung des akademischen Grades eines  
Doktors der Naturwissenschaften (Dr. rer. nat.)

in der Bayreuther Graduiertenschule für  
Mathematik und Naturwissenschaften  
(BayNAT)  
der Universität Bayreuth

vorgelegt von

**Florian Trybel**

aus Hof  
Bayreuth, 2020



This doctoral thesis was prepared at the Bavarian Research Institute of Experimental Geochemistry and Geophysics (BGI) at the University of Bayreuth from August 2017 until June 2020 and was supervised by PD Dr. Gerd Steinle-Neumann.

This is a full reprint of the thesis submitted to obtain the academic degree of Doctor of Natural Sciences (Dr. rer. nat.) and approved by the Bayreuth Graduate School of Mathematical and Natural Sciences (BayNAT) of the University of Bayreuth.

Date of submission: 2 July 2020

Date of defence: 18 August 2020

Acting director: Prof. Dr. Markus Lippitz

Doctoral committee:

PD Dr. Gerd Steinle-Neumann	(Reviewer)
Prof. Dr. Dr. h.c. Ronald Redmer	(Reviewer)
Prof. Dr. Gergor Golabek	(Chairman)
PD Dr. Catherine McCammon	(Reviewer)



## Summary

Investigating hydrogen bearing phases is experimentally and theoretically challenging, but knowledge about their properties, especially at elevated pressures, is key for understanding a variety of geophysical processes as well as for the development of technical materials with, e.g. superconducting properties. Two classes of hydrogen bearing phases, water ice and transition metal hydrides are investigated and compressional, electronic and dynamical properties are explored in the current thesis:

The recent discovery of an ice-VII inclusion in a diamond from the Earth's mantle highlights the importance of this high-pressure phase of water for planetary interiors beyond the icy satellites of Jupiter and Saturn in our solar system, and potentially H<sub>2</sub>O-dominated exosolar planets. At room temperature, water crystallizes as ice-VII at pressures above 2 GPa in a cubic structure, based on a body-centered cubic arrangement of oxygens with two possible proton positions along the diagonal O-O direction that are occupied randomly, but assumed to follow the ice-rules. With increasing pressure, the hydrogen bond undergoes a continuous symmetrization to form ice-X. In ice-VII a double-well potential along the O-O direction can be found under correlated proton movement changing significantly under compression. This double-well potential provides the basis for proton dynamics. Although numerous studies have investigated the properties at high pressure, no consensus on the symmetrization pressure has emerged.

In the first part of this thesis, the ice-VII – ice-X phase transition, related proton dynamics and changes in the compressibility are investigated computationally and experimentally at the pressure of planetary interiors. Using a density-functional-theory-based approach, the symmetrization and proton dynamics in ice-VII are explored. The pressure-dependent potential seen by the proton is directly sampled, and the related proton dynamics is calculated by solving the Schrödinger equation for a wave packet in these potentials. A continuous transition from double- to single-well character over the pressure range of 2 to 130 GPa is found, accompanied by a pressure-dependence of the proton dynamics, in agreement with Nuclear Magnetic Resonance (NMR) experiments.

The transition is furthermore studied by synchrotron time-resolved X-ray diffraction (XRD) measurements in dynamic Diamond Anvil Cell (dDAC) experiments, reaching pressures of up to 180 GPa at room temperature. The H<sub>2</sub>O sample is continuously compressed with compression rates in the order of GPa/s in a piezo-driven dDAC, and diffraction patterns are collected with a detector providing a sampling rate in the MHz regime. This dense pressure-coverage permits to directly derive the bulk modulus from the obtained pressure-

volume data without the necessity of choosing an analytical form for the equation-of-state. Three major changes in the compression behavior in the ranges of 35-45, 50-55 and 90-110 GPa are found, in perfect agreement with the computational results, showing that proton dynamics influences the high-pressure compressibility of H<sub>2</sub>O and that these changes can be resolved in XRD measurements.

In recent years, metal hydride systems gained scientific interest due to their potential as hydrogen storage and high-temperature superconducting materials. Still, metal hydrides continue to be enigmatic due to the highly variable metal-hydrogen bond. In the second part of this thesis the metal hydride systems Fe-H and Cu-H are studied at pressures of up to 200 GPa using high-pressure NMR spectroscopy and XRD experiments interpreted on the basis of *ab-initio* electronic structure calculations.

NMR experiments as well as calculated electronic densities-of-state show a distinct deviation from ideal metallic behavior in cubic FeH between 64 and 110 GPa. The calculation of the electron localization functions suggests the formation of an intercalating sublattice of electron density connecting the hydrogens in this pressure-range and a related onset of hydrogen-hydrogen interaction at an average H-H distance ( $r_{\text{HH}}$ ) of 2.4 Å, much larger than previously thought. Furthermore, the atomic and electronic structures of Cu<sub>2</sub>H and CuH have been investigated by high-pressure NMR spectroscopy, XRD and *ab-initio* calculations. Experiments and computations show a similar deviation from ideal metallic behavior in Cu<sub>2</sub>H, suggesting an enhancement of H-H interactions at  $r_{\text{HH}}$  coinciding with the distances at which the same effect is found in FeH. Therefore, the effect seems to be dominantly controlled by  $r_{\text{HH}}$ , and only weakly by the metallic host lattice. Additionally, NMR line shape analysis, supported by the results of molecular dynamics simulations, shows a high proton mobility in Cu<sub>2</sub>H and FeH at elevated pressure.

Comparing the features of Cu<sub>2</sub>H and FeH suggests that deviations from Fermi gas behavior, formation of a hydrogen network and high proton mobility could be common features of metal hydrides.

## Zusammenfassung

Die Untersuchung von wasserstoffhaltigen Verbindungen ist sowohl experimentell als auch theoretisch herausfordernd, aber die Kenntnis ihrer Eigenschaften, insbesondere bei erhöhten Drücken, ist der Schlüssel zum Verständnis einer Vielzahl geophysikalischer Prozesse, sowie zur Entwicklung technischer Materialien mit z.B. supraleitenden Eigenschaften. Zwei Klassen wasserstoffhaltiger Phasen, H<sub>2</sub>O-Eis und Übergangsmetallhydride werden im Rahmen dieser Arbeit betrachtet und kompressive, elektronische und dynamische Eigenschaften untersucht:

Die kürzliche Entdeckung eines Eis-VII-Einschlusses in einem Diamanten aus dem Erdmantel unterstreicht die Bedeutung dieser Hochdruckphase für den Aufbau und die Entwicklung des Inneren der Planeten jenseits der eisigen Satelliten von Jupiter und Saturn in unserem Sonnensystem und möglichen H<sub>2</sub>O-dominierten exosolaren Planeten. Bei Raumtemperatur kristallisiert Wasser bei Drücken über 2 GPa als Eis-VII in einer kubischen Struktur, basierend auf einem raumzentrierten Sauerstoff-Gitter mit zwei möglichen Protonenpositionen entlang der diagonalen O-O Richtung, die zufällig, aber den Eisregeln folgend, besetzt sind. Mit zunehmendem Druck unterliegt die Wasserstoffbindung einer kontinuierlichen Symmetrisierung und geht in die Eis-X Phase über. In Eis-VII existiert ein Doppelmuldenpotential entlang der O-O-Richtung unter korrelierter Protonenbewegung, das eine signifikante Kompressionsabhängigkeit aufweist und die Grundlage für eine druckabhängige Protonendynamik bildet. Obwohl zahlreiche Studien die Eigenschaften von Hochdruck-H<sub>2</sub>O-Eis untersucht haben, hat bis jetzt kein allgemeiner Konsens im Hinblick auf den Symmetrisierungsdruck entwickelt.

Im ersten Teil dieser Arbeit werden der Eis-VII - Eis-X Phasenübergang, die damit verbundene Protonendynamik sowie Änderungen der Kompressibilität unter planetaren Drücken numerisch sowie experimentell untersucht. Unter Verwendung eines auf Dichtefunktionaltheorie (DFT) basierenden Ansatzes werden die Symmetrisierung und Protonendynamik in Eis-VII erforscht. Dazu wird das druckabhängige Potential, in dem das Proton sitzt, durch dessen Verschiebung entlang der O-O Diagonale bestimmt und die zugehörige Protonendynamik berechnet, indem die Schrödinger-Gleichung für ein Wellenpaket im berechneten eindimensionalen Potential gelöst wird. Die Berechnungen zeigen einen kontinuierlichen Übergang von einem Doppel- zu einem Einzelmuldenpotential über einen Druckbereich von 2 bis 130 GPa und eine Druckabhängigkeit der Protonendynamik in Übereinstimmung mit der Analyse von Kernspinresonanzexperimenten (NMR).

Des Weiteren wird der Übergang durch zeitaufgelöste Synchrotron Röntgenbeugung

(XRD) in dynamischen Diamantstempelzellen (dDAC) untersucht, bei denen bei Raumtemperatur Drücke von bis zu 180 GPa erreicht werden. Die H<sub>2</sub>O-Probe wird kontinuierlich mit Kompressionsraten in der Größenordnung von GPa/s in einer piezogesteuerten dDAC komprimiert und Beugungsmuster mit einer Abtastrate im MHz-Bereich detektiert. Diese hohe Druckauflösung ermöglicht es, den isothermen Kompressionsmodul direkt aus den Druck-Volumen-Daten zu berechnen, ohne dass eine analytische Form für die Zustandsgleichung angenommen werden muss. Drei wesentliche Änderungen des Kompressionsverhaltens in den Druckbereichen 35-45, 50-55 und 90-110 GPa werden in Übereinstimmung mit den Berechnungsergebnissen gefunden und zeigen, dass die Protonendynamik die Kompressibilität von H<sub>2</sub>O beeinflusst und dass diese Änderungen mit Röntgenbeugung aufgelöst werden können.

In den letzten Jahren haben Metallhydridsysteme aufgrund ihres Potenzials als Wasserstoffspeicher und Hochtemperatur-Supraleiter großes wissenschaftliches Interesse erlangt. Dennoch sind die Hochdruckeigenschaften von Metallhydriden aufgrund der hochvariablen Metall-Wasserstoff-Bindung weiterhin nicht ausreichend verstanden. Im zweiten Teil dieser Arbeit werden die Metallhydridsysteme Fe-H und Cu-H bei Drücken von bis zu 200 GPa unter Verwendung von NMR- und XRD-Experimenten untersucht, die auf der Grundlage von DFT-basierten Berechnungen der elektronischen Struktur ausgewertet werden.

NMR-Experimente sowie berechnete elektronische Zustandsdichten zeigen eine deutliche Abweichung von idealem metallischem Verhalten in kubischem FeH zwischen 64 und 110 GPa. Die Berechnung der elektronischen Lokalisierungsfunktion legt die Bildung eines interkalierenden Untergitters der Elektronendichte nahe, das die Wasserstoffatome in diesem Druckbereich verbindet, und einen damit verbundenen Beginn von Wasserstoff-Wasserstoff-Wechselwirkungen bei einem durchschnittlichen H-H Abstand ( $r_{\text{HH}}$ ) von 2,4 Å, wesentlich größer als bisher angenommen wurde. Darüber hinaus wurde die räumliche und elektronische Struktur von Cu<sub>2</sub>H und CuH mit Hilfe von NMR-Spektroskopie, XRD- und *ab-initio* Berechnungen untersucht. NMR Experimente sowie Berechnungen zeigen eine Abweichung von idealem metallischem Verhalten in Cu<sub>2</sub>H bei gleichem  $r_{\text{HH}}$  wie in FeH. Daher scheint die Abweichung dominant durch  $r_{\text{HH}}$  und nur schwach durch das metallische Wirtsgitter gesteuert zu werden. Zusätzlich zeigt eine NMR-Linienformanalyse, die durch die Ergebnisse von Molekulardynamiksimulationen gestützt wird, eine hohe Protonenmobilität in Cu<sub>2</sub>H und FeH. Ein Vergleich der Phänomene in Cu<sub>2</sub>H und FeH legt nahe, dass Abweichungen von idealem metallischem Verhalten, die Bildung eines Netzwerks erhöhter Elektronendichte zwischen den Wasserstoffen und eine hohe Protonenmobilität gemeinsame Merkmale von Metallhydriden sein könnten.





# Contents

<b>1</b>	<b>Scientific Motivation</b>	<b>1</b>
1.1	H <sub>2</sub> O Ice . . . . .	2
1.2	Transition Metal Hydrides . . . . .	4
<b>2</b>	<b>Theory &amp; Methods</b>	<b>11</b>
2.1	Density Functional Theory . . . . .	12
2.2	Lattice & Molecular Dynamics . . . . .	15
<b>3</b>	<b>Experimental Techniques</b>	<b>21</b>
3.1	The synergy of experiment and simulation . . . . .	22
3.2	The Diamond Anvil Cell . . . . .	23
3.3	Nuclear Magnetic Resonance Spectroscopy . . . . .	25
3.4	X-Ray Diffraction . . . . .	28
<b>4</b>	<b>Synopsis</b>	<b>35</b>
4.1	High-Pressure H <sub>2</sub> O Ice . . . . .	37
4.1.1	Proton Dynamics in High-Pressure Ice-VII . . . . .	37
4.1.2	Ice-VII – ice-X transition studied by time-resolved XRD in a dDAC . . . . .	43
4.1.3	Summary & Outlook . . . . .	48
4.2	Transition Metal Hydrides . . . . .	49
4.2.1	Pressure-Induced Hydrogen-Hydrogen Interaction in FeH . . . . .	49
4.2.2	Proton Mobility in Metallic Copper Hydride . . . . .	53
4.2.3	Summary & Outlook . . . . .	57
<b>5</b>	<b>Manuscripts</b>	<b>63</b>
5.1	Proton Dynamics in High-Pressure Ice-VII . . . . .	65
5.2	Ice-VII - ice-X transition studied by time-resolved XRD in a dDAC . . . . .	81
5.3	Pressure-Induced Hydrogen-Hydrogen Interaction in FeH . . . . .	95
5.4	Proton Mobility in Metallic Copper Hydride . . . . .	105



## Chapter 1

# Scientific Motivation

Hydrogen is the most abundant element in the universe [50], but despite its overwhelming amount, a deep understanding of the physical properties of pure hydrogen as well as hydrogen bearing compounds has not yet been attained. Similarly, simple hydrides are not fully understood and hydrogen itself is, especially at elevated pressures ( $P$ ), subject of considerable scientific endeavours [e.g. 4, 11, 40] and controversy [13, 33, 14]. Although the complexity of hydrogen-bearing phases is astonishing in itself, it is even more interesting, that the physical properties of water, “[...] the driving force of all nature ” as Leonardo da Vinci [44] already recognised, are yet not fully understood. Studying hydrogen-bearing phases is - in general - experimentally challenging at high  $P$ , prevalent for planetary and stellar interiors, as diffusion of hydrogen in the diamond anvils and related structural weakening can lead to early diamond breaking [35], a reaction with the gasket material or, e.g., in the case of electrical resistivity measurements with the electrodes, can contaminate the sample [18], and the small X-ray cross-section of hydrogen atoms impedes an analysis of structural properties via X-ray diffraction (XRD) [25]. From a theoretical point of view, hydrogen-bearing phases are not easier to deal with, as hydrogen is readily influenced by quantum effects due to its low mass, e.g., zero-point energy and tunnelling, which complicates computations considerably [45].

## 1.1 H<sub>2</sub>O Ice

Water shows a particularly wide variety of phases under compression and elevated temperatures ( $T$ ) [52, 48, 1, 20]. Ice-VII and -X are especially interesting in the geophysical scope of this thesis, as these phases are predicted stable up to planetary interior conditions ( $P \lesssim 200$  GPa and  $T \lesssim 2500$  K [48]) and are suggested to be present in Earth’s mantle, as substantiated recently by the discovery of an ice-VII inclusion in a diamond [53] from the transition zone (410-660 km), in ice giants [48] and the icy satellites of Jupiter and Saturn [42, 15] as well as potentially H<sub>2</sub>O-dominated exosolar planets [55, 22, 58, 43, 27, 41].

Cubic ice-VII (spacegroup  $Pn\bar{3}m$ ) is based on a body centered cubic ( $bcc$ ) arrangement of oxygens with two possible proton positions along the diagonal O-O direction (dOOd) which are occupied randomly (Figure 1.1), but assumed to generally follow the ice-rules [9]. With increasing  $P$ , the O-H $\cdots$ O bond is thought to continuously symmetrize to form ice-X [31, 26]. It is suggested, that the transition can be divided into four stages, with distinct characteristic proton behavior:

- (i) At low pressure ( $P > 2$  GPa), protons are located in one minimum of a double-well potential, such that the ice-rules [9] are satisfied.

- (ii) With increasing  $P$ , the barrier in the double-well potential decreases and protons start to become mobile (in terms of tunnelling), while maintaining an ice-rule conforming ice-VII structure in general terms.
- (iii) Upon further compression, the barrier vanishes and protons are, on average, centered between the two oxygen positions, still showing a high mobility which is decreasing with  $P$ .
- (iv) At very high  $P$ , protons are fully localised at the center position and no mobility is expected.

Associated with these stages are individual phases, named ice-VII, dynamically disordered ice-VII (ice-VII'), dynamically disordered ice-X (ice-X') and static ice-X. Although a significant number of studies investigated this high- $P$  symmetrization experimentally [46, 30, 24, 2, 7, 32, 8, 49, 12, 3, 28] and computationally [10, 31, 21, 34, 54, 26], no consensus on transition pressures has emerged.

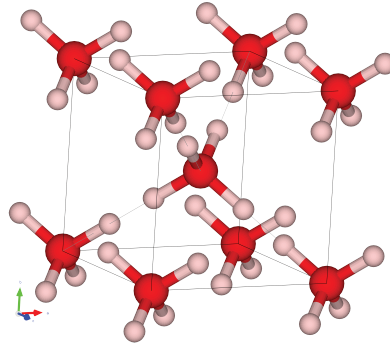


Figure 1.1: Unit cell of ice-VII with all possible hydrogen positions (oxygen in red and hydrogen in white). The diagonal bonds are only occupied by one hydrogen, at one of the two possible positions along the diagonal oxygen-oxygen distance. Visualization with VESTA [39].

Furthermore, knowledge about the elastic properties, in particular the bulk modulus as a function of pressure including a quantification of the influence of the symmetrization has been limited at lower  $P$  and is completely missing at  $P < 100$  GPa, which would provide information for geodynamical simulation of water-dominated exosolar planets and therefore the characterization of astrophysical observations through, e.g., Kepler [29] or Plato [47] satellites.

This thesis provides a theoretical analysis of the character of the double-well potential and the related proton dynamics on the basis of density functional theory calculations and compares the results with recent nuclear magnetic resonance experiments (Section 4.1.1).

Furthermore, dynamic compression experiments in combination with time-resolved X-ray diffraction have been performed in order to understand the compressional behavior of H<sub>2</sub>O ice across the ice-VII – ice-X transition by using a dynamic diamond anvil cell (dDAC) driven by a piezoelectric actuator (Section 4.1.2).

## 1.2 Transition Metal Hydrides

Metal hydrides, first described in 1844 [57], are currently one of the main candidate class for future energy- and hydrogen-storage materials [38] and may furthermore pave the way to room-temperature superconductivity. Based on the hypothesis of Wigner & Huntington [56] that hydrogen may reach a metallic state under high compression, Ashcroft [4] and Ginzburg [23] suggested in the late 1960s, based on BCS theory [6], that hydrogen could exhibit superconducting properties at room temperature. Although considerable scientific efforts have been undertaken, this hypothesis has not yet been substantiated and related research passed almost unnoticed into oblivion as the interest in unconventional superconductivity took over [19].

40 years later, Ashcroft [5] realized that precompressing hydrogen in a metallic host lattice could lead to a class of superconducting metal hydrides with a critical temperature ( $T_C$ ) close to room temperature. This identification led to a renaissance of metal-hydride research and an exemplary synergy between experimental measurements and theoretical predictions, driven by advances in high- $P$  experiments and theory, especially the prediction of electron-phonon coupling. Experimental results followed in 2015, when Drozdov et al. [16] found  $T_C = 203$  K in the sulfur hydride system and later, in 2018, a new record  $T_C = 250$  K was reported in LaH<sub>10</sub> [51, 17] (Further details can be found in the review articles of Pickard et al. [45] and Flores-Livas et al. [19]). Superconducting properties are so far investigated by measuring the electrical resistivity using electrodes (e.g. tantalum [16]) connected to the sample, or the Meissner effect (the expulsion of the magnetic field [37]) below  $T_C$ . These techniques require a complicated DAC setup and a careful sample preparation in order to exclude sample contamination or early diamond failure and are not able to directly probe electronic and dynamic properties of the hydrogen sub-systems. Recent developments in high- $P$  Nuclear Magnetic Resonance (NMR) spectroscopy enable *in-situ* measurements in the DAC, giving direct access to electronic properties ([36], Section 3.3), and in combination with *ab-initio* electronic structure calculations it is possible to analyse the electronic properties of the sub-system and related interaction as well as proton dynamics.

In the second half of this thesis, the electronic properties of compounds in the Fe-H

(Section 4.2.1) and Cu-H (Section 4.2.2) systems, archetype metal hydrides, are investigated with a combination of synchrotron X-ray diffraction, NMR spectroscopy and density functional theory-based calculations.

## Bibliography

- [1] Antsyshkin, D., A. Dunaeva, & O. Kuskov (2010). Thermodynamics of phase transitions in the system ice VI-ice VII-water. *Geochemistry International* 48(7), 633–642.
- [2] Aoki, K., H. Yamawaki, M. Sakashita, & H. Fujihisa (1996). Infrared absorption study of the hydrogen-bond symmetrization in ice to 110 GPa. *Phys. Rev. B* 54, 15673–15677.
- [3] Asahara, Y., K. Hirose, Y. Ohishi, N. Hirao, & M. Murakami (2010). Thermoelastic properties of ice VII and its high-pressure polymorphs: Implications for dynamics of cold slab subduction in the lower mantle. *Earth and Planetary Science Letters* 299(3), 474 – 482.
- [4] Ashcroft, N. W. (1968). Metallic Hydrogen: A High-Temperature Superconductor? *Phys. Rev. Lett.* 21, 1748–1749.
- [5] Ashcroft, N. W. (2004). Hydrogen Dominant Metallic Alloys: High Temperature Superconductors? *Phys. Rev. Lett.* 92, 187002.
- [6] Bardeen, J., L. N. Cooper, & J. R. Schrieffer (1957). Theory of Superconductivity. *Phys. Rev.* 108, 1175–1204.
- [7] Benoit, M., D. Marx, & M. Parrinello (1998). Tunnelling and zero-point motion in high-pressure ice. *Nature* 392, 258–261.
- [8] Benoit, M., A. H. Romero, & D. Marx (2002). Reassigning hydrogen-bond centering in dense ice. *Phys. Rev. Lett.* 89, 145501.
- [9] Bernal, J. D. & R. H. Fowler (1933). A Theory of Water and Ionic Solution, with Particular Reference to Hydrogen and Hydroxyl Ions. *The Journal of Chemical Physics* 1(8), 515–548.
- [10] Bernasconi, M., P. L. Silvestrelli, & M. Parrinello (1998). Ab Initio Infrared Absorption Study of the Hydrogen-Bond Symmetrization in Ice. *Phys. Rev. Lett.* 81, 1235–1238.
- [11] Borinaga, M., I. Errea, M. Calandra, F. Mauri, & A. Bergara (2016). Anharmonic effects in atomic hydrogen: Superconductivity and lattice dynamical stability. *Phys. Rev. B* 93, 174308.
- [12] Caracas, R. (2008). Dynamical Instabilities of Ice X. *Phys. Rev. Lett.* 101, 085502.
- [13] Dias, R. P. & I. F. Silvera (2017a). Observation of the Wigner-Huntington transition to metallic hydrogen. *Science* 355(6326), 715–718.
- [14] Dias, R. P. & I. F. Silvera (2017b). Erratum for the Research Article “Observation of the Wigner-Huntington transition to metallic hydrogen”. *Science* 357(6352).
- [15] Dougherty, M. K. & L. J. Spilker (2018). Review of Saturn’s icy moons following the Cassini mission. *Reports on Progress in Physics* 81, 065901.
- [16] Drozdov, A. P., M. I. Erements, I. A. Troyan, V. Ksenofontov, & S. I. Shylin (2015). Conventional superconductivity at 203 kelvin at high pressures in the sulfur hydride system. *Nature* 525(7567), 73–76.
- [17] Drozdov, A. P., P. P. Kong, V. S. Minkov, S. P. Besedin, M. A. Kuzovnikov, S. Mozaffari, L. Balicas, F. F. Balakirev, D. E. Graf, V. B. Prakapenka, E. Greenberg, D. A. Knyazev, M. Tkacz, & M. I. Erements (2019). Superconductivity at 250 K in lanthanum hydride under high pressures. *Nature* 569(7757), 528–531.
- [18] Erements, M. I., A. P. Drozdov, P. P. Kong, & H. Wang (2019). Semimetallic molecular hydrogen at pressure above 350 GPa. *Nature Physics* 15(12), 1246–1249.
- [19] Flores-Livas, J. A., L. Boeri, A. Sanna, G. Profeta, R. Arita, & M. Erements (2020). A perspective on conventional high-temperature superconductors at high pressure: Methods and materials. *Physics Reports* 856, 1 – 78.

- [20] Fortes, A. D. & M. Choukroun (2010). Phase Behaviour of Ices and Hydrates. *Space Science Reviews* 153(1), 185–218.
- [21] French, M. & R. Redmer (2015). Construction of a thermodynamic potential for the water ices VII and X. *Phys. Rev. B* 91, 014308.
- [22] Fu, R., R. J. O'Connell, & D. D. Sasselov (2009). The interior dynamics of water planets. *The Astrophysical Journal* 708(2), 1326–1334.
- [23] Ginzburg, V. L. (1969). Superfluidity and superconductivity in the universe. *Journal of Statistical Physics* 1(1), 3–24.
- [24] Goncharov, A. F., V. V. Struzhkin, M. S. Somayazulu, R. J. Hemley, & H. K. Mao (1996). Compression of ice to 210 gigapascals: Infrared evidence for a symmetric hydrogen-bonded phase. *Science* 273(5272), 218–220.
- [25] Hammond, C. (2015). *The Basics of Crystallography and Diffraction*. IUCr monographs on crystallography. Oxford University Press.
- [26] Hernandez, J.-A. & R. Caracas (2018). Proton dynamics and the phase diagram of dense water ice. *The Journal of Chemical Physics* 148, 214501.
- [27] Journaux, B., I. Daniel, S. Petitgirard, H. Cardon, J.-P. Perrillat, R. Caracas, & M. Mezourar (2017). Salt partitioning between water and high-pressure ices. implication for the dynamics and habitability of icy moons and water-rich planetary bodies. *Earth and Planetary Science Letters* 463, 36 – 47.
- [28] Klotz, S., K. Komatsu, H. Kagi, K. Kunc, A. Sano-Furukawa, S. Machida, & T. Hattori (2017). Bulk moduli and equations of state of ice-VII and ice-VIII. *Phys. Rev. B* 95, 174111.
- [29] Koch, D. G., W. J. Borucki, G. Basri, N. M. Batalha, T. M. Brown, D. Caldwell, J. Christensen-Dalsgaard, W. D. Cochran, E. Devore, E. W. Dunham, T. N. Gautier, J. C. Geary, R. L. Gilliland, A. Gould, J. Jenkins, Y. Kondo, D. W. Latham, J. J. Lissauer, G. Marcy, D. Monet, D. Sasselov, A. Boss, D. Brownlee, J. Caldwell, A. K. Dupree, S. B. Howell, H. Kjeldsen, S. Meibom, D. Morrison, T. Owen, H. Reitsema, J. Tarter, S. T. Bryson, J. L. Dotson, P. Gazis, M. R. Haas, J. Kolodziejczak, J. F. Rowe, J. E. V. Cleve, C. Allen, H. Chandrasekaran, B. D. Clarke, J. Li, E. V. Quintana, P. Tenenbaum, J. D. Twicken, & H. Wu (2010). Kepler mission design, realized photometric performance, and early science. *The Astrophysical Journal* 713(2), L79–L86.
- [30] Lee, C., D. Vanderbilt, K. Laasonen, R. Car, & M. Parrinello (1993). Ab initio studies on the structural and dynamical properties of ice. *Phys. Rev. B* 47, 4863–4872.
- [31] Lin, L., J. A. Morrone, & R. Car (2011). Correlated Tunneling in Hydrogen Bonds. *Journal of Statistical Physics* 145(2), 365–384.
- [32] Loubeyre, P., R. LeToullec, E. Wolanin, M. Hanfland, & D. Hausermann (1999). Modulated phases and proton centring in ice observed by X-ray diffraction up to 170 GPa. *Nature* 397, 503–506.
- [33] Loubeyre, P., F. Occelli, & P. Dumas (2017). Comment on: Observation of the Wigner-Huntington transition to metallic hydrogen. *arXiv* 1702.07192.
- [34] Lu, X. Z., Y. Zhang, P. Zhao, & S. J. Fang (2011). Vibrational Analysis of the Hydrogen-Bond Symmetrization in Ice. *The Journal of Physical Chemistry B* 115(1), 71–74.
- [35] Mao, H.-k. & R. J. Hemley (1994). Ultrahigh-pressure transitions in solid hydrogen. *Rev. Mod. Phys.* 66, 671–692.
- [36] Meier, T., N. Wang, D. Mager, J. G. Korvink, S. Petitgirard, & L. Dubrovinsky (2017). Magnetic flux tailoring through lens lenses for

- ultrasmall samples: A new pathway to high-pressure nuclear magnetic resonance. *Science Advances* 3(12), eaao5242.
- [37] Meissner, W. & R. Ochsenfeld (1933). Ein neuer Effekt bei Eintritt der Supraleitfähigkeit. *Naturwissenschaften* 21(44), 787–788.
- [38] Mohtadi, R. & S.-i. Orimo (2016). The renaissance of hydrides as energy materials. *Nature Reviews Materials* 2(3), 16091.
- [39] Momma, K. & F. Izumi (2008). VESTA: a three-dimensional visualization system for electronic and structural analysis. *Journal of Applied Crystallography* 41(3), 653–658.
- [40] Monserrat, B., S. E. Ashbrook, & C. J. Pickard (2019). Nuclear magnetic resonance spectroscopy as a dynamical structural probe of hydrogen under high pressure. *Phys. Rev. Lett.* 122, 135501.
- [41] Monteux, J., G. J. Golabek, D. C. Rubie, G. Tobie, & E. D. Young (2018). Water and the Interior Structure of Terrestrial Planets and Icy Bodies. *Space Science Reviews* 214(1), 39.
- [42] Nimmo, F. & R. T. Pappalardo (2016). Ocean worlds in the outer solar system. *Journal of Geophysical Research: Planets* 121, 1378–1399.
- [43] Noack, L., D. Höning, A. Rivoldini, C. Heisteracher, N. Zimov, B. Journaux, H. Lammer, T. V. Hoolst], & J. Bredehöft (2016). Water-rich planets: How habitable is a water layer deeper than on Earth? *Icarus* 277, 215 – 236.
- [44] Pfister, L., H. H. Savenije, & F. Fenicia (2009). Leonardo da vinci’s water theory. *On the origin and fate of water. IAHS Special Publication* 9, 94.
- [45] Pickard, C. J., I. Errea, & M. I. Eremets (2020). Superconducting Hydrides Under Pressure. *Annual Review of Condensed Matter Physics* 11(1), 57–76.
- [46] Polian, A. & M. Grimsditch (1984). New High-Pressure Phase of H<sub>2</sub>O: Ice X. *Phys. Rev. Lett.* 52, 1312–1314.
- [47] Rauer, H., C. Aerts, J. Cabrera, & P. Team (2016). The PLATO Mission. *Astronomische Nachrichten* 337(8-9), 961–963.
- [48] Redmer, R., T. R. Mattsson, N. Nettelmann, & M. French (2011). The phase diagram of water and the magnetic fields of Uranus and Neptune. *Icarus* 211(1), 798 – 803.
- [49] Sanz, E., C. Vega, J. L. F. Abascal, & L. G. MacDowell (2004). Phase Diagram of Water from Computer Simulation. *Phys. Rev. Lett.* 92, 255701.
- [50] Schramm, D. N. & M. S. Turner (1998). Big-bang nucleosynthesis enters the precision era. *Rev. Mod. Phys.* 70, 303–318.
- [51] Somayazulu, M., M. Ahart, A. K. Mishra, Z. M. Geballe, M. Baldini, Y. Meng, V. V. Struzhkin, & R. J. Hemley (2019). Evidence for superconductivity above 260 K in lanthanum superhydride at megabar pressures. *Phys. Rev. Lett.* 122(2), 027001.
- [52] Song, M., H. Yamawaki, H. Fujihisa, M. Sakashita, & K. Aoki (2003). Infrared investigation on ice VIII and the phase diagram of dense ices. *Phys. Rev. B* 68, 014106.
- [53] Tschauner, O., S. Huang, E. Greenberg, V. B. Prakapenka, C. Ma, G. R. Rossman, A. H. Shen, D. Zhang, M. Newville, A. Lanzirrotti, & K. Tait (2018). Ice-VII inclusions in diamonds: Evidence for aqueous fluid in Earth’s deep mantle. *Science* 359(6380), 1136–1139.
- [54] Tsuchiya, J. & T. Tsuchiya (2017). First principles calculation of the elasticity of ice VIII and X. *The Journal of Chemical Physics* 146(1), 014501.
- [55] Valencia, D., D. D. Sasselov, & R. J. O’Connell (2007). Detailed Models of Super-Earths: How Well Can We Infer Bulk Properties? *The Astrophysical Journal* 665(2), 1413–1420.
- [56] Wigner, E. & H. B. Huntington (1935). On the Possibility of a Metallic Modification of Hy-

drogen. *The Journal of Chemical Physics* 3(12), 764–770.

[57] Wurtz, A. (1844). On copper hydride. *Hebdomadaires des Séances de l'Académie des Sciences* 1, 702–704.

[58] Zeng, L. & D. Sasselov (2014). The effect of temperature evolution on the interior structure of H<sub>2</sub>O-rich planets. *The Astrophysical Journal* 784(2), 96.



## Chapter 2

# Theory & Methods

## 2.1 Density Functional Theory

The main theoretical basis of the work performed in this thesis is density functional theory (DFT). The foundation of density functional theory by Hohenberg & Kohn [24] and Kohn & Sham [26] was published in 1964 and 1965, respectively - nearly 80 years after the first suggestion by Ludwig Boltzmann that the energy states of a physical system could be discrete and more than 40 years after the mathematical description of Quantum Mechanics by Heisenberg, Schrödinger, Dirac and others [10] which highlights the long process that was necessary in order to develop a density-based approach to quantum mechanics.

Although Quantum Mechanics was able to describe a variety of phenomena that classical mechanics could not explain (e.g., the Stern Gerlach experiment [16]), scientists realised already in the late 1920s, shortly after the development, that the theory was overwhelmingly complex even for a small number of particles. Therefore, approximations to the wave function description of the Schrödinger Theory were attempted, without major success. The approximations, e.g., Hartree-Fock approximation [21, 14, 35], were unable to give a sufficiently accurate description of many body systems and especially chemical bonding.

On the other hand, Llewellyn Thomas and Enrico Fermi developed an approximation to the quantum mechanical many-body problem [40, 12], asking the question: Is it possible to find an energy-density functional  $E[n]$  with which it is possible to find the ground state energy of a many-body system without the knowledge of the wavefunction  $\Psi$ . While they succeeded in the development of a density-based approximation, their treatment of the kinetic energy was not sensitive to boundary conditions and therefore could not describe important quantization effects. Edward Teller [39] demonstrated that Thomas-Fermi theory was also unable to describe chemical bonding, as the energy of a system would decrease continuously with distance between two nuclei. Therefore, Thomas-Fermi theory was not able to play an important role in the description of solids.

The major breakthrough was the developments by Hohenberg & Kohn [24]. Already in the abstract, they state:

„It is proved that there exists a universal functional of the density,  $F[n(\mathbf{r})]$ , independent of  $v(\mathbf{r})$ , such that the expression  $E \equiv \int v(\mathbf{r})n(\mathbf{r})d^3\mathbf{r} + F[n(\mathbf{r})]$  has as its minimum value the correct ground-state energy associated with  $v(\mathbf{r})$ .“,

and show that the ground-state electron density  $n(\mathbf{r})$  uniquely determines the potential  $v(\mathbf{r})$ , up to an arbitrary constant [6], laying the cornerstone of DFT. In the following year, Kohn & Sham [26] gave a detailed description of the energy density functional and the

practical calculation procedure. The quantum mechanical many-body problem is mapped on to a single-particle problem with an effective potential  $v_{\text{eff}}$ . The functional consists of three parts: (i) the single particle kinetic energy  $T_S[n]$ , (ii) the electrostatic interaction  $E_H[n]$ , named Hartree energy, and (iii) the non-analytical parts of the kinetic energy and the interaction (Fock energy), combined into the exchange-correlation energy  $E_{\text{xc}}[n]$ . The functional is defined as

$$E[n] = T_S[n] + E_H[n] + \int d^3\mathbf{r} n(\mathbf{r})v_{\text{ext}}(\mathbf{r}) + E_{\text{xc}}[n], \quad (2.1a)$$

$$T_S[n] = \sum_{i=1}^N \int d^3\mathbf{r} \phi_i[n](\mathbf{r})^* \left(-\frac{\hbar^2}{2m} \nabla^2\right) \phi_i[n](\mathbf{r}), \quad (2.1b)$$

$$E_H[n] = \frac{e}{2} \int d^3\mathbf{r} \int d^3\mathbf{r}' \frac{n(\mathbf{r})n(\mathbf{r}')}{|\mathbf{r} - \mathbf{r}'|}, \quad (2.1c)$$

where  $v_{\text{ext}}$  is the external potential,  $\phi_j(\mathbf{r})$  are Kohn-Sham single-particle wave functions and the effective potential is defined as

$$v_{\text{eff}}^{KS} = v_{\text{ext}}(\mathbf{r}) + \int \frac{n(\mathbf{r}')}{|\mathbf{r} - \mathbf{r}'|} d\mathbf{r}' + v_{\text{xc}}(\mathbf{r}). \quad (2.2)$$

In order to calculate the ground-state electronic energy of a system consisting of  $N$  electrons with an ionic background,  $N$  single-particle Schrödinger-type equations of the form

$$\left(-\frac{\hbar^2}{2m} \nabla^2 + v_{\text{eff}}^{KS}(\mathbf{r})\right) \phi_j(\mathbf{r}) = \epsilon_j^{KS} \phi_j(\mathbf{r}) \quad (2.3)$$

must be solved, where  $\epsilon_j$  are the respective energy eigenvalues. The Kohn-Sham density is subsequently calculated as

$$n_{\text{KS}}(\mathbf{r}) = \sum_{j=1}^N |\phi_j(\mathbf{r})|^2. \quad (2.4)$$

This system of equations is solved by an iterative solution method with the following self-consistent cycle: (i) Guess a set of  $\phi_{j,k=0}(\mathbf{r})$  in step  $k = 0$ , (ii) calculate  $n_{\text{KS}}(\mathbf{r})$  via (2.4), (iii) calculate  $v_{\text{eff}}^{KS}$  via (2.2), (iv) solve the set of Schrödinger-type Kohn-Sham equations (2.3), (v) check if the energy is sufficiently converged with respect to the chosen convergence criteria. If the energy is not sufficiently converged, go to (ii) with the  $\phi_{j,k}(\mathbf{r})$  replaced by the result of (iv),  $\phi_{j,k+1}(\mathbf{r})$ . If the energy is converged (usually 4 - 200 steps  $k$ ), terminate the cycle. The wave functions  $\phi_{j,k}(\mathbf{r})$  are typically represented as a linear combination of, e.g., Gaussians [41] or in the projector augmented wave formalism (PAW) [5].

The overall complexity of the calculation is to find an appropriate approximation to  $v_{\text{xc}}(\mathbf{r})$  which takes the many-body character of the problem into account. The most com-

mon approximations are the local density approximation (LDA), for which the electronic density is locally approximated as a homogenous electron gas of equal density, [25, 3] and the generalised gradient approximation (GGA), where an additional gradient correction is taken into account, improving total and atomization energy [31, 30] as well as the overbinding found in LDA-based potentials [36, 33].

### Electronic Properties

After charge density and the potential are calculated self-consistently, the full Hamiltonian of the system can be constructed and therefore the electronic band structure and density-of-state of the system calculated from the Hamiltonian with the wave function approximated by, e.g., the PAW expansion. Furthermore it is possible to calculate higher dimensional properties, e.g., the Fermi Energy surface, i.e., the energy surface in reciprocal space, separating occupied from unoccupied electron states, or the electron localisation function (ELF) [4, 34], used in Section 4.2.1. Both can be used to obtain topological information about the electronic properties of the system of interest [20, 9].

The original definition of the ELF by Becke & Edgecombe [4], based on Hartree-Fock theory, builds on a Taylor expansion of the average same-spin pair probability density to measure an electron close to a reference electron with the same spin, but as in DFT pair properties are not explicitly defined, Savin et al. [34] introduced an alternative formulation. In this formulation, the ELF is a measure of the influence of the Pauli kinetic energy density relative to a uniform electron gas of the same density.

Starting with the kinetic energy functional of the Kohn-Sham formalism defined in equation (2.1), it is possible to calculate the kinetic energy density of the non-interacting electrons as  $t_S(r) = \frac{1}{2} \sum_{i=1}^N |\nabla \phi_i(r)|^2$ , which has a lower limit [38] of

$$t_S(r) \geq \frac{1}{8} \frac{|\nabla n(r)|^2}{n(r)}. \quad (2.5)$$

The Pauli kinetic energy is the energy due to a redistribution of electrons by means of the Pauli principle and therefore the kinetic energy density minus its lower limit,

$$t_P(r) = t_S(r) - \frac{1}{8} \frac{|\nabla n(r)|^2}{n(r)}. \quad (2.6)$$

The Pauli kinetic energy does not resolve bonding information, but dividing  $t_P(r)$  by

$t_P^0 = \frac{3}{10}(3\pi^2)^{2/3}n(r)^{5/3}$  of a uniform electron gas leads to

$$ELF = (1 + (t_P/t_P^0)^2)^{-1}, \quad (2.7)$$

which is normalized such that  $ELF=1/2$  corresponds to a homogeneous electron gas-like localization and  $ELF=1$  to perfect localization.

## 2.2 Lattice & Molecular Dynamics

Density functional theory enables not only the calculation of the electronic ground state, but also forces acting on atomic cores via the Hellmann-Feynman theorem [23, 13]. The Hellmann-Feynman theorem states that the derivative of the total energy with respect to a variable is equal to the expectation value of the derivative of the Hamiltonian with respect to the same variable:

$$\frac{dE}{d\lambda} = \langle \psi_\lambda | \frac{d\hat{H}}{d\lambda} | \psi_\lambda \rangle. \quad (2.8)$$

Consequently, it is possible to use the theorem to calculate the forces on particles by calculation of the derivative of energy with respect to a displacement of a particle. With these forces not only the equilibrium geometry of a lattice, but also dynamical properties of a quantum system can be calculated. The ground state energy of a system in combination with the forces acting on the respective atoms can be used to structurally relax the system by displacing the atoms along the forces until the energy is minimal. Alternatively, if one starts with a large set of configurations with randomly chosen [32] or evolutionary modified [19] coordinates, it is possible to search for stable structures at a certain chemical composition and compression [29]. In both cases, the equilibrium structures can then be used for comparison with, e.g., X-ray diffraction patterns (see Section 3.4). Knowing the forces in the system, it is possible to describe the dynamics of the atoms in two distinct ways.

### Lattice Dynamics (LD)

Calculating the forces for a set of configurations with slightly displaced ionic positions, one can calculate the force constant matrix  $\Phi_{n\alpha i, n'\alpha' i'}$ , parametrizing the force on atom  $\alpha$  in direction  $i$  in unit cell  $n$  caused by a displacement of atom  $\alpha'$  in unit cell  $n'$  in direction  $i'$  from which, by applying Hamilton's equations of motion, the ionic eigenmodes can be calculated and thereby vibrational and thermodynamics properties. Two things are especially important: (i) the approximation made for the definition of the force constants determines how well thermodynamic properties are described. For example in the simplest

approximation (quasi-harmonic), the potential defining the forces due to atomic displacement is expanded in a Taylor series and truncated after the second-order term, leading to  $T$ -independent frequencies as well as infinite lifetimes of the quasi particles associated to the excitation of the respective modes (phonons) and, consequently, to an infinite thermal conductivity. Nevertheless, this approximation can be used to include thermal properties in LD calculations at relatively low computational costs as long as the limitations of the approximation are taken into account. In practice, the force constants can be calculated within density functional perturbation theory (DFPT) [18, 17] used for the calculations in the following, or by using the small displacement method [1].

In order to further improve the description, it is possible to include higher order terms, at significantly higher computational costs [11, 37]. Therefore, an appropriate approximation level has to be chosen depending on the problem. The most important advantage of this method is, that quantum mechanical behavior at 0 K is well described and thermodynamic potentials, e.g., Helmholtz ( $F$ ) or Gibbs ( $G$ ) energy of the system are directly accessible in the canonical ( $NVT$ ) or isothermal-isobaric ( $NPT$ ) ensemble, respectively.

### Molecular Dynamics (MD)

The Hellmann-Feynman forces can also be used to apply classical Newtonian equations of motion and calculate the dynamical time ( $t$ ) evolution of a system. From the atomic coordinates at each timestep, the mean-square-displacement

$$\text{MSD}(\tau) = \langle |r_i(t) - r_i(t_0)|^2 \rangle, \quad (2.9)$$

which can be linked to the diffusion coefficient  $D$  by

$$\text{MSD}(\tau) = 6\tau D(\tau), \quad (2.10)$$

where  $\tau = t - t_0$ , and the radial distribution function can be calculated and sub-sequentially linked to structural properties [15]. It is important to note that the quantities calculated from molecular dynamics simulations are in general time averages and the experimental observables are considered to be ensemble averages, which can be assumed to be equal due to the applicability to the ergodic hypothesis [15].

Finite temperature is taken into account by minimizing  $F[n] = E[n] - TS$ , where in this case  $T$  represents the ionic temperature, controlled via a thermostat [28, 2], and  $S$  the entropy [27, 26], giving access to the  $T$ -dependence of properties. Using (uncorrelated) snapshots from the  $T$ -dependent  $t$ -evolution of atomic positions or fluctuation formulas [7],

vibrational [22], elastic [42] and transport [8] (e.g., electronic and thermal conductivity) properties can be calculated. The downside of this approach is that the classical description of the dynamics is strictly valid only above the Debye temperature, when all phonon modes are occupied, hence, quantum mechanical properties at low  $T$  are not taken into account. In addition, Helmholtz and Gibbs energy are not directly accessible as in LD, but require additional thermodynamic integration [15].

## Bibliography

- [1] Alfè, D. (2009). PHON: A program to calculate phonons using the small displacement method. *Computer Physics Communications* 180(12), 2622–2633.
- [2] Andersen, H. C. (1980). Molecular dynamics simulations at constant pressure and/or temperature. *The Journal of Chemical Physics* 72(4), 2384–2393.
- [3] Becke, A. D. (1989). *Density Functional Theories in Quantum Chemistry*, Volume 394, pp. 165–179. American Chemical Society.
- [4] Becke, A. D. & K. E. Edgecombe (1990). A simple measure of electron localization in atomic and molecular systems. *The Journal of Chemical Physics* 92(9), 5397–5403.
- [5] Blöchl, P. E. (1994). Projector augmented-wave method. *Phys. Rev. B* 50, 17953–17979.
- [6] Burke, K. (2012). Perspective on density functional theory. *J. Chem. Phys.* 136, 150901.
- [7] Che, J., T. Çağın, W. Deng, & W. A. Goddard III (2000). Thermal conductivity of diamond and related materials from molecular dynamics simulations. *The Journal of Chemical Physics* 113(16), 6888–6900.
- [8] de Koker, N., G. Steinle-Neumann, & V. Vlček (2012). Electrical resistivity and thermal conductivity of liquid Fe alloys at high P and T, and heat flux in Earth’s core. *Proceedings of the National Academy of Sciences* 109(11), 4070–4073.
- [9] Dugdale, S. B. (2016). Life on the edge: a beginner’s guide to the Fermi surface. *Physica Scripta* 91(5), 053009.
- [10] Edwards, D. A. (1979). The mathematical foundations of quantum mechanics. *Synthese* 42(1), 1–70.
- [11] Errea, I., M. Calandra, & F. Mauri (2014). Anharmonic free energies and phonon dispersions from the stochastic self-consistent harmonic approximation: Application to platinum and palladium hydrides. *Phys. Rev. B* 89, 064302.
- [12] Fermi, E. (1928). Eine statistische Methode zur Bestimmung einiger Eigenschaften des Atoms und ihre Anwendung auf die Theorie des periodischen Systems der Elemente. *Zeitschrift für Physik* 48(1), 73–79.
- [13] Feynman, R. P. (1939). Forces in molecules. *Phys. Rev.* 56, 340–343.
- [14] Fock, V. (1930). Näherungsmethode zur Lösung des quantenmechanischen Mehrkörperproblems. *Zeitschrift für Physik* 61(1), 126–148.
- [15] Frenkel, D. & B. Smit (2002). Chapter 7 - Free Energy Calculations. In D. Frenkel & B. Smit (Eds.), *Understanding Molecular Simulation (Second Edition)*, pp. 167 – 200. Academic Press.
- [16] Gerlach, W. & O. Stern (1922). Der experimentelle Nachweis der Richtungsquantelung im Magnetfeld. *Zeitschrift für Physik* 9(1), 349–352.
- [17] Giannozzi, P., O. Andreussi, T. Brumme, O. Bunau, M. B. Nardelli, M. Calandra, R. Car, C. Cavazzoni, D. Ceresoli, M. Cococcioni, et al. (2017). Advanced capabilities for materials modelling with QUANTUM ESPRESSO. *Journal of Physics: Condensed Matter* 29(46), 465901.
- [18] Giannozzi, P., S. Baroni, N. Bonini, M. Calandra, R. Car, C. Cavazzoni, D. Ceresoli, G. L. Chiarotti, M. Cococcioni, I. Dabo, et al. (2009). QUANTUM ESPRESSO: a modular and open-source software project for quantum simulations of materials. *Journal of Physics: Condensed Matter* 21(39), 395502.
- [19] Glass, C. W., A. R. Oganov, & N. Hansen (2006). USPEX An Evolutionary crystal structure prediction. *Computer Physics Communications* 175(11), 713 – 720.

- [20] Glazyrin, K., L. V. Pourovskii, L. Dubrovinsky, O. Narygina, C. McCammon, B. Hewener, V. Schünemann, J. Wolny, K. Muffler, A. I. Chumakov, W. Crichton, M. Hanfland, V. B. Prakapenka, F. Tasnádi, M. Ekholm, M. Aichhorn, V. Vildosola, A. V. Ruban, M. I. Katsnelson, & I. A. Abrikosov (2013). Importance of Correlation Effects in hcp Iron Revealed by a Pressure-Induced Electronic Topological Transition. *Phys. Rev. Lett.* *110*, 117206.
- [21] Hartree, D. R. (1928). The Wave Mechanics of an Atom with a Non-Coulomb Central Field. Part II. Some Results and Discussion. *Mathematical Proceedings of the Cambridge Philosophical Society* *24*(1), 111–132.
- [22] Hellman, O. & I. A. Abrikosov (2013). Temperature-dependent effective third-order interatomic force constants from first principles. *Phys. Rev. B* *88*, 144301.
- [23] Hellmann, H. (1937). *Einführung in die Quantenchemie*. F. Deuticke.
- [24] Hohenberg, P. & W. Kohn (1964). Inhomogeneous Electron Gas. *Phys. Rev.* *136*, B864–B871.
- [25] Jones, R. O. & O. Gunnarsson (1989). The density functional formalism, its applications and prospects. *Rev. Mod. Phys.* *61*, 689–746.
- [26] Kohn, W. & L. J. Sham (1965). Self-Consistent Equations Including Exchange and Correlation Effects. *Phys. Rev.* *140*, A1133–A1138.
- [27] Mermin, N. D. (1965). Thermal Properties of the Inhomogeneous Electron Gas. *Phys. Rev.* *137*, A1441–A1443.
- [28] Nosé, S. (1984). A unified formulation of the constant temperature molecular dynamics methods. *The Journal of Chemical Physics* *81*(1), 511–519.
- [29] Oganov, A. R., C. J. Pickard, Q. Zhu, & R. J. Needs (2019). Structure prediction drives materials discovery. *Nature Reviews Materials* *4*(5), 331–348.
- [30] Perdew, J. P., K. Burke, & M. Ernzerhof (1996). Generalized Gradient Approximation Made Simple. *Phys. Rev. Lett.* *77*, 3865–3868.
- [31] Perdew, J. P., J. A. Chevary, S. H. Vosko, K. A. Jackson, M. R. Pederson, D. J. Singh, & C. Fiolhais (1993). Erratum: Atoms, molecules, solids, and surfaces: Applications of the generalized gradient approximation for exchange and correlation. *Phys. Rev. B* *48*, 4978–4978.
- [32] Pickard, C. J. & R. J. Needs (2011). Ab initio random structure searching. *Journal of Physics: Condensed Matter* *23*(5), 053201.
- [33] Rappoport, D., N. R. Crawford, F. Furche, & K. Burke (2011). Approximate density functionals: which should I choose? *Encyclopedia of Inorganic and Bioinorganic Chemistry*.
- [34] Savin, A., O. Jepsen, J. Flad, O. K. Andersen, H. Preuss, & H. G. von Schnering (1992). Electron localization in solid-state structures of the elements: the diamond structure. *Angewandte Chemie International Edition in English* *31*(2), 187–188.
- [35] Slater, J. C. (1928). The Self Consistent Field and the Structure of Atoms. *Phys. Rev.* *32*, 339–348.
- [36] Stixrude, L., R. E. Cohen, & D. J. Singh (1994). Iron at high pressure: Linearized-augmented-plane-wave computations in the generalized-gradient approximation. *Phys. Rev. B* *50*, 6442–6445.
- [37] Tadano, T., Y. Gohda, & S. Tsuneyuki (2014). Anharmonic force constants extracted from first-principles molecular dynamics: applications to heat transfer simulations. *Journal of Physics: Condensed Matter* *26*(22), 225402.
- [38] Tal, Y. & R. F. W. Bader (1978). Studies of the energy density functional approach. I. Kinetic energy. *International Journal of Quantum Chemistry* *14*(S12), 153–168.

- [39] Teller, E. (1962). On the Stability of Molecules in the Thomas-Fermi Theory. *Rev. Mod. Phys.* *34*, 627–631.
- [40] Thomas, L. H. (1927). The calculation of atomic fields. *Mathematical Proceedings of the Cambridge Philosophical Society* *23*(5), 542–548.
- [41] VandeVondele, J., M. Krack, F. Mohamed, M. Parrinello, T. Chassaing, & J. Hutter (2005). Quickstep: Fast and accurate density functional calculations using a mixed gaussian and plane waves approach. *Computer Physics Communications* *167*(2), 103–128.
- [42] Zhang, Z., L. Stixrude, & J. Brodholt (2013). Elastic properties of MgSiO<sub>3</sub>-perovskite under lower mantle conditions and the composition of the deep Earth. *Earth and Planetary Science Letters* *379*, 1 – 12.

## Chapter 3

# Experimental Techniques

### 3.1 The synergy of experiment and simulation

The manuscripts presented in this thesis consist of a combination of theoretical calculations based on density functional theory and experiments using NMR spectroscopy, X-ray diffraction or a combination of both, or deal with the analysis of diffraction data. Therefore, a brief introduction to both techniques is given in the following, although I did not perform any experiments.

Nevertheless, it is especially important to highlight the possibilities emerging by a direct synergy between experiment and theory. Not only is it essential to compare published data, but also to directly link experimental and theoretical techniques in order to improve the reliability of theoretical predictions and give insight in the analysis of experimental data.

High- $P$  NMR spectroscopy, for example, has only recently become available [25] and there is still an ongoing learning process on what properties can be investigated, how they can be interpreted and what additional knowledge is necessary in order to analyse the rather abstract experimental data (Section 3.3). In this context, the manuscripts presented in Sections 4.2.1 and 4.2.2 deal with NMR and diffraction experiments on transition metal hydrides, which are interpreted on the basis of *ab-initio* calculations of electronic and ionic structure.

This chapter presents an introduction to experimental setups used by my collaborators in the scientific work discussed in this thesis. First, an introduction to the diamond anvil cell, the  $P$ -creating device used in all experiments, is given; subsequently NMR spectroscopy in general as well as the high-pressure setup are introduced, followed by X-ray diffraction in a static and dynamically driven DAC.

## 3.2 The Diamond Anvil Cell

The diamond anvil cell is an experimental high- $P$  device used to achieve static compressions of up to several hundred GPa. A DAC consists of a pair of diamonds within a metal housing, in between which a sub nano-litre sample can be highly compressed (Figure 3.1).

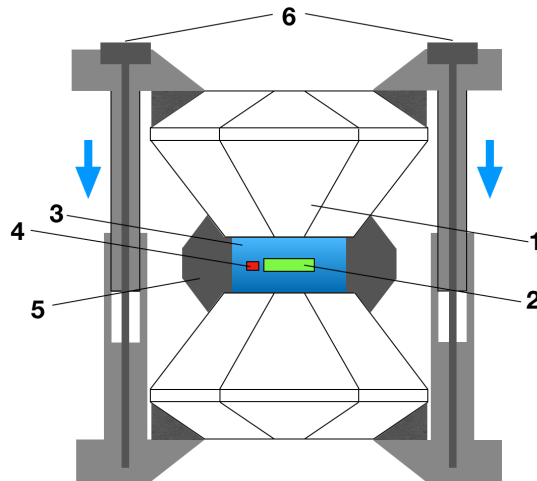


Figure 3.1: Schematics of a diamond anvil cell: (1) diamond anvils, (2) sample, (3) pressure medium (e.g. Ne), (4) pressure marker (e.g. Au, Pt), (5) gasket (typically Re) and (6) screws to create the loading force.

The sample (2) is contained in a gasket (5), usually Re or Be, surrounded by a pressure-transmitting medium (3) (e.g., Ne) in order to improve hydrostatic conditions. Additionally, a pressure marker (4), e.g., Au or Pt, with a well known equation-of-state (EOS) can be added (see Section 3.4). The gasket (5) is placed between the two diamond anvils (1) which sit in a metal housing consisting of two parts that can be slid into each other. To increase compression on the sample, screws (6) are tightened to apply force on the diamonds (1) via the metal housing.

There are different DAC designs, depending on the particular type of experiment, e.g., for X-ray diffraction [20] or for ultra high pressures by using secondary anvils [9]. Furthermore it is possible to heat the sample in the DAC either by placing a resistive heater close to the gasket or by laser [12], enabling high- $T$  experiments and sample synthesis within the DAC.

### Dynamic Diamond Anvil Cell (dDac)

Usually diamond anvil cells are hand-operated, but it is possible to compress the sample not through the torque of the screws via the metal housing, but by applying force to the

cell via a membrane [18] or piezoelectric activator [10, 19]. With these methods, very high compression rates in the order of TPa/s can be achieved. Furthermore it is possible to apply a periodic compression to the sample and thereby cycle through a phase transition or investigate the dynamic response of the sample at the frequencies of seismic waves [23].

### Possible Measurements

The diamond anvil cell as the  $P$ -creating apparatus enables a variety of experiments at high pressure: i) X-ray diffraction can be used to determine the atomic positions within a crystal lattice (Section 3.4). ii) Optical techniques, e.g., Raman [7], IR [30] and Brillouin [28] spectroscopy can be used to obtain information about the vibrational and elastic properties. iii) Mössbauer spectroscopy [26], the resonant absorption and emission of gamma rays by atomic nuclei in a solid, can be used to obtain information about, e.g. the oxidation state, electron shielding and magnetic hyperfine splitting. iv) NMR spectroscopy has only recently become available at high pressure ( $> 10$  GPa) and enables, among others, the investigation of electronic and diffusive properties.

### 3.3 Nuclear Magnetic Resonance Spectroscopy

Nuclear Magnetic Resonance spectroscopy as an experimental technique is widely applied in Chemistry, Medicine and Material Science. Its use as a spectroscopic technique was first demonstrated in 1945 by Felix Bloch [3], following the observation of nuclear magnetic resonance by Issac Rabi in 1939 [27, 2, 29]. The foundation of NMR is the Zeeman effect [31] (Nobel Prize 1902): the non-zero nuclear spin  $I$  of many stable elements leads, in the presence of a static magnetic field  $B_0$ , to a sub-level splitting  $\Delta E$  of the energy eigenvalues  $E_m$  and a resonance frequency defined by

$$E_m = -\gamma_n \hbar B_0 m, \quad m = I, I - 1, \dots, -I \quad (3.1a)$$

$$\Delta E = \gamma_n \hbar B_0 = \hbar \omega_0, \quad (3.1b)$$

where  $\gamma_n$  is the nuclear gyromagnetic ratio and  $\omega_0$  is the resonance frequency (equal to the Larmor precession frequency of a classical magnetic moment  $\mu = \gamma_n \hbar I$  in an external field  $B_0$ ).

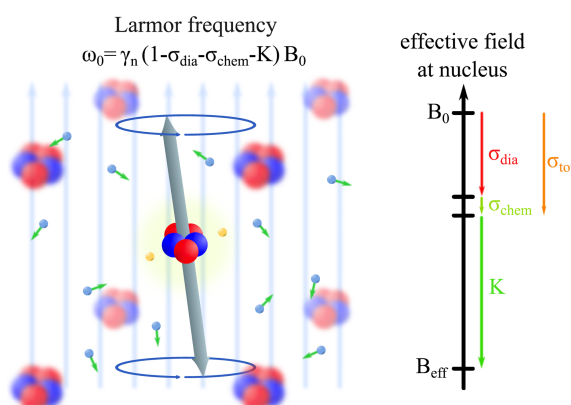


Figure 3.2: Visualization of the spin precession due to the effective magnetic field  $B_{\text{eff}}$ . The diamagnetic shielding induced by the presence of core electrons (yellow), the chemical environment and the Knight shift lead to a modified effective magnetic field  $B_{\text{eff}}$  indicated by the light blue field lines.

The external field  $B_0$  is shielded due to the magnetic properties of the surrounding, leading to an effective magnetic field and a modified  $\omega_0$

$$B_{\text{eff}} = (1 - \sigma_{\text{tot}})B_0 \Rightarrow \omega_0 = \gamma_n(1 - \sigma_{\text{tot}})B_0, \quad (3.2)$$

where  $\sigma_{\text{tot}}$  is the chemical shielding tensor containing contributions from diamagnetic

shielding of the surrounding electrons  $\sigma_{\text{dia}}$  and nuclei  $\sigma_{\text{chem}}$  (Figure 3.2).

Therefore, the resonance frequency  $\omega_0$  depends on the local chemical environment of the nucleus, and consequently this environment can be investigated by measuring the shift of the resonance frequency. In order to measure the resonance, an additional  $t$ -dependent magnetic field  $B_1(t)$  is introduced via a secondary coil. This field is chosen such that it leads, e.g., to a deflection of spin states by  $90^\circ$ . The energy released during the subsequent relaxation process is measured via the secondary coil as the induced voltage. The Fourier transformation of this signal contains information about the signal shift with respect to a reference frequency (usually tetramethylsilane for  $^1\text{H-NMR}$ ) and the relaxation time and thereby the chemical environment of the nucleus. Further details are described in, e.g., Bloembergen et al. [4] or Walstedt [29].

The influence of hyperfine interaction of conduction electrons on the nuclei must be taken into account as an additional shielding mechanism to explain the NMR signal of metallic systems. The effective external magnetic field becomes

$$B_{\text{eff}} = (1 - \sigma_{\text{tot}} - K_{\text{H}})B_0, \quad (3.3)$$

with the Knight shift [21]

$$K_{\text{H}} = \frac{1}{A\mu_{\text{B}}} \left[ H_{\text{HF}}^0 \chi_0 + \sum_i H_{\text{HF}}^i \chi_i \right], \quad (3.4)$$

where  $\chi_0$  summarizes the orbital paramagnetic and the diamagnetic contribution of the ion cores,  $H_{\text{HF}}$  is the respective hyperfine field, and  $\chi_i$  the magnetic susceptibility related to electronic state  $i$  (e.g.  $i = s, d$ ) [15].

For a Fermi gas we can substitute

$$\chi_i = 2\mu_0\mu_{\text{B}}^2 N_i(E_{\text{F}}), \quad (3.5)$$

where  $N_i(E_{\text{F}})$  is the electronic density of state at the Fermi energy for state  $i$  [15] leading to

$$K_{\text{H}} = \frac{1}{A} \left[ \frac{1}{\mu_{\text{B}}} H_{\text{HF}}^0 \chi_0 + 2\mu_0\mu_{\text{B}} \sum_i H_{\text{HF}}^i N_i \right]. \quad (3.6)$$

The modification of  $B_{\text{eff}}$  due to the Knight shift is typically one order of magnitude larger than the contribution of  $\sigma_{\text{tot}}$ .

### High-pressure NMR

Although NMR spectroscopy is widely used in Chemistry and Material Science, its application at high- $P$  has become possible due to the introduction of magnetic flux tailoring through Lenz lenses in the DAC [25]. In this special NMR setup, the high frequency coil close to the sample is supported by a Lenz lens, an inductively coupled broadband passive electromagnetic lens, to locally amplify the magnetic field at the isolated sample (Figure 3.3). This lens consists of a gold or copper layer, which is coated directly on the diamond and shaped using a focused ion beam (FIB). With the introduction of this lens, the filling factor (the fraction of the coil detection volume filled with sample) is significantly improved, which enables NMR spectroscopy at pressures up to 72 GPa [24] and with the introduction of second and third stage Lenz lenses up to 202 GPa (Section 4.2.1).

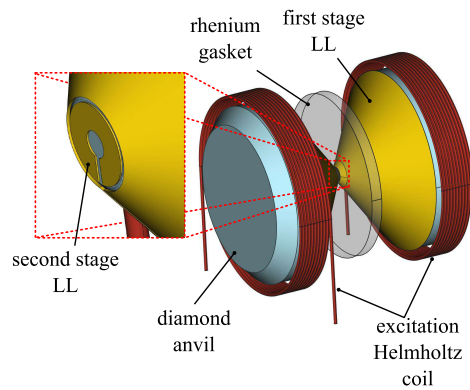


Figure 3.3: Schematics of the resonator setup with Lenz lenses (LL) and the anvil/gasket arrangement for NMR experiments in the diamond anvil cell [24]

### 3.4 X-Ray Diffraction

X-ray diffraction is one of the main experimental methods used in crystallography. Its importance is highlighted by Mike Glazer [14]:

„If it were not for crystallography, and especially the discovery of X-ray crystallography in 1912, the world today would look very different. There would not be much of a pharmaceuticals industry, nor useful drugs, no electronics to speak of, no computers, no worldwide communication, no mobile phones, and so on. “

The foundation of diffraction by X-rays (photons with  $E > 10$  eV or  $\lambda < 10$  nm) or, e.g., neutrons is Bragg’s Law [6]:

$$n\lambda = 2d_{\text{hkl}} \sin(\theta), \quad (3.7)$$

where  $d_{\text{hkl}}$  is the spacing between different lattice planes,  $\theta$  is the incident angle of the radiation,  $\lambda$  is the wavelength of the radiation and  $n \in \mathbb{N}$ . It states that light is only diffracted, if the value of  $\lambda$  satisfies equation (3.7) with respect to  $d_{\text{hkl}}$  and  $\theta$ , and that if  $\theta$  and  $\lambda$  are measured, it is possible to calculate  $d_{\text{hkl}}$  and therefore the positions of the scatterer, hence, in the case of a crystal, the space group. It is important to note that not the atomic cores, but the electrons contribute almost exclusively to the scattering of X-rays [17], and as a result, X-ray diffraction generates an electron-density map and therefore contains no direct information on the position of atomic cores. This means, that atoms with a larger number of electrons scatter stronger than those with less electrons, which leads to the problem that in the case of hydrogen with only one electron which is, in general, the donor in a bond, X-rays are not scattered from the position of the hydrogen core, but rather from the bond, and can therefore only give limited insight in the crystal structure.

In order to perform X-ray diffraction at elevated  $P$ , DACs are used in combination with an experimental setup depending on the sample. If the sample consists of a single crystal (sXRD), the cell (or detector) must be rotated or the beam must vary in frequency in order to probe a wide space in either  $\theta$  (angle dispersive) or  $\lambda$  (energy dispersive). The rotation leads to a three dimensional sphere of reflections, the Ewald sphere [11], from which the position of the scatterer can be reconstructed. For a powder sample (pXRD), consisting of small quasi-randomly oriented crystallites (depending on the growth mechanism),  $\theta$ -space is assumed to be sufficiently probed and so called Debye-Scherrer rings [8] emerge on the detector (Figure 3.6 a). These rings are integrated along the radius to obtain the intensity as a function of the angle relative to the incident beam. The main difference is that in

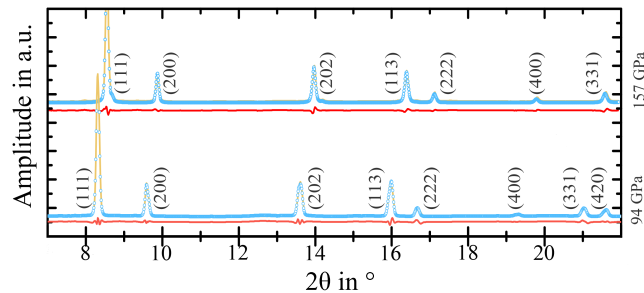


Figure 3.4: Powder X-ray diffraction patterns of  $\text{CuH}_x$  at 94 and 157 GPa. Blue dots are the experimental data, yellow line the fitted pattern and the red line represents the residual between the fit ( $\text{Fm}\bar{3}\text{m}$  with  $x = 1.0$ ) and the experimental data. Pressure is calculated from the Raman shift of the diamond.

pXRD the amplitudes of the scattered light cannot be used to calculate structure factors, like in sXRD, but combined with the simpler setup, it has the significant benefit that in many cases powders can be synthesised directly in the DAC at high- $P$  high- $T$  conditions. Figure 3.4 shows exemplary the pXRD pattern of a mixture of paraffin oil and copper powder after laser heating at a  $P$  of 94 and 157 GPa. The peaks are characteristic for  $\text{P}\bar{3}\text{m}1 \text{Cu}_2\text{H}$  (see Section 4.2.2 for details).

The main parts of the experimental setup are an X-ray source, a monochromator, a sample holder with or without a rotating platform in the case of sXRD and a detector with additional components to, e.g., heat the sample or shape the X-ray beam. Although, table top size X-ray diffractometers are common, due to the increasing effect of the DAC environment on scattering during compression, it is in general, but especially due to line broadening if the sample is heated, favourable to use a high-brilliance and higher intensity X-ray beam which can be found at synchrotron facilities. Details on the experimental setup can be found in Liermann et al. [22] where a detailed description of the Extreme Conditions Beamline P02.2 at DESY (Deutsches Electron-Synchrotron), where most of the X-ray experiments discussed in the following have been performed. To obtain information about the conditions in the DAC during a diffraction experiment a  $P$ -marker with known space group and EOS which does not react with the sample, e.g. gold, can be added. As the peak position reflects the distance between lattice planes, all peaks are shifted under compression to larger scattering angles. The compression-dependent peak position can be used to calculate the unit cell volume ( $V$ ) if the space group is known and through the EOS  $P$  is accessible. The downside of an additional  $P$ -marker is the potential to observe peak overlap with the actual sample and therefore, depending on the number of visible peaks, problems with the peak identification (Figure 3.7). Pressure can also be obtained

via optical techniques, e.g., Raman spectroscopy, but this requires an additional setup and complicates the logistics, especially at large synchrotron facilities.

Further details on the high- $P$  applications of X-ray diffraction beyond this short introduction are explained, for example, by Angel [1] and Boffa Ballaran et al. [5].

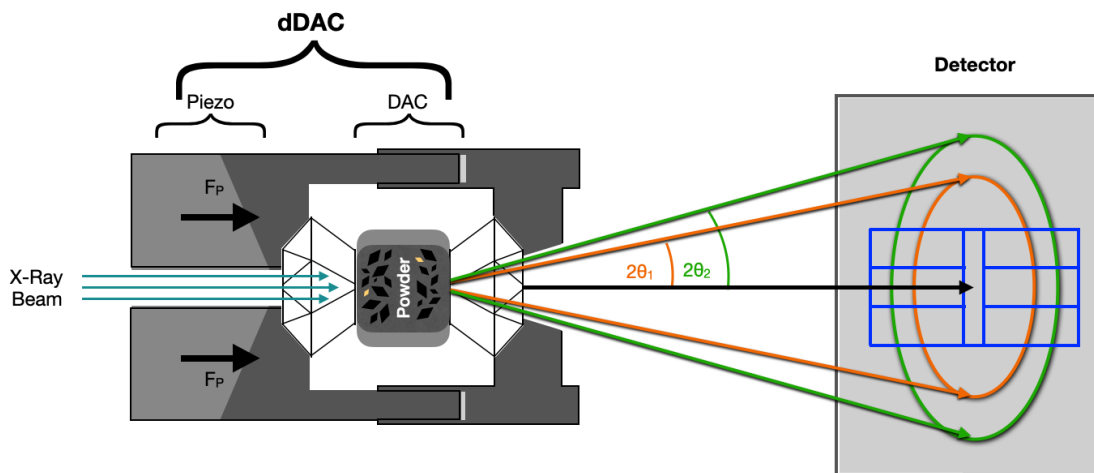


Figure 3.5: Schematic illustration of the dynamic Diamond Anvil Cell (dDAC) setup used. The DAC as described in Figure 3.1 is contained in a metal housing together with a piezo-actuator. If the a voltage is applied to the piezo-actuator, it extends and applies force to the housing of the DAC similar to the screws in Figure 3.1. The X-ray beam entering the cell is diffracted on the crystallites and pressure marker and creates Debye-Scherrer rings on the detector.

X-ray diffraction is, in general, performed under static compression in a DAC. But for some samples, especially hydrogen-bearing ones which can weaken the structural integrity of the diamonds, or if the dynamic response of a material is of interest, dynamic compression can be applied to a DAC via a piezoelectric element or a membrane (Section 3.2). In these experiments a large number of diffraction patterns is collected at a frequency of up to several MHz at compression rates of up to several hundred GPa per second. Hence, it is possible to collect extended  $P$ -series within minutes and construct an equation-of-state from the diffraction patterns (Section 4.1.2). The layout of such an experiment is illustrated in Figure 3.5.

Each diffraction pattern is integrated to obtain intensities as a function of the diffraction angle (Figure 3.4 and 3.6). In order to analyse the data, the peak positions must be assigned to a crystal structure and the position of the individual peaks must be tracked during the compression.

Figure 3.6 a) shows a powder pattern for a  $\text{H}_2\text{O}$  sample in a rhenium gasket with gold as a pressure marker with the characteristic Debye-Scherrer rings. Figure 3.6 shows the

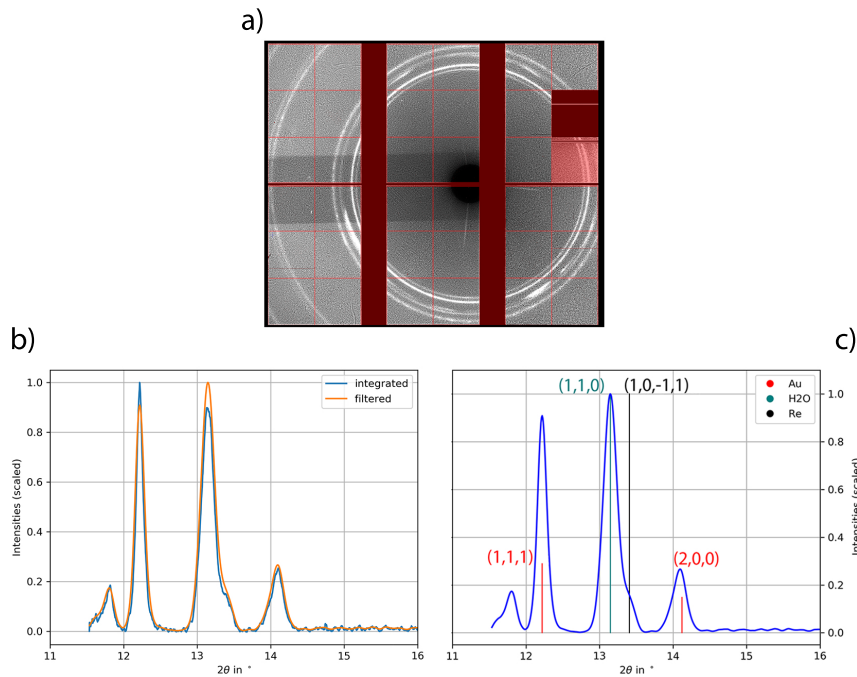


Figure 3.6: **(a)** Detector image of a water sample in a rhenium gasket with gold as a pressure marker at a pressure of 26 GPa, with a masked area in the upper right. **(b)** Integrated intensity as a function of the diffraction angle (blue) and with an infinite impulse response (IIR) filter [16] with zero phase shift (orange). **(c)** Diffraction pattern with assigned reflection indices. Solid vertical lines denote the position in  $2\theta$  space and the amplitude is relative to the largest peak. Both are calculated with the program introduced in Section 4.1.2. Pressure is determined from the signal of gold in combination with the equation-of-state by Fei et al. [13]. For the rhenium peak, the four indices version of the Miller indices ( $hkml$ ) for hexagonal systems with  $l = -(h + k)$  is used, assuming the same compression as for ice.

related intensity as a function of the diffraction angle after integration (b) and subsequent application of a low pass filter (c). The signal from the rhenium gasket is masked during the integration (light red area in Figure 3.6 a). Figure 3.7 shows diffraction patterns at  $P$  of 24 (a) and 45 GPa (b) which illustrates peak overlap between the rhenium gasket and the H<sub>2</sub>O sample upon compression. The peak from the gasket (1,0,-1,1) has a smaller shift under compression than the (1,1,0) peak of H<sub>2</sub>O. Consequently, the ordering in the pattern changes and the H<sub>2</sub>O peak „overtakes“ the rhenium peak at  $\sim 30$  GPa. These effects in combination with non-hydrostatic conditions due to the high compression rates as well as missing  $P$ -transmitting media and the amount of diffraction patterns ( $\gtrsim 1000$  per experiment) complicate the data analysis in dDAC experiments.

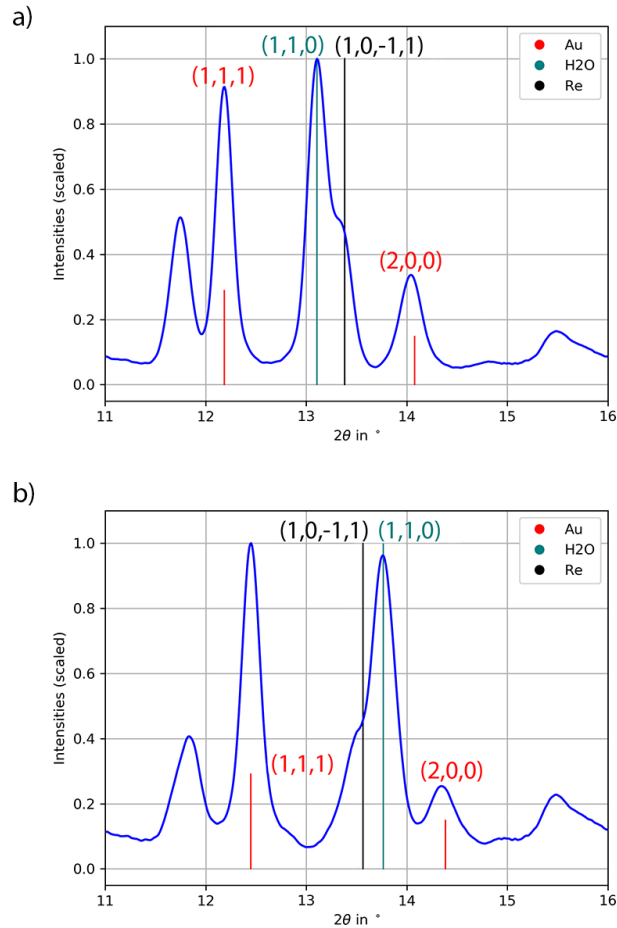


Figure 3.7: Powder diffraction pattern of water in a rhenium gasket with gold as a pressure marker at (a) 24 GPa and (b) 45 GPa. The example shows the overlap of H<sub>2</sub>O and rhenium peaks over a pressure range of 20 GPa where the ice peak is overtaking the rhenium peak in terms of  $2\theta$ -shift with compression. Pressure is determined from the signal of gold in combination with the equation-of-state by Fei et al. [13]. Blue lines are the experimental pattern after the IIR filter is applied to improve the signal/noise ratio. Solid vertical lines denote the calculated position in  $2\theta$ -space and the amplitude is relative to the largest peak.

## Bibliography

- [1] Angel, R. J. (2003). Automated profile analysis for single-crystal diffraction data. *Journal of Applied Crystallography* 36(2), 295–300.
- [2] Becker, E. D. (1993). A brief history of nuclear magnetic resonance. *Analytical Chemistry* 65(6), 295A–302A.
- [3] Bloch, F., W. W. Hansen, & M. Packard (1946). The Nuclear Induction Experiment. *Phys. Rev.* 70, 474–485.
- [4] Bloembergen, N., E. M. Purcell, & R. V. Pound (1948). Relaxation Effects in Nuclear Magnetic Resonance Absorption. *Phys. Rev.* 73, 679–712.
- [5] Boffa Ballaran, T., A. Kurnosov, & D. Trots (2013). Single-crystal X-ray diffraction at extreme conditions: a review. *High Pressure Research* 33(3), 453–465.
- [6] Bragg, W. H. & W. L. Bragg (1913). The reflection of X-rays by crystals. *Proceedings of the Royal Society of London. Series A, Containing Papers of a Mathematical and Physical Character* 88(605), 428–438.
- [7] Chariton, S., V. Cerantola, L. Ismailova, E. Bykova, M. Bykov, I. Kuppenko, C. McCammon, & L. Dubrovinsky (2018). The high-pressure behavior of spherocobaltite (CoCO<sub>3</sub>): a single crystal Raman spectroscopy and XRD study. *Physics and Chemistry of Minerals* 45(1), 59–68.
- [8] Debye, P. & P. Scherrer (1916). Interferenzen an regellos orientierten Teilchen im Röntgenlicht. I. *Nachrichten von der Gesellschaft der Wissenschaften zu Göttingen, Mathematisch-Physikalische Klasse* 1916, 1–15.
- [9] Dubrovinsky, L., N. Dubrovinskaia, V. B. Prakapenka, & A. M. Abakumov (2012). Implementation of micro-ball nanodiamond anvils for high-pressure studies above 6 Mbar. *Nat. Com.* 3(1), 1–7.
- [10] Evans, W. J., C.-S. Yoo, G. W. Lee, H. Cynn, M. J. Lipp, & K. Visbeck (2007). Dynamic diamond anvil cell (dDAC): A novel device for studying the dynamic-pressure properties of materials. *Review of Scientific Instruments* 78(7), 073904.
- [11] Ewald, P. P. (1913). Zur Theorie der Interferenzen der Röntgenstrahlen in Kristallen. *Phys. Z* 14, 465–472.
- [12] Fedotenko, T., L. Dubrovinsky, G. Aprilis, E. Koemets, A. Snigirev, I. Snigireva, A. Baranikov, P. Ershov, F. Cova, M. Hanfland, et al. (2019). Laser heating setup for diamond anvil cells for in situ synchrotron and in house high and ultra-high pressure studies. *Review of Scientific Instruments* 90(10), 104501.
- [13] Fei, Y., A. Ricolleau, M. Frank, K. Mibe, G. Shen, & V. Prakapenka (2007). Toward an internally consistent pressure scale. *Proceedings of the National Academy of Sciences* 104(22), 9182–9186.
- [14] Glazer, A. M. (2016). *Crystallography: A very short introduction*, Volume 469. Oxford University Press.
- [15] Goring, R., R. Lukas, & K. Bohmhammel (1981). Multipulse NMR investigation of band structure in titanium hydride: proton Knight shift and spin-lattice relaxation. *Journal of Physics C: Solid State Physics* 14(36), 5675–5687.
- [16] Gustafsson, F. (1996). Determining the initial states in forward-backward filtering. *IEEE Transactions on signal processing* 44(4), 988–992.
- [17] Hammond, C. (2015). *The Basics of Crystallography and Diffraction*. IUCr monographs on crystallography. Oxford University Press.
- [18] Jenei, Z., H. Cynn, K. Visbeck, & W. J. Evans (2013). High-temperature experiments using a resistively heated high-pressure membrane diamond anvil cell. *Review of Scientific Instruments* 84(9), 095114.

- [19] Jenei, Z., H. P. Liermann, R. Husband, A. S. J. Méndez, D. Pennicard, H. Marquardt, E. F. O'Bannon, A. Pakhomova, Z. Konopkova, K. Glazyrin, M. Wendt, S. Wenz, E. E. McBride, W. Morgenroth, B. Winkler, A. Rothkirch, M. Hanfland, & W. J. Evans (2019). New dynamic diamond anvil cells for tera-pascal per second fast compression x-ray diffraction experiments. *Review of Scientific Instruments* 90(6), 065114.
- [20] Kantor, I., V. Prakapenka, A. Kantor, P. Dera, A. Kurnosov, S. Sinogeikin, N. Dubrovinskaia, & L. Dubrovinsky (2012). BX90: A new diamond anvil cell design for X-ray diffraction and optical measurements. *Review of Scientific Instruments* 83(12), 125102.
- [21] Knight, W. D. (1949). Nuclear magnetic resonance shift in metals. *Phys. Rev.* 76, 1259–1260.
- [22] Liermann, H.-P., Z. Konôpková, W. Morgenroth, K. Glazyrin, J. Bednarčík, E. E. McBride, S. Petitgirard, J. T. Delitz, M. Wendt, Y. Bican, A. Ehnes, I. Schwark, A. Rothkirch, M. Tischer, J. Heuer, H. Schulte-Schrepping, T. Kracht, & H. Franz (2015). The Extreme Conditions Beamline P02.2 and the Extreme Conditions Science Infrastructure at PETRA III. *Journal of Synchrotron Radiation* 22(4), 908–924.
- [23] Marquardt, H., J. Buchen, A. Méndez, A. Kurnosov, M. Wendt, A. Rothkirch, D. Pennicard, & H.-P. Liermann (2018). Elastic softening of  $(\text{Mg}_{0.8}\text{Fe}_{0.2})\text{O}$  ferropericlase across the iron spin crossover measured at seismic frequencies. *Geophysical Research Letters* 45(14), 6862–6868.
- [24] Meier, T., S. Petitgirard, S. Khandarkhaeva, & L. Dubrovinsky (2018). Observation of nuclear quantum effects and hydrogen bond symmetrisation in high pressure ice. *Nature Communications* 9(1), 2766.
- [25] Meier, T., N. Wang, D. Mager, J. G. Korvink, S. Petitgirard, & L. Dubrovinsky (2017). Magnetic flux tailoring through lenz lenses for ultrasmall samples: A new pathway to high-pressure nuclear magnetic resonance. *Science Advances* 3(12), eaao5242.
- [26] Narygina, O., L. S. Dubrovinsky, C. A. McCammon, A. Kurnosov, I. Y. Kantor, V. B. Prakapenka, & N. A. Dubrovinskaia (2011). X-ray diffraction and Mössbauer spectroscopy study of fcc iron hydride FeH at high pressures and implications for the composition of the Earth's core. *Earth and Planetary Science Letters* 307(3–4), 409–414.
- [27] Rabi, I. I., S. Millman, P. Kusch, & J. R. Zacharias (1939). The Molecular Beam Resonance Method for Measuring Nuclear Magnetic Moments. The Magnetic Moments of  ${}^3\text{Li}^6$ ,  ${}^3\text{Li}^7$  and  ${}^9\text{F}^{19}$ . *Phys. Rev.* 55, 526–535.
- [28] Satta, N., H. Marquardt, A. Kurnosov, J. Buchen, T. Kawazoe, C. McCammon, & T. B. Ballaran (2019). Single-crystal elasticity of iron-bearing phase E and seismic detection of water in Earth's upper mantle. *American Mineralogist* 104(10), 1526–1529.
- [29] Walstedt, R. E. (2018). *The NMR Probe of High- $T_c$  Materials and Correlated Electron Systems*. Springer.
- [30] Yang, X., H. Keppler, L. Dubrovinsky, & A. Kurnosov (2014). In-situ infrared spectra of hydroxyl in wadsleyite and ringwoodite at high pressure and high temperature. *American Mineralogist* 99(4), 724–729.
- [31] Zeeman, P. (1897). On the influence of magnetism on the nature of the light emitted by a substance. *The London, Edinburgh, and Dublin Philosophical Magazine and Journal of Science* 43(262), 226–239.

## Chapter 4

# Synopsis



## 4.1 High-Pressure H<sub>2</sub>O Ice

The following two subsections compile the work performed on H<sub>2</sub>O ices, in particular, the ice-VII to ice-X transition. The first section summarizes the density-functional-theory-based work in comparison with recently published NMR results [39]. The second section presents a study on the compressional behavior of H<sub>2</sub>O ice up to 180 GPa at room  $T$  using time-resolved XRD in a piezo-driven dynamic DAC.

### 4.1.1 Proton Dynamics in High-Pressure Ice-VII

The following subsection summarizes the manuscript included in section 5.1:

*„Proton Dynamics in High-Pressure Ice-VII from Density Functional Theory“*

Florian Trybel, Michael Cosacchi, Thomas Meier, Vollrath Martin Axt  
and Gerd Steinle-Neumann

Status: Submitted to *Physical Review Letters*  
(30 June 2020)

#### Individual Contributions

On the basis of NMR experiments [39], Thomas Meier, Gerd Steinle-Neumann and I designed the study. I performed and analysed the density functional theory calculations and wrote the scripts to perform the hydrogen bond sampling. Together with Michael Cosacchi, I designed and wrote the Python program to calculate the tunnelling frequencies and the related analysis software. Together with Michael Cosacchi, Gerd Steinle-Neumann and Vollrath Martin Axt, I wrote the manuscript.

We directly sample the potential seen by the proton along the diagonal oxygen-oxygen direction (dOOd) in the *bcc* oxygen host-lattice as a function of the lattice constant  $l$  between 3.35 and 2.55 Å. In order to perform the sampling, we move all protons in the 128 molecules ice-rule conforming [4] supercell in 22 steps along their respective dOOd. The resulting energies per proton are interpolated with a third order spline and the energetic minima is calculated for each  $l$ . We obtain a double-well potential (characterized by an energy barrier  $\Phi_m$  and the distance between each minimum and the center of the dOOd,  $\delta_c$ ) at low compression (Figure 4.1), and observe a continuous transition to a single-well

with decreasing  $l$ . Equilibrium positions obtained through the collective displacement of all protons are used to optimise the background, when only a fraction of the protons is sampled in additional configurations.

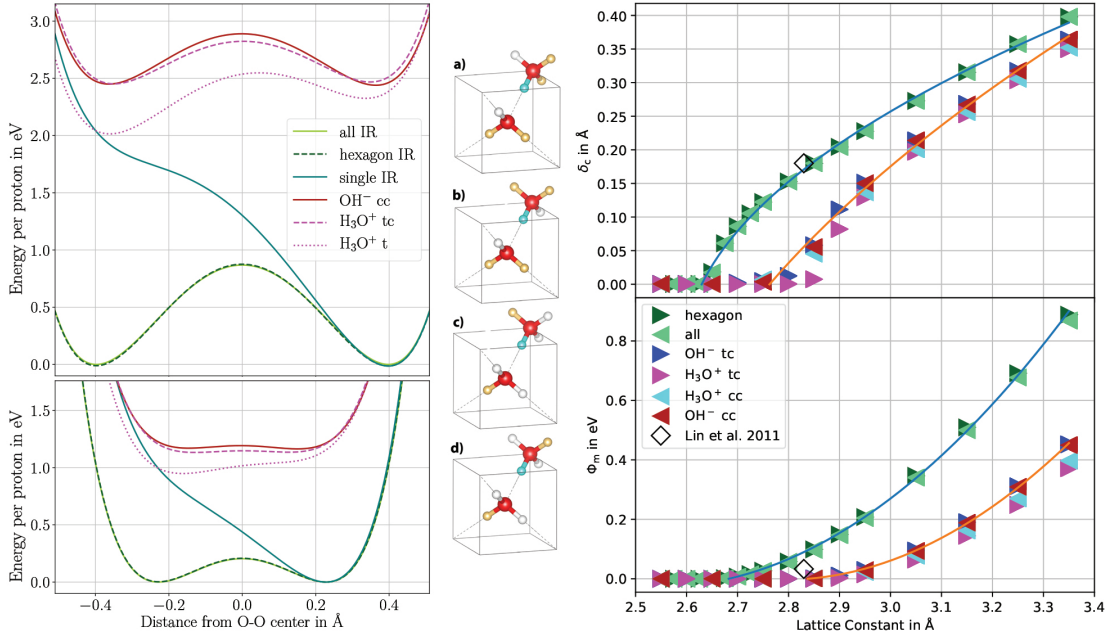


Figure 4.1: **(left)** Energy of different proton configurations for  $l = 3.35 \text{ \AA}$  (top) and  $l = 2.95 \text{ \AA}$  (bottom) and visualization of possible configurations with a single-proton ice-rule violation. Oxygen in red, unoccupied hydrogen positions in white, occupied hydrogen positions in yellow and sampled hydrogen in teal. **a)**  $\text{H}_3\text{O}^+$  in cis configuration, **b)**  $\text{H}_3\text{O}^+$  in trans configuration, **c)**  $\text{OH}^-$  in cis configuration and **d)**  $\text{OH}^-$  in trans configuration. Potentials displayed are for a collective motion of protons (all), the collective hexagonal configuration (hexagon) and a single proton (single), all obeying the ice-rules. Potentials for the ice-rule breaking arrangements are  $\text{H}_3\text{O}^+$  in the trans (t) configuration, without and with conjugation (tc) of the associated charge defect, and  $\text{OH}^-$  in the conjugated cis (cc) configuration.  $\text{H}_3\text{O}^+ \text{ tc}$  and  $\text{OH}^- \text{ cc}$  are shown as they bracket the potential of all ice-rule breaking structures. **(right)** Parameter describing the structure of the double-well potential as a function of lattice parameter  $l$ : (top)  $\delta_c$ , the distance between the center of the double-well and the minima; (bottom)  $\Phi_m$ , the height of the barrier. Solid lines are fits of a square root for  $\delta_c$  and a quadratic function for  $\Phi_m$  to the hexagonal (green) and the  $\text{OH}^-$  trans points (orange). Black diamonds show result of path integral *ab-initio* molecular dynamics simulations at  $l = 2.84 \text{ \AA}$  [35].

If only one proton is sampled in the ice-rule conforming configuration [4], we obtain a strongly asymmetric single-well with the minimum coinciding with one of the minima of the all-proton sampling. With increasing compression the potential becomes more symmetric and converges into the all-proton case, when the double-well character is lost (Figure 4.1).

In previous path integral based studies [35] ([12] for hexagonal ice), a collective motion of six protons in a hexagonal configuration was identified without breaking the ice-rules. We follow this suggestion and move six protons in such a configuration. The resulting potentials are in nearly perfect agreement with the all-proton case with a slight asymmetry due to the position of the hexagon in the simulation cell combined with the periodic boundary conditions (Figure 4.1).

It is furthermore possible to create configurations where a single proton exhibits a double-well potential by breaking the ice-rules at a position next to the sampling point. This way, one of the four configurations illustrated in Figure 4.1 a) - d) with two possible hydrogen arrangements at the two enclosing oxygen atoms ( $\text{OH}^-$  or  $\text{H}_3\text{O}^+$ ) and two possible symmetries with respect to the dOOd (cis or trans) can be realised. To reduce the asymmetry of the potential, we conjugate the emerging defect in local charge neutrality to the edge of the simulation cell (Figure 4.1).

The double-well parameters  $\delta_c$  and  $\Phi_m$  (Figure 4.1) fall in two groups: (i) ice-rule conforming structures where the double-well character is lost at  $l \lesssim 2.675 \text{ \AA}$ ; and (ii) for ice-rule breaking structures at  $l \lesssim 2.85 \text{ \AA}$ . Comparing the parameters with the results of path integral based calculations of Lin et al. [35] shows a very good agreement of  $\delta_c$  for the all/hexagonal configuration. The barrier height,  $\Phi_m$ , has a lower value than our prediction. We attribute this difference to the fact that Lin et al. [35] performed an ensemble calculation compared to our single configuration sampling as well as the classical treatment of the protons compared to their quantum mechanical approach. Temperature is neglected in our calculations to this point, but the good agreement between our prediction for  $\delta_c$  and the path integral results taking thermal effects into account, suggests that  $T$  does not have a strong influence on the width of the potential.

The double-well parameters itself are only of limited value for a comparison with experimental data, but the dynamics of the system provides greater insight. We calculate the proton dynamics by numerically solving the 1-D time-dependent Schrödinger equation for the proton in the effective potential using a matrix exponential formalism. The initial state is described by a generic 1D-Gaussian of the form

$$\Psi(x) = \frac{1}{\mathcal{I}} \mathcal{F}\left(\frac{x-x_0}{3a}\right) \frac{1}{\sqrt{a\sqrt{\pi}}} \exp\left(-0.5\left(\frac{x-x_0}{a}\right)^2\right), \quad (4.1)$$

where  $k_B$  is the Boltzmann and  $\hbar$  the reduced Planck constant,  $x$  the position along dOOd,  $a$  and  $x_0$  the width and center of the Gaussian,  $m$  the proton mass.  $\mathcal{F}$  is a mollifier [17], improving the localization of  $\Psi$ , leading to a significant speed-up and a higher stability of the numerics, without affecting any physical features.  $\mathcal{I}$  ensures normalization of  $\Psi(x)$ .

We assume that through a spontaneous symmetry breaking the protons are localised at one of the minima positions at  $t = t_0$  and therefore choose  $x_0$  for the initial state such, that  $\Psi(x)$  is centered at the minimum of the respective potential for each  $l$ .

In order motivate this choice, it is helpful to first look at an eigenvalue analysis of the Hamiltonian

$$\mathcal{H} = -\frac{\hbar^2}{2m_p}\mathcal{D} + \Phi, \quad (4.2)$$

where  $\mathcal{D}$  is the matrix representation of the 3rd order central difference scheme with a stencil reduction at the boundaries, and  $\Phi$  the diagonal matrix constructed from the obtained potential at each  $l$ . If we construct an initial state as the superposition of the two lowest eigenstates, it is straightforward to show that the resulting wave packet oscillates between the minima with a frequency  $\nu_{01}^H$ , exactly corresponding to the difference in energies of both eigenstates, representing the tunnelling frequency. As the eigenstates of the Hamiltonian are a basis set, any initial state can be decomposed into them, and the resulting dynamics includes all frequencies which correspond to the combinatorically possible differences between their energies. While exactly diagonalizing the Hamiltonian yields all  $\nu^H$  taking part in the dynamics, solving the problem with a physically motivated initial state additionally provides access to amplitudes. If we diagonalize  $\mathcal{H}$ , we find  $\nu_{01}^H$  to increase with  $P$  in a square root-like fashion between 5 and  $\sim 100 - 120$  GPa and linearly upon further compression to our maximum pressure of 200 GPa.

To obtain a dynamical property related to tunnelling from time evolution of  $\Psi$  in the potential, we calculate the probability of finding the wave packet in the left hand side of the potential at each time step as

$$p(x < 0) = \int_{-\infty}^0 |\Psi(x)|^2 dx. \quad (4.3)$$

The Fourier transform of  $p(x < 0)$ ,  $p(k)$ , results in a  $\nu^{FT}$ -spectrum that perfectly coincides with the set of  $\nu^H$  calculated from the diagonalization of the Hamiltonian.

Choosing  $x_0$  for the initial state as the minimum of the respective potential leads to a non-zero overlap between the ground state and the first excited state and therefore  $\nu_{01}^{FT} > 0$  as long as  $x_0$  is not central. Once the minimum of the potential moves to the center ( $x_0 = 0$ ), no overlap between the ground state (symmetric) and the first excited state (antisymmetric) is expected, and the amplitude of  $\nu_{01}^{FT}$  should vanish, indicating the completion of symmetrization. We find  $\nu_{01}^{FT}$  to follow the  $P$ -dependence of  $\nu_{01}^H$  to  $P \lesssim 130$  GPa, where a significant drop in amplitude occurs, suggesting that the  $\nu_{01}$  oscillation no longer contributes to the dynamics of the system and no tunnelling is expected to happen.

If we compare the amplitude of  $\nu_{01}^{FT}$  in  $p(k)$  as a function of  $P$  with results by Meier et al. [39] (Figure 4.2), we find that the hexagonal configuration reproduces the  $P$ -dependence of the NMR line-shape analysis at room  $T$  well: A strong increase in amplitude up to  $P \sim 20$  GPa, a plateau to  $P \sim 80-90$  GPa, and a subsequent drop in mobile protons. This further supports the interpretation of Lin et al. [35] that charge balance is widely maintained at low  $T$  and consequently tunnelling in correlated hexagonal rings is dominant.

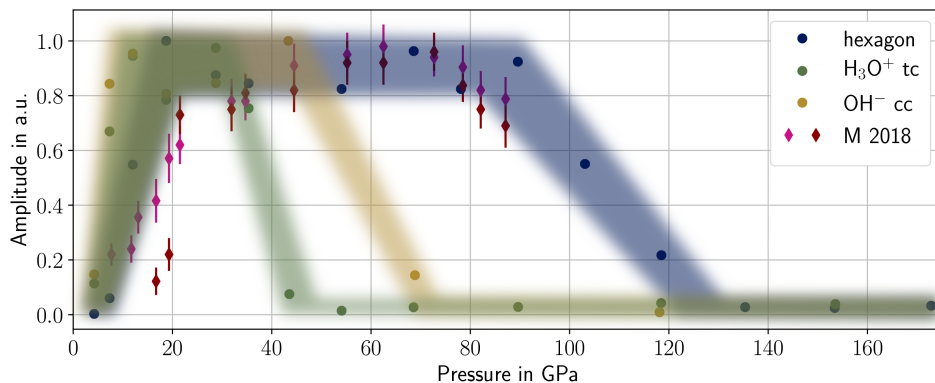


Figure 4.2: Amplitude of  $\nu_{01}^{FT}$  in  $p(k)$  as a function of  $P$  at 300 K for the different configurations considered in this study. Amplitudes are normalized to the maximum value for the respective configuration. Diamonds in magenta and purple show the result of a peak analysis of NMR experiments by Meier et al. [39] (M 2018).

We do not find a sharp phase transition in cubic ice between the emergence of ice-VII at  $\sim 2$  GPa and 200 GPa, well in the stability range of ice-X, but a gradual change from a double- to a single-well potential, and we predict related changes in proton dynamics. Based on our results we can distinguish regions of characteristic proton dynamics and potential (at room  $T$ ):

- (i) For  $2 \text{ GPa} < P < 20 \text{ GPa}$ , protons become increasingly delocalized, as the potential barrier decreases;
- (ii) for  $20 \text{ GPa} < P < 90 \text{ GPa}$ , protons tunnel in a fashion well represented by correlated hexagons;
- (iii) for  $90 \text{ GPa} < P < 130 \text{ GPa}$ , symmetrization occurs and the amplitude of  $\nu_{01}^{FT}$  drops significantly as the potential barrier becomes small, but non-zero;
- (iv) for  $P \gtrsim 130 \text{ GPa}$ , the system is fully symmetric and no proton dynamics is expected.

In  $P$ -ranges (i) and (iii), varying energy and momentum transfer to the sample by different experimental methods may modify the probed potential, ranging from an excitation of the

proton spin system without significant momentum or energy transfer to the lattice in NMR [39], through momentum transfer by collisions with neutrons [30], the excitation of lattice vibrations in Raman [25, 48, 58], IR [22] and Brillouin [3, 2, 59] spectroscopy, to high-energy irradiation with X-rays [56, 37, 50, 51]. Based on this observation we suggest that experimental methods can be expected not to agree on a single transition  $P$  in a system like H<sub>2</sub>O ice. Further, the limited experimental resolution in terms of  $P$ -sampling may lead to an over-interpretation of the nature of the phase transition, in some cases suggesting a sharp transition [22, 51, 52].

### 4.1.2 Ice-VII – ice-X transition studied by time-resolved XRD in a dDAC

The following subsection summarizes the manuscript included in section 5.2:

*„Bulk modulus of H<sub>2</sub>O across the ice-VII – ice-X transition measured by time-resolved X-ray diffraction in dynamic Diamond Anvil Cell experiments “*

Alba S.J. Méndez, Florian Trybel, Rachel Husband, Gerd Steinle-Neumann,  
Hanns-Peter Liermann and Hauke Marquardt

Status: Submitted to *Physical Review B*

(25 June 2020)

#### Individual Contributions

I wrote the diffraction pattern analysis and peak-fitting software. Alba S.J. Méndez, Rachel Husband, Hanns-Peter Liermann and Hauke Marquardt designed and performed the experiment. Together with Alba S.J. Méndez, Hauke Marquardt and Gerd Steinle-Neumann, I analysed the data and wrote the manuscript.

We perform dynamic compression experiments with time-resolved X-ray diffraction in order to understand the compression behavior of H<sub>2</sub>O across the ice-VII – ice-X transition by using a dynamic Diamond Anvil Cell driven by a piezoelectric actuator up to 180 GPa [14, 26]. As discussed in Section 4.1.1, the properties, especially the bulk modulus, of ice-VII are still not fully understood at high  $P$ . It is furthermore not clear, if the transitions in the potential character and proton mobility significantly influence the bulk modulus and, in particular, if they can be related to distinct features in XRD.

Three symmetric DACs are prepared with 150, 100 and 80  $\mu\text{m}$  diameter culet anvils (dDAC-1, dDAC-2 and dDAC-3). Two different gasket configurations are employed: (i) In dDAC-1, a disk of an amorphous boron alloy (Fe<sub>0.79</sub>Si<sub>0.06</sub>B<sub>0.15</sub>) and (ii) in dDAC-2 and dDAC-3, regular Re gaskets. Milli-Q H<sub>2</sub>O is loaded along with Au powder (99.99% pure from Sigma Aldrich) as a pressure marker and a ruby chip to control  $P$  in the sample during pre-compression. The DAC is coupled to a high voltage piezoelectric actuator and trapezoidal voltage-time waveforms are applied with average compression rates ranging from 0.3-0.6 GPa/s permitting the employment of long exposure times while still achieving

a high pressure-resolution. Monochromatic synchrotron radiation with a fixed wavelength (0.4828 Å) is used for time-resolved XRD measurements at the Extreme Conditions Beamline P02.2 at PETRA III [34]. For dDAC-2, one detector was aligned with the sample center, allowing the collection of full diffraction rings. For dDAC-1 and dDAC-3, the two detectors L1 and L2 were placed on either side of the sample center capturing different sections of the Debye–Scherrer diffraction rings [8], where images were collected simultaneously. We consider dDAC-2 as the reference experiment. Using dDAC-1, we can investigate the influence of the different gasket material and dDAC-3 the influence of a different compression rate on the results. The obtained detector images are integrated

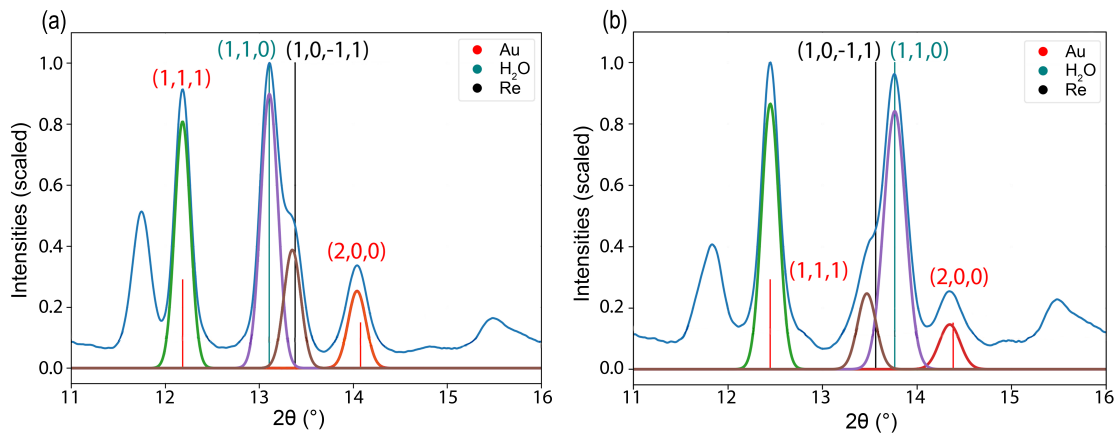


Figure 4.3: Extended Version of Figure 3.7 including the set of Gaussians fitting the pattern and a linear background correction (solid lines). **a)** and **b)** are diffraction patterns for dDAC-2 at 24 GPa and 45 GPa, respectively. The examples show the interaction of the ice and rhenium peak over a pressure range of 20 GPa where the ice peak is overtaking the rhenium peak in terms of  $2\theta$  shift with compression. Pressure is determined from the signal of gold in combination with the equation-of-state by Fei et al. [15]. Blue lines are the experimental pattern after an infinite impulse response filter [24] is applied to improve the signal/noise ratio. Solid vertical lines denote the calculated peak position in  $2\theta$  space and the respective amplitude relative to the highest peak. For the rhenium peak, the four indices version of the Miller indices ( $hklm$ ) for hexagonal systems with  $l = -(h + k)$  and the same compression as for ice is assumed.

using the Dioptas software [46] to obtain diffraction patterns as a function of the  $2\theta$ -angle and indices assigned through peak comparison. A python routine is written to deal with the large number of diffraction patterns and to automate peak fitting and tracking. Before integrated patterns are processed by the routine, we average over three points in  $2\theta$ -space and apply an infinite impulse response filter with zero phase shift [24] to improve the signal to noise ratio and the reliability as well as the speed of the fitting routine (Figure 3.6). The routine calculates a theoretical diffraction pattern for the sample,  $P$ -marker

and gasket material as a function of a given compression ( $V/V_0$ ) using a routine from the pymatgen (Python Materials Genomics) library [44] and optimizes a model consisting of a Gaussian for each peak and a linear background correction using the *LMFIT* package [43] on the basis of a non-linear least-squares formalism. The compression is optimized with an adaptive step width such that the theoretical peak positions and the fitted model coincide within  $\epsilon \lesssim 10^{-3}$  in  $2\theta$ -space (Figure 4.3). A possible peak from the gasket is calculated to improve the initial guess in the fitting routine, but neglected in the optimization. From the optimized theoretical peak positions, the volume of the sample and the  $P$ -marker are calculated and using the EOS by Fei et al. [15].

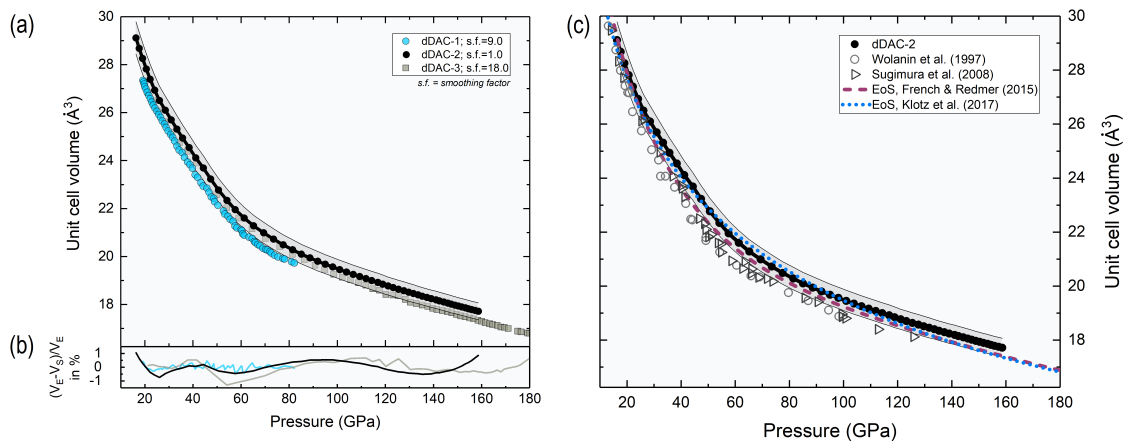


Figure 4.4: **(a)** Volume-pressure points of H<sub>2</sub>O ice as derived from dDAC-1 (blue solid circles), dDAC-2 (black solid circles) and dDAC-3 (grey solid squares) experiments. Data are splined with smoothing factors of 9.0 (dDAC-1), 1.0 (dDAC-2) and 18.0 (dDAC-3), with the interpolation shown for dDAC-2 (black curve). **(b)** Difference between the data points and the smoothed spline is under 1% over the complete compression range for all experiments. **(c)** Previous XRD measurements in static Diamond Anvil Cell experiments by Wolanin et al. [56] (grey open circles) and Sugimura et al. [51] (black open triangles) are plotted in comparison with  $P$ - $V$  derived from dDAC-2. The maroon dashed lines represents the computational equations-of-state by French & Redmer [16] and the blue dotted line the EOS by Klotz et al. [30], fitted to neutron diffraction data and extrapolated beyond the maximum pressure of 14 GPa reached in the experiments.

The fitting is significantly complicated by the large amount of patterns, asymmetry in the peaks (possibly due to non-hydrostatic conditions because of a missing  $P$ -transmitting medium) and peak overlap. An interaction between  $(110)_{\text{IceVII}}$  and  $(10-11)_{\text{Re}}$  is shown in Figure 4.3. At low pressure, the  $(110)_{\text{IceVII}}$  appears at a lower  $2\theta$ -value than the  $(10-11)_{\text{Re}}$ . During compression, peaks start to overlap at  $P > 20$  GPa and the reorder with respect to the  $2\theta$ -angle at  $P > 40$  GPa.

Differences between the unit cell volumes calculated from the three experimental runs fall within the experimental uncertainty (Figure 4.4 a), suggesting that the compression rate and gasket material have no significant influence on the data. The results are in general agreement with previous XRD [51, 56] and neutron diffraction [30] measurements as well as the calculated equation-of-state of French & Redmer [16], but show a distinct change in slope at  $P \approx 35 - 45$  GPa (Figure 4.4 c).

Due to the high data density, we can calculate the isothermal bulk modulus as

$$K_T = -V \left( \frac{\partial P}{\partial V} \right)_T \quad (4.4)$$

without any assumption on the analytic form of the EOS. Nevertheless, the data density complicates the calculation of the derivative, as small jumps in the  $P$ - $V$  curve appear strongly magnified in the derivative. Therefore, we use only every 5th data point for dDAC-2/3 and every 25th for dDAC-1, in order to reduce noise and calculation time, while still preserving a sufficient resolution. Furthermore, we apply a smoothing [10] to the  $P$ - $V$  data, such that smooth variations of the bulk modulus with  $P$  were obtained, while simultaneously keeping the difference between the data points and the smoothed spline below 1% over the complete compression range for all experiments (Figure 4.4 b). The error is calculated from the minimal possible peak separation ( $0.05^\circ$  in  $2\theta$ ) and propagated with a finite difference scheme to  $K_T$ . The pressure is assumed to be error free, as there is no asymmetry or peak overlap for the  $P$ -marker and therefore the peak positions can be optimised to an  $\epsilon$  at least one order of magnitude smaller compared to the sample peak. The resulting bulk modulus as a function of pressure is shown in Figure 4.5. We find three distinct changes in the slope of  $K_T$ :

- (i) A softening between 35 and 45 GPa indicates the transition towards a more compressible state. We associate this change with an increase in tunnelling probability and the accompanying formation of dynamically disordered ice-VII'.
- (ii) A step increase in bulk modulus for  $P \approx 50 - 55$  GPa marks a more incompressible phase. We attribute this feature to the formation of ice-X'.
- (iii) A distinct change in  $P$ -dependence of the bulk modulus between 90 and 110 GPa, which has not been documented by previous experiments on the elastic properties of ice-VII. We attribute this change to the formation of static ice-X in agreement with Section 4.1.1.

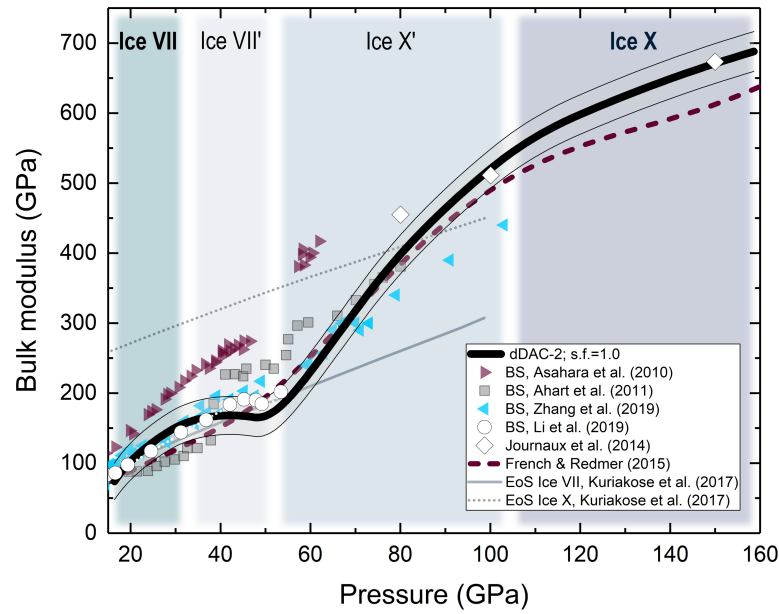


Figure 4.5: Bulk modulus of H<sub>2</sub>O ice as a function of pressure calculated from the smoothed spline interpolation of the fitted  $P$ - $V$  data for dDAC-2 in comparison to previous studies. Right-pointing triangles, solid squares, left-pointing triangles and solid circles represent Brillouin inelastic scattering (BS) data [3, 2, 59, 33]. The solid and dotted thin lines represent the equations of state for ice-VII and ice-X, respectively [32]. Open diamonds represent theoretical predictions of the bulk modulus of ice-X [27]. The dashed line refers to computational results [16]. The shaded areas represent the approximate pressure stability regimes of ice-VII, ice-VII', ice-X' and ice-X based on changes in bulk modulus.

### 4.1.3 Summary & Outlook

We show that the character of proton dynamics can be investigated by sampling the effective potential seen by the individual protons through a set of DFT calculations and obtain potentials in agreement with path integral based calculations [35] and proton dynamics showing a  $P$ -dependence in agreement with NMR based experiments [39].

Time-resolved synchrotron XRD measurements have been performed using a dDAC driven by a piezoelectric actuator. We record diffraction data for H<sub>2</sub>O ice up to 180 GPa with a dense enough  $P$ -resolution to numerically calculate the bulk modulus without the necessity of assuming an analytical EOS and respective phase transitions. Furthermore, we were able to show that the changes in proton dynamics affect the bulk modulus, resolvable in XRD.

Both studies provide a consistent picture and suggest that there are no sharp transitions, certainly not of first, unlikely of second order, contradictory to previous claims [22, 51, 52]. More interestingly, the steep increase in the amplitude of  $\nu_{01}^{FT/H}$  at  $P \gtrsim 20$  GPa seems to control the softening in the bulk modulus prominently visible at 35-40 GPa in the XRD measurements. The increase in bulk modulus, starting from 50-55 GPa, is in agreement with reaching a saturation in the amplitude of  $\nu_{01}^{FT/H}$ . The following decrease in amplitude between 90 and 120 GPa correlates with a gradual change in the slope of the bulk modulus.

The sampling method used to investigate the character of the potential is not limited to H<sub>2</sub>O, but can be used to analyse other structures expected to undergo a hydrogen bond symmetrization. Furthermore, it is possible to perform a multi-step structure optimization, where self-consistently the hydrogen position and the atomic positions in a host lattice can be optimized. This enables the treatment of more complex compounds, e.g.  $\delta(\text{Al,Fe})\text{OOH}$  [49], where not only the hydrogen position is expected to symmetrize, but the host lattice undergoes a structural reconfiguration synchronously.

## 4.2 Transition Metal Hydrides

The following two subsections compile the work performed on the metal hydride systems Fe-H and Cu-H. The first subsection summarizes NMR experiments and electronic structure calculations for the Fe-H system. The second subsection discusses the work performed on the Cu-H system, where also XRD experiments are performed.

### 4.2.1 Pressure-Induced Hydrogen-Hydrogen Interaction in FeH

The following subsection summarizes the published paper included in Section 5.3:

*„Pressure-Induced Hydrogen-Hydrogen Interaction  
in Metallic FeH revealed by NMR“*

Thomas Meier, Florian Trybel, Saiana Khandarkhaeva, Gerd Steinle-Neumann, Stella Chariton, Timofey Fedotenko, Sylvain Petitgirard, Michael Hanfland, Konstantin Glazyrin, Natalia Dubrovinskaia, and Leonid Dubrovinsky

Status: Published

Phys. Rev. X 9, 031008 – 17 July 2019

#### Individual Contributions

I performed and analysed the *ab-initio* calculations of structural and electronic properties supported by Gerd Steinle-Neumann. Together with Thomas Meier, Gerd Steinle-Neumann, Leonid Dubrovinsky and Natalia Dubrovinskaia, I performed the overall data analysis and wrote the manuscript. Thomas Meier and Leonid Dubrovinsky designed the experiment. Thomas Meier, Saiana Khandarkhaeva and Sylvain Petitgirard prepared the DACs and NMR resonators. Saiana Khandarkhaeva performed focused ion beam cutting as well as structure refinement after laser heating. Leonid Dubrovinsky performed the sample synthesis in the DACs. Stella Chariton and Timofey Fedotenko performed XRD measurements at DESY and ESRF, respectively.

This work combines NMR spectroscopy and density functional theory based calculations to investigate the electronic properties and characteristics of hydrogen-hydrogen interaction in FeH at pressures of up to 200 GPa. Iron monohydride was synthesized in the diamond anvil cell from iron powder and paraffin oil at 30 GPa upon laser heating to

1200 K. Synchrotron X-ray diffraction shows peaks of *fcc* FeH<sub>x</sub> [41, 53], with no residual signal from pure iron. The hydrogenation degree *x* is estimated from the volume expansion with respect to *fcc* iron to be *x*= 1.0(1) as suggested by [41], and additional XRD measurement at 150 GPa suggest that the structure is stable over the complete pressure-range of interest.

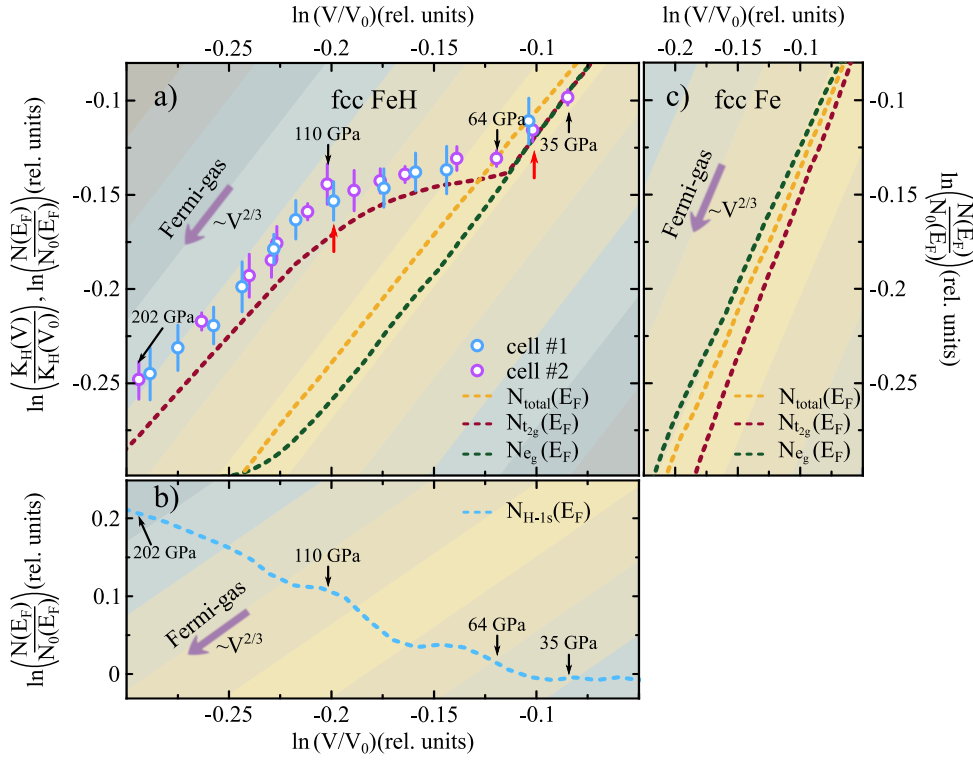


Figure 4.6: Comparison of experimental data and *ab-initio* electronic density of states calculations. (a) Double logarithmic power plot of relative changes in Knight shift  $K_H$  and  $N(E_F)$  as a function of the relative volume. Experimental data points (blue and purple) are normalized to  $V_0$  using the equation-of-state from [41] and extrapolated values of  $K_H(V_0)$ . The dashed lines (splines through computed values) show the dependence of  $N_{total}(E_F)$ ,  $N_{t_{2g}}(E_F)$ , and  $N_{e_g}(E_F)$ . The diagonal color stripes are guides to the eye depicting a  $\propto V^{2/3}$  scaling for free-electron Fermi-gas-like behavior,  $N(E_F) \propto V \cdot \sqrt{V^{-2/3}}$ . Black arrows denote respective pressure points; red arrows show data recorded under decompression. (b) Evolution of  $N_{H-1s}$  - indicated pressure markers are related to the experimental data from (a). (c) Volume dependence of  $N_{total}(E_F)$ ,  $N_{t_{2g}}(E_F)$ , and  $N_{e_g}(E_F)$  for *fcc* Fe over a similar compression range.

NMR measurements show a strong signal from the hydrogen reservoir (paraffin oil) before laser heating, with a frequency similar to earlier studies [42, 53]. After laser heating, a second peak with a shifted frequency can be assigned to iron hydride, with the value of the Korringa ratio [31] falling in between pure  $^{57}\text{Fe}$  and hydrogen. As introduced in equation

(3.6) (Section 3.3), the Knight shift

$$K_H = \frac{1}{A\mu_B} \left[ H_{\text{HF}}^0 \chi_0 + 2\mu_0 \mu_B^2 \sum_i H_{\text{HF}}^i N_i \right] \quad (4.5)$$

can be used as a measure for the metallic character of a sample. In a metallic sample with  $N(E) \propto V\sqrt{E}$ ,  $E_F \propto V^{-2/3}$  and  $N(E_F) \propto V \cdot \sqrt{V^{-2/3}}$ , the Knight shift should follow a  $V^{-2/3}$  slope under compression.

For *fcc* FeH, NMR measurements show a deviation from the ideal metallic behavior of the Knight shift between 64 and 110 GPa (Figure 4.6). In order to investigate this deviation and its underlying mechanism, we performed density functional theory based calculations for *fcc* iron-monohydride. Our calculations predict, in agreement with Mössbauer spectroscopy measurements by Narygina et al. [41] that ferromagnetism is not found at pressures over 30 GPa. The calculated orbital projected electronic density-of-state shows the same characteristic deviation as the Knight shift from the NMR measurements for  $N_{t_{2g}}(E_F)$  of the iron *3d* state (Figure 4.6 a) accompanied by an increase in  $N_{\text{H}_{1s}}(E_F)$  of hydrogen. *fcc*-iron at the same  $V$  does not show this feature (Figure 4.6 b) and we conclude therefore that the deviation is related to interaction with or between the hydrogen atoms. Features of this type in the electronic DOS may be related to a topological transition visible in the electronic band structure [21]. As no feature is visible in the band structure, we use the electronic localization function (ELF) to investigate two-dimensional electronic localization. Under increasing compression, the ELF indicates the formation of areas of Fermi-gas-like electron localization connecting the hydrogen atoms as an intercalating sublattice, similar to the delocalized electronic background found in metals.

The network starts to form and spread at  $V/V_0 \lesssim 0.88$ , corresponding to  $P \gtrsim 60$  GPa, at the same point where the Knight shift and the calculated electronic DOS start to deviate from  $V^{-2/3}$  proportionality. It is fully connected at  $P \gtrsim 100$  GPa ( $V/V_0 \lesssim 0.78$ ), where Knight shift and electronic DOS return to a  $V^{-2/3}$  slope. Figure 4.7 shows projections of the ELF on three different planes for a  $V/V_0$  value of 0.9 and 0.69, corresponding to a pressure of 30 and 200 GPa, where the sublattice is not yet and fully formed, respectively.

This study shows that pressure-induced H-H interactions can occur in metal hydrides at much lower compression and larger H-H distances ( $\sim 2.4 \text{ \AA}$ ) than previously thought. This suggests an alternative pathway in the search for novel high- $T_c$  superconductors.

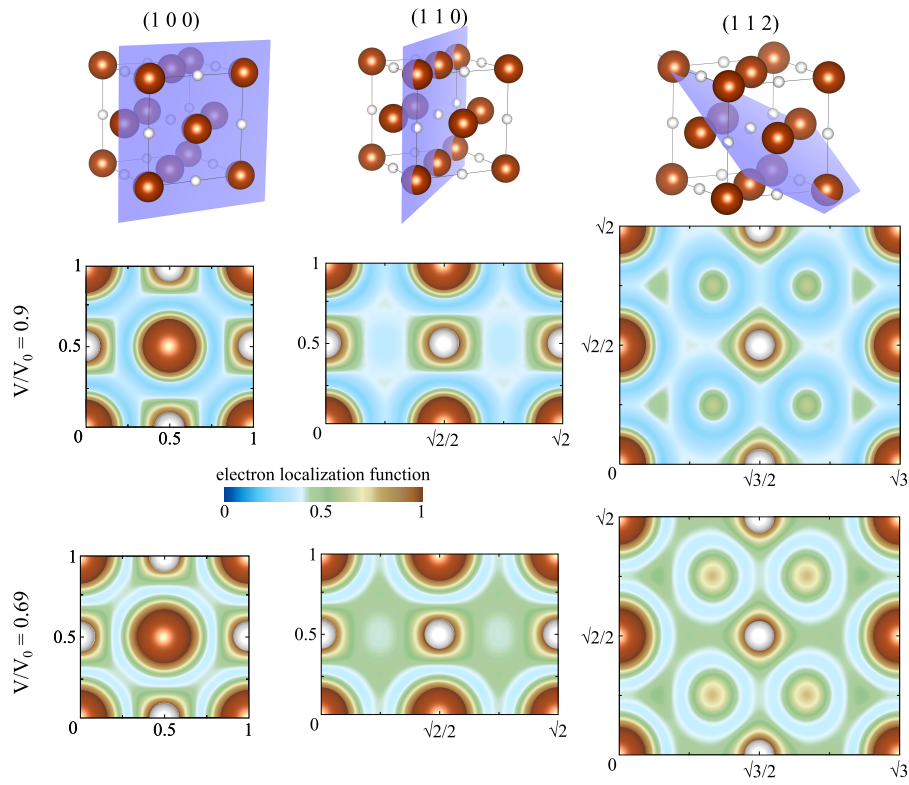


Figure 4.7: Electron localization function maps in three major crystal planes at a compression of  $V/V_0 = 0.9$  and  $0.69$ , corresponding to 30 and 200 GPa, respectively. Brown spheres represent iron atoms, white spheres hydrogen. Green areas (ELF  $\sim 0.5$ ) correspond to Fermi-gas-like regions of free electrons.

### 4.2.2 Proton Mobility in Metallic Copper Hydride

The following subsection summarizes the manuscript included in Section 5.4:

*„Proton Mobility in Metallic Copper Hydride from High Pressure  
Nuclear Magnetic Resonance “*

Thomas Meier\*, Florian Trybel\*, Giacomo Criniti, Dominique Laniel, Saiana  
Khandarkhaeva, Egor Koemets, Timofey Fedotenko, Konstantin Glazyrin, Michael  
Hanfland, Maxim Bykov, Gerd Steinle-Neumann, Natalia Dubrovinskaia  
and Leonid Dubrovinsky

Status: Submitted to *Physical Review B*  
(Submitted 21 July 2020, Revised 21 August 2020)

#### Individual Contributions

I performed and analysed the *ab-initio* calculations of structural, electronic and dynamical properties supported by Gerd Steinle-Neumann. Together with Thomas Meier, Leonid Dubrovinsky, Natalia Dubrovinskaia and Gerd Steinle-Neumann, I performed the overall data analysis and wrote the manuscript. Thomas Meier and Leonid Dubrovinsky designed the experiments. Thomas Meier, Leonid Dubrovinsky, Saiana Khandarkhaeva, and Dominique Laniel prepared all diamond anvil cells. Giacomo Criniti, Dominique Laniel, Egor Koemets, Timofey Fedotenko, Konstantin Glazyrin, Michael Hanfland, Maxim Bykov and Leonid Dubrovinsky performed the diffraction experiments.

\*Thomas Meier and I contributed equally to this study.

In this study, we combine XRD and high- $P$  NMR spectroscopy with *ab-initio* calculations to investigate the atomic and electronic structures of  $\text{Cu}_2\text{H}$  and  $\text{CuH}$  and therefore extend our study on iron mono-hydride (Section 4.2.1) to a more complex system,  $\text{Cu-H}$ , where different crystal structures coexist over the  $P$ -range of interest.

All  $\text{CuH}_x$  compounds are synthesized by direct reaction of pure copper and paraffin in the laser-heated DAC [41]. After laser heating at 35 GPa, a trigonal compound forms. We determine the crystal structure by powder as well as single crystal diffraction as  $\text{Cu}_2\text{H}$  (space group  $P\bar{3}m1$ ) and calculated an EOS from a third order Birch-Murnaghan fit to our DFT calculations with optimised  $c/a$  ratios. The  $V$ - $P$  points obtained for the  $\text{Cu}_2\text{H}$  compound are found to be in very good agreement with our calculated EOS and the EOS

of Donnerer et al. [11] (Figure 4.8). Laser heating of  $\text{Cu}_2\text{H}$  or pristine copper with paraffin at  $P > 50$  GPa results, in agreement with previous observations [5], in the formation of a cubic phase with an *fcc* arrangement of Cu atoms at up to  $P \simeq 160$  GPa. The volume expansion relative to *fcc* copper is in agreement with *fcc*-structured  $\text{CuH}_{0.65}$  [5] (Figure 4.8). After repeated heating and *T*-quench of the cubic phase at  $P \lesssim 110$  GPa, our data suggest a copper hydride with a larger hydrogen content than previously reported at high  $P$  [11, 5]. The respective XRD data compare very well with our *ab-initio* calculations on the EOS of NaCl-structured  $\text{CuH}$  and we therefore, infer that the cubic copper hydride has a ratio of  $\text{Cu}/\text{H}=1$  ( $\text{CuH}$ ).

NMR measurements of the copper-paraffin sample at 5 GPa (before heating) show signals originating solely from the paraffin reservoir. Additional signals appear after laser heating at 50 and 89 GPa, assigned to  $\text{Cu}_2\text{H}$  and  $\text{CuH}$ , respectively. During decompression of  $\text{Cu}_2\text{H}$  to  $P \lesssim 16$  GPa, the spectrum is interpreted as that of  $\text{CuH}_{0.15}$  [54]. Based on the excellent agreement between the  $V$ - $P$  points determined from XRD and the *ab-initio* equation-of-states for  $\text{Cu}_2\text{H}$  and  $\text{CuH}$ , we confidently compare the high- $P$  NMR data to the results of our electronic structure calculations.

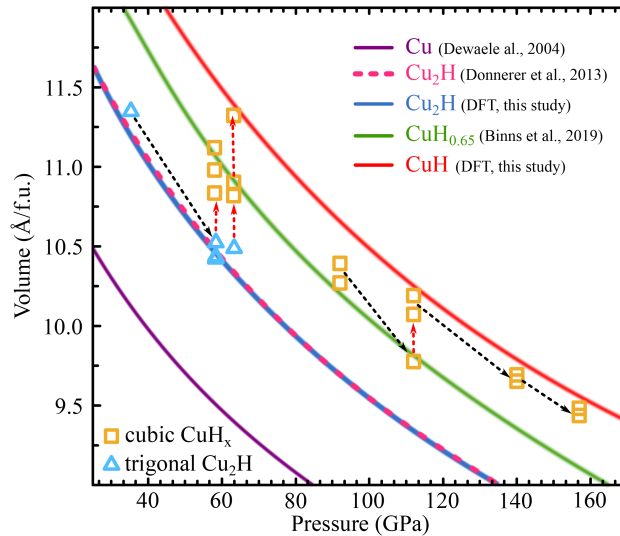


Figure 4.8: Equations of state of the copper hydride phases and pure Cu: the experimental equations-of-state for pure copper (Dewaele et al. [9] and  $\text{CuH}_{0.65}$  (Binns et al. [5]) are shown in purple and green, respectively. The brown dashed line denotes the experimental equation-of-state for  $\text{Cu}_2\text{H}$  (Donnerer et al. [11]). The results of a third order Birch-Murnaghan fit to the *ab-initio* energies are shown by a blue curve for  $\text{Cu}_2\text{H}$  and red for  $\text{CuH}$ . Open orange squares and blue triangles denote structures refined from diffraction data, and the arrows illustrate the experimental pathways of heating (red) and compression (black).

We find that  $K_{\text{H}}$  for both  $\text{CuH}_{0.15}$  and  $\text{CuH}$  violate Fermi gas ideality in agreement with Xiao et al. [57], while  $K_{\text{H}}$  of  $\text{Cu}_2\text{H}$  follows a slope expected for a free electron gas-like system ( $K_{\text{H}} \propto V^{2/3}$ ), but displays a deviation from free electron gas behavior between 43 and 58 GPa (Figure 4.9 a), similar to  $\text{FeH}$  between 64 and 110 GPa (Section 4.2.1). This effect can also be seen in the dependence of the calculated  $N(E_{\text{F}})$ , which follows  $K_{\text{H}}$  perfectly for both  $\text{Cu}_2\text{H}$  and  $\text{CuH}$ . The contribution of the orbital-resolved DOS of the hydrogen  $1s$  electron to  $N(E_{\text{F}})$  for  $\text{Cu}_2\text{H}$  and  $\text{FeH}$  gradually increases with decreasing distance between hydrogen atoms  $r_{\text{HH}}$ , suggesting that conduction electron density from the uncompensated  $4s$  states in  $\text{Cu}_2\text{H}$  or respectively the uncompensated  $3d\text{-}t_{2g}$  states in  $\text{FeH}$  is transferred to  $N_{\text{H-}1s}(E_{\text{F}})$  (Figure 4.9 b). By contrast,  $N_{\text{H-}1s}(E_{\text{F}})$  of semi-metallic  $\text{CuH}$  shows a strongly negative slope. Given the similarity of the observed behavior in  $K_{\text{H}}$  and electronic DOS for  $\text{Cu}_2\text{H}$  with that of  $\text{FeH}$ , we explain the deviation by the onset of significant H-H and H-Cu interactions in trigonal  $\text{Cu}_2\text{H}$  at  $P \sim 40$  GPa.

The dependence of the relative proton NMR resonance line-widths on  $r_{\text{HH}}$  (taken from *ab-initio* simulations at corresponding  $P$ ) increases under compression for  $r_{\text{HH}} > 2.45$  Å ( $P = 43$  GPa for  $\text{Cu}_2\text{H}$  and  $P = 64$  GPa for  $\text{FeH}$ ) as expected due to dipolar coupling ( $\sim r_{\text{HH}}^{-3}$ ) [1]; under further compression ( $r_{\text{HH}} < 2.45$  Å), line-widths decrease significantly. Since diffraction data and computational results on  $\text{Cu}_2\text{H}$  and  $\text{FeH}$  do not show signs of structural transitions within the experimental  $P$ -range, electronic and dynamic effects on the hydrogen spin system must be considered. Hydrogen spin-lattice relaxation rates  $R_1$  in metal hydrides originate from two mechanisms: (i) electronic hyperfine interactions and (ii) proton diffusion [29]. Assuming  $R_1 = 1/T_1$  [1, 6], where  $T_1$  is the relaxation time, the electronic hyperfine interaction  $R_1^e$  calculated from the respective Knight shift [23] is

$$R_1^e = \frac{4\pi k_{\text{B}} T}{\hbar} \left( \frac{\gamma_{\text{n}}}{\gamma_{\text{e}}} \right)^2 K_{\text{H}}^2, \quad (4.6)$$

where  $k_{\text{B}}$  is the Boltzmann,  $\hbar$  the reduced Planck's constant and  $\gamma_{\text{e}}$ ,  $\gamma_{\text{n}}$  the gyromagnetic ratios of the electron and the hydrogen nucleus, respectively. Furthermore, following Bloembergen et al. [6] the effect of diffusion is described by

$$R_1^d = \frac{3\pi \gamma^4 \hbar^2 N_0}{10 a D}, \quad (4.7)$$

where  $N_0$  is the number density of atoms,  $a$  the distance of closest approach which is at the order of  $r_{\text{HH}}$ ,  $\hbar$  Planck's constant and  $D$  the hydrogen diffusion coefficient. Calculating  $R_1^e$  from  $K_{\text{H}}$ , in the extreme narrowing limit [47], we can calculate  $R_1^d = R_1 - R_1^e$  and

furthermore the the hydrogen diffusion coefficient as

$$D = \frac{3\pi}{10} \frac{\gamma^4 h^2 N_0}{a} \left( T_1^d \right)_n. \quad (4.8)$$

The hydrogen diffusion coefficient can be calculated from molecular dynamics via the species resolved mean-square-displacement (calculated with a modified version of QUANTUM ESPRESSO [20, 19]) using equation (2.10). Comparing the coefficients for  $\text{Cu}_2\text{H}$  and  $\text{FeH}$  (Figure 4.9 c), we can see that the line-width analysis and the calculated diffusion coefficients are in qualitative agreement and show significant proton mobility in the range of  $10^{-7} \text{ cm}^2/\text{s}$ . Proton mobility investigated in other metal hydride systems by NMR find diffusion coefficients to typically lie between  $10^{-13}$  and  $10^{-7} \text{ cm}^2/\text{s}$  [29, 7, 38, 55].  $\text{Cu}_2\text{H}$  and  $\text{FeH}$  fall in the upper limit of this broad range, suggesting that proton self-diffusion plays a significant role in high- $P$  metal hydrides compared to hydrides stabilized at ambient conditions.

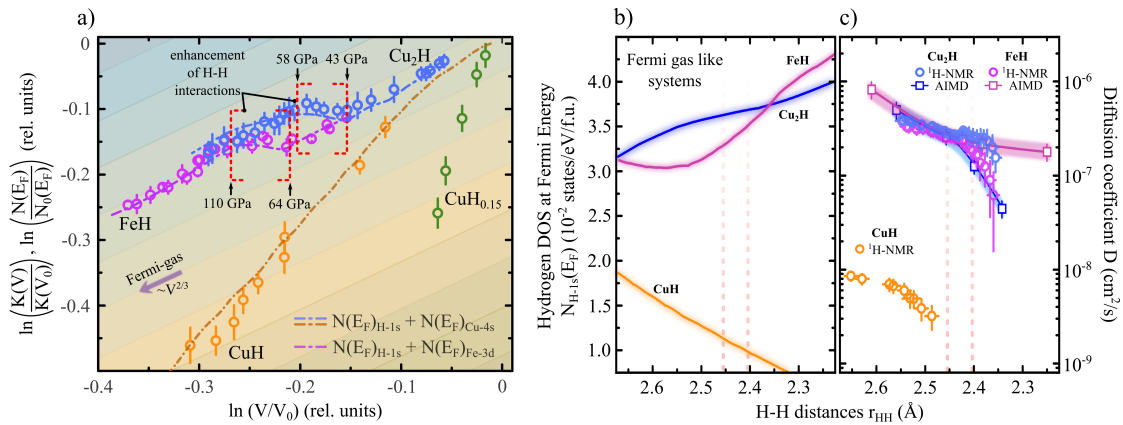


Figure 4.9: Comparison of experimental NMR data and electronic structure calculations. **a)** Double logarithmic power plot of relative changes in the NMR Knight shift  $K_{\text{H}}(V)$  and the electron-density-of-states at the Fermi energy  $N(E_{\text{F}})$  as a function of relative volume. Experimental data points (blue, magenta, orange and green) have been normalized to  $K_{\text{H}}(V_0)$  and  $V_0$  using the respective equation-of-states from Tkacz et al. [54] ( $\text{CuH}_{0.15}$ ) and DFT computations from this study ( $\text{CuH}$  and  $\text{Cu}_2\text{H}$ ); The blue, magenta and orange dashed lines (splines through computed values) show the respective volume dependence of  $N(E_{\text{F}})$ . Diagonal color stripes are guides to the eye representing a  $\propto V^{2/3}$  scaling for free-electron Fermi-gas-like behavior. **b)** and **c)** Comparison of electronic structure and proton diffusivities. **b)** Hydrogen  $1s$  electron density of state contribution  $N_{\text{H-1s}}(E_{\text{F}})$  of  $\text{CuH}$ ,  $\text{Cu}_2\text{H}$  and  $\text{FeH}$  as a function of the H-H distance in the structures (pressure increasing to the right). **c)** Proton diffusion coefficients calculated from NMR data (blue, purple and orange circles) and computed via *ab-initio* molecular dynamics simulations (blue and magenta squares and lines) for metallic  $\text{Cu}_2\text{H}$  and  $\text{FeH}$ , and the semi-metallic  $\text{CuH}$ . Vertical pink lines denote the formation range of enhanced H-H interactions.

Cu<sub>2</sub>H reveals a surprising onset of hydrogen-hydrogen interactions in a  $P$ -range of 43-58 GPa, associated with an enhanced electronic density of states at the Fermi level of the hydrogen 1s state. Our previous work on FeH (Section 4.2.1) shows very similar effects in the electronic structure in a  $P$ -range of 64-110 GPa. Correlating these effects with the average hydrogen-hydrogen distance, we find that in both compounds H-H interactions influence the electronic structure at the same  $r_{\text{HH}}$ , and therefore may only weakly depend on the parent transition metal ions. This insight may provide an important step in the future search and design of novel hydride-based high- $T$  superconductors.

### 4.2.3 Summary & Outlook

We have used a combination of XRD, high- $P$  NMR and *ab-initio* electronic structure calculations to investigate the hydrogen sub-system in transition metal hydrides with Fe-H and Cu-H compositions. We find an increase in hydrogen-hydrogen interaction at an unexpectedly low average hydrogen-hydrogen distance of 2.4 Å, coinciding for both phases and therefore suggest that the interaction may be independent of the host lattice. Furthermore, we find a high proton self-diffusion coefficient from both a NMR line width analysis and *ab-initio* molecular dynamics simulations in metallic FeH and Cu<sub>2</sub>H, with a possible impact on vibrational and therefore superconducting properties.

The combination of high- $P$  NMR and *ab-initio* electronic structure calculations provides a perfect toolkit to investigate the properties of metal hydrides. We have furthermore illustrated that our approach can be used to underpin structure refinement by XRD, although currently only for relatively simple systems. As we learn more about the possibilities high- $P$  NMR provides if it is directly supported by *ab-initio* calculations, we can proceed to systems with a more complex phase diagram, e.g. Y-H and La-H [13, 36]. Combining high- $P$  NMR with structure prediction on phases where XRD cannot refine the structure sufficiently, e.g., super-hydrides with a high hydrogen content and complex structures [45, 18, 28], the electronic properties can be used to compare predicted structures with the results of NMR experiments as suggested by Monserrat et al. [40].

## Bibliography

- [1] Abragam, A. & L. C. Hebel (1961). *Principles of Nuclear Magnetism, 18th ed.* Oxford University Press.
- [2] Ahart, M., M. Somayazulu, S. A. Gramsch, R. Boehler, H.-k. Mao, & R. J. Hemley (2011). Brillouin scattering of H<sub>2</sub>O ice to megabar pressures. *The Journal of Chemical Physics* 134(12), 124517.
- [3] Asahara, Y., K. Hirose, Y. Ohishi, N. Hirao, & M. Murakami (2010). Thermoelastic properties of ice VII and its high-pressure polymorphs: Implications for dynamics of cold slab subduction in the lower mantle. *Earth and Planetary Science Letters* 299(3), 474 – 482.
- [4] Bernal, J. D. & R. H. Fowler (1933). A Theory of Water and Ionic Solution, with Particular Reference to Hydrogen and Hydroxyl Ions. *The Journal of Chemical Physics* 1(8), 515–548.
- [5] Binns, J., M. Peña-Alvarez, M.-E. Donnelly, E. Gregoryanz, R. T. Howie, & P. Dalladay-Simpson (2019). Structural Studies on the Cu–H System under Compression. *Engineering* 5(3), 505–509.
- [6] Bloembergen, N., E. M. Purcell, & R. V. Pound (1948). Relaxation Effects in Nuclear Magnetic Resonance Absorption. *Phys. Rev.* 73, 679–712.
- [7] Bowman Jr, R. C., D. M. Gruen, & M. H. Mendelsohn (1979). NMR studies of hydrogen diffusion in  $\beta$ -LaNi<sub>5-y</sub>Al<sub>y</sub> hydrides. *Solid State Communications* 32(7), 501–506.
- [8] Debye, P. & P. Scherrer (1916). Interferenzen an regellos orientierten Teilchen im Röntgenlicht. I. *Nachrichten von der Gesellschaft der Wissenschaften zu Göttingen, Mathematisch-Physikalische Klasse* 1916, 1–15.
- [9] Dewaele, A., P. Loubeyre, & M. Mezouar (2004). Equations of state of six metals above 94 GPa. *Physical Review B* 70(9), 094112.
- [10] Dierckx, P. (1975). An algorithm for smoothing, differentiation and integration of experimental data using spline functions. *Journal of Computational and Applied Mathematics* 1(3), 165–184.
- [11] Donnerer, C., T. Scheler, & E. Gregoryanz (2013). High-pressure synthesis of noble metal hydrides. *The Journal of Chemical Physics* 138(13), 134507.
- [12] Drechsel-Grau, C. & D. Marx (2017). Collective proton transfer in ordinary ice: local environments, temperature dependence and deuteration effects. *Physical Chemistry Chemical Physics* 19, 2623–2635.
- [13] Drozdov, A. P., P. P. Kong, V. S. Minkov, S. P. Besedin, M. A. Kuzovnikov, S. Mozaffari, L. Balicas, F. F. Balakirev, D. E. Graf, V. B. Prakapenka, E. Greenberg, D. A. Knyazev, M. Tkacz, & M. I. Eremets (2019). Superconductivity at 250 K in lanthanum hydride under high pressures. *Nature* 569(7757), 528–531.
- [14] Evans, W. J., C.-S. Yoo, G. W. Lee, H. Cynn, M. J. Lipp, & K. Visbeck (2007). Dynamic diamond anvil cell (dDAC): A novel device for studying the dynamic-pressure properties of materials. *Review of Scientific Instruments* 78(7), 073904.
- [15] Fei, Y., A. Ricolleau, M. Frank, K. Mibe, G. Shen, & V. Prakapenka (2007). Toward an internally consistent pressure scale. *Proceedings of the National Academy of Sciences* 104(22), 9182–9186.
- [16] French, M. & R. Redmer (2015). Construction of a thermodynamic potential for the water ices VII and X. *Phys. Rev. B* 91, 014308.
- [17] Friedrichs, K. O. (1944). The identity of weak and strong extensions of differential operators. *Transactions of the American Mathematical Society* 55(1), 132–151.

- [18] Geballe, Z. M., H. Liu, A. K. Mishra, M. Ahart, M. Somayazulu, Y. Meng, M. Baldini, & R. J. Hemley (2018). Synthesis and stability of lanthanum superhydrides. *Angewandte Chemie* 130(3), 696–700.
- [19] Giannozzi, P., O. Andreussi, T. Brumme, O. Bunau, M. B. Nardelli, M. Calandra, R. Car, C. Cavazzoni, D. Ceresoli, M. Cococcioni, et al. (2017). Advanced capabilities for materials modelling with QUANTUM ESPRESSO. *Journal of Physics: Condensed Matter* 29(46), 465901.
- [20] Giannozzi, P., S. Baroni, N. Bonini, M. Calandra, R. Car, C. Cavazzoni, D. Ceresoli, G. L. Chiarotti, M. Cococcioni, I. Dabo, et al. (2009). QUANTUM ESPRESSO: a modular and open-source software project for quantum simulations of materials. *Journal of Physics: Condensed Matter* 21(39), 395502.
- [21] Glazyrin, K., L. V. Pourovskii, L. Dubrovinsky, O. Narygina, C. McCammon, B. Hewener, V. Schünemann, J. Wolny, K. Muffler, A. I. Chumakov, W. Crichton, M. Hanfland, V. B. Prakapenka, F. Tasnádi, M. Ekholm, M. Aichhorn, V. Vildosola, A. V. Ruban, M. I. Katsnelson, & I. A. Abrikosov (2013). Importance of Correlation Effects in hcp Iron Revealed by a Pressure-Induced Electronic Topological Transition. *Phys. Rev. Lett.* 110, 117206.
- [22] Goncharov, A. F., V. V. Struzhkin, M. S. Somayazulu, R. J. Hemley, & H. K. Mao (1996). Compression of ice to 210 gigapascals: Infrared evidence for a symmetric hydrogen-bonded phase. *Science* 273(5272), 218–220.
- [23] Goring, R., R. Lukas, & K. Bohmhammel (1981). Multipulse NMR investigation of band structure in titanium hydride: proton Knight shift and spin-lattice relaxation. *Journal of Physics C: Solid State Physics* 14(36), 5675–5687.
- [24] Gustafsson, F. (1996). Determining the initial states in forward-backward filtering. *IEEE Transactions on signal processing* 44(4), 988–992.
- [25] Hirsch, K. R. & W. B. Holzapfel (1986). Effect of high pressure on the Raman spectra of ice VIII and evidence for ice X. *The Journal of Chemical Physics* 84(5), 2771–2775.
- [26] Jenei, Z., H. P. Liermann, R. Husband, A. S. J. Méndez, D. Pennicard, H. Marquardt, E. F. O’Bannon, A. Pakhomova, Z. Konopkova, K. Glazyrin, M. Wendt, S. Wenz, E. E. McBride, W. Morgenroth, B. Winkler, A. Rothkirch, M. Hanfland, & W. J. Evans (2019). New dynamic diamond anvil cells for tera-pascal per second fast compression x-ray diffraction experiments. *Review of Scientific Instruments* 90(6), 065114.
- [27] Journaux, B., R. Caracas, P. Carrez, K. Gouriet, P. Cordier, & I. Daniel (2014). Elasticity and dislocations in ice X under pressure. *Physics of the Earth and Planetary Interiors* 236, 10–15.
- [28] Kim, D. Y., R. H. Scheicher, C. J. Pickard, R. J. Needs, & R. Ahuja (2011). Predicted Formation of Superconducting Platinum-Hydride Crystals under Pressure in the Presence of Molecular Hydrogen. *Phys. Rev. Lett.* 107, 117002.
- [29] Kimmerle, F., G. Majer, U. Kaess, A. Maeland, M. S. Conradi, & A. McDowell (1998). NMR Studies of hydrogen diffusion in ZrBe<sub>2</sub>H<sub>1.4</sub>. *Journal of Alloys and Compounds* 264(1-2), 63–70.
- [30] Klotz, S., K. Komatsu, H. Kagi, K. Kunc, A. Sano-Furukawa, S. Machida, & T. Hattori (2017). Bulk moduli and equations of state of ice-VII and ice-VIII. *Phys. Rev. B* 95, 174111.
- [31] Korringa, J. (1950). Nuclear magnetic relaxation and resonance line shift in metals. *Physica* 16(7-8), 601–610.
- [32] Kuriakose, M., S. Raetz, Q. M. Hu, S. M. Nikitin, N. Chigarev, V. Tournat, A. Bulou,

- A. Lomonosov, P. Djemia, V. E. Gusev, et al. (2017). Longitudinal sound velocities, elastic anisotropy, and phase transition of high-pressure cubic H<sub>2</sub>O ice to 82 GPa. *Physical Review B* 96(13), 134122.
- [33] Li, X., W. Shi, X. Liu, & Z. Mao (2019). High-pressure phase stability and elasticity of ammonia hydrate. *American Mineralogist* 104(9), 1307 – 1314.
- [34] Liermann, H.-P., Z. Konôpková, W. Morgenroth, K. Glazyrin, J. Bednarčík, E. E. McBride, S. Petitgirard, J. T. Delitz, M. Wendt, Y. Bican, A. Ehnes, I. Schwark, A. Rothkirch, M. Tischer, J. Heuer, H. Schulte-Schrepping, T. Kracht, & H. Franz (2015). The Extreme Conditions Beamline P02.2 and the Extreme Conditions Science Infrastructure at PETRA III. *Journal of Synchrotron Radiation* 22(4), 908–924.
- [35] Lin, L., J. A. Morrone, & R. Car (2011). Correlated Tunneling in Hydrogen Bonds. *Journal of Statistical Physics* 145(2), 365–384.
- [36] Liu, H., I. I. Naumov, R. Hoffmann, N. W. Ashcroft, & R. J. Hemley (2017). Potential high-T<sub>c</sub> superconducting lanthanum and yttrium hydrides at high pressure. *Proceedings of the National Academy of Sciences* 114(27), 6990–6995.
- [37] Loubeyre, P., R. LeToullec, E. Wolanin, M. Hanfland, & D. Hausermann (1999). Modulated phases and proton centring in ice observed by X-ray diffraction up to 170 GPa. *Nature* 397, 503–506.
- [38] Majer, G., W. Renz, A. Seeger, R. Barnes, J. Shinar, & A. Skripov (1995). Pulsed-field-gradient nuclear magnetic resonance studies of hydrogen diffusion in Laves-phase hydrides. *Journal of Alloys and Compounds* 231(1-2), 220–225.
- [39] Meier, T., S. Petitgirard, S. Khandarkhaeva, & L. Dubrovinsky (2018). Observation of nuclear quantum effects and hydrogen bond symmetrisation in high pressure ice. *Nature Communications* 9(1), 2766.
- [40] Monserrat, B., S. E. Ashbrook, & C. J. Pickard (2019). Nuclear magnetic resonance spectroscopy as a dynamical structural probe of hydrogen under high pressure. *Phys. Rev. Lett.* 122, 135501.
- [41] Narygina, O., L. S. Dubrovinsky, C. A. McCammon, A. Kurnosov, I. Y. Kantor, V. B. Prakapenka, & N. A. Dubrovinskaia (2011a). X-ray diffraction and Mössbauer spectroscopy study of fcc iron hydride FeH at high pressures and implications for the composition of the Earth’s core. *Earth and Planetary Science Letters* 307(3-4), 409–414.
- [42] Narygina, O., L. S. Dubrovinsky, C. A. McCammon, A. Kurnosov, I. Y. Kantor, V. B. Prakapenka, & N. A. Dubrovinskaia (2011b). X-ray diffraction and Mössbauer spectroscopy study of fcc iron hydride FeH at high pressures and implications for the composition of the Earth’s core. *Earth and Planetary Science Letters* 307(3-4), 409–414.
- [43] Newville, M., T. Stensitzki, D. B. Allen, & A. Ingargiola (2014). LMFIT: Non-Linear Least-Square Minimization and Curve-Fitting for Python. Technical report, 10.5281/zenodo.11813.
- [44] Ong, S. P., W. D. Richards, A. Jain, G. Hautier, M. Kocher, S. Cholia, D. Gunter, V. L. Chevrier, K. A. Persson, & G. Ceder (2013). Python Materials Genomics (pymatgen): A robust, open-source python library for materials analysis. *Computational Materials Science* 68, 314 – 319.
- [45] Peng, F., Y. Sun, C. J. Pickard, R. J. Needs, Q. Wu, & Y. Ma (2017). Hydrogen Clathrate Structures in Rare Earth Hydrides at High Pressures: Possible Route to Room-Temperature Superconductivity. *Phys. Rev. Lett.* 119, 107001.
- [46] Prescher, C. & V. B. Prakapenka (2015). DIOPTAS: a program for reduction of two-

- dimensional X-ray diffraction data and data exploration. *High Pressure Research* 35(3), 223–230.
- [47] Price, W. S. (2009). *NMR studies of translational motion: principles and applications*. Cambridge University Press.
- [48] Pruzan, P., J. C. Chervin, E. Wolanin, B. Canny, M. Gauthier, & M. Hanfland (2003). Phase diagram of ice in the VII-VIII-X domain. Vibrational and structural data for strongly compressed ice VIII. *Journal of Raman Spectroscopy* 34(7-8), 591–610.
- [49] Sano-Furukawa, A., T. Hattori, K. Komatsu, H. Kagi, T. Nagai, J. J. Molaison, A. M. dos Santos, & C. A. Tulk (2018). Direct observation of symmetrization of hydrogen bond in  $\delta$ -AlOOH under mantle conditions using neutron diffraction. *Scientific reports* 8(1), 1–9.
- [50] Somayazulu, M., J. Shu, C.-s. Zha, A. F. Goncharov, O. Tschauner, H.-k. Mao, & R. J. Hemley (2008). In situ high-pressure x-ray diffraction study of H<sub>2</sub>O ice VII. *The Journal of Chemical Physics* 128(6), 064510.
- [51] Sugimura, E., T. Iitaka, K. Hirose, K. Kawamura, N. Sata, & Y. Ohishi (2008). Compression of H<sub>2</sub>O ice to 126 GPa and implications for hydrogen-bond symmetrization: Synchrotron x-ray diffraction measurements and density-functional calculations. *Phys. Rev. B* 77, 214103.
- [52] Sugimura, E., T. Komabayashi, K. Ohta, K. Hirose, Y. Ohishi, & L. S. Dubrovinsky (2012). Experimental evidence of superionic conduction in H<sub>2</sub>O ice. *The Journal of Chemical Physics* 137(19), 194505.
- [53] Thompson, E., A. Davis, W. Bi, J. Zhao, E. Alp, D. Zhang, E. Greenberg, V. Prakapenka, & A. Campbell (2018). High-pressure geophysical properties of fcc phase FeH<sub>x</sub>. *Geochemistry, Geophysics, Geosystems* 19(1), 305–314.
- [54] Tkacz, M., S. Majchrzak, & B. Baranowski (1989). High Pressure X-Ray Diffraction Study of Copper Hydride at Room Temperature. *Zeitschrift für Physikalische Chemie* 163(2), 467–468.
- [55] Wipf, H., B. Kappesser, & R. Werner (2000). Hydrogen diffusion in titanium and zirconium hydrides. *Journal of Alloys and Compounds* 310(1-2), 190–195.
- [56] Wolanin, E., P. Pruzan, J. C. Chervin, B. Canny, M. Gauthier, D. Häusermann, & M. Hanfland (1997). Equation of state of ice VII up to 106 GPa. *Phys. Rev. B* 56, 5781–5785.
- [57] Xiao, X.-H., D.-F. Duan, Y.-B. Ma, H. Xie, H. Song, D. Li, F.-B. Tian, B.-B. Liu, H.-Y. Yu, & T. Cui (2019). Ab initio studies of copper hydrides under high pressure. *Frontiers of Physics* 14(4), 43601.
- [58] Zha, C.-S., J. S. Tse, & W. A. Bassett (2016). New Raman measurements for H<sub>2</sub>O ice VII in the range of 300 cm<sup>-1</sup> to 4000 cm<sup>-1</sup> at pressures up to 120 GPa. *The Journal of Chemical Physics* 145, 124315.
- [59] Zhang, J. S., M. Hao, Z. Ren, & B. Chen (2019). The extreme acoustic anisotropy and fast sound velocities of cubic high-pressure ice polymorphs at Mbar pressure. *Applied Physics Letters* 114(19), 191903.



## Chapter 5

# Manuscripts



## 5.1 Proton Dynamics in High-Pressure Ice-VII

The following section contains the manuscript:

*„Proton Dynamics in High-Pressure Ice-VII from Density Functional Theory“*

Florian Trybel, Michael Cosacchi, Thomas Meier, Vollrath Martin Axt  
and Gerd Steinle-Neumann

Status: Submitted to *Physical Review Letters*

(30 June 2020)

and the related supplementary material.

## Proton dynamics in high-pressure ice-VII from density functional theory

Florian Trybel,<sup>1,\*</sup> Michael Cosacchi,<sup>2</sup> Thomas Meier,<sup>1</sup> Vollrath Martin Axt,<sup>2</sup> and Gerd Steinle-Neumann<sup>1</sup>

<sup>1</sup>*Bayerisches Geoinstitut, Universität Bayreuth, D-95440 Bayreuth, Germany*

<sup>2</sup>*Theoretische Physik III, Universität Bayreuth, D-95440 Bayreuth, Germany*

(Dated: June 30, 2020)

Using a density-functional-theory-based approach, we explore the symmetrization and proton dynamics in ice-VII, for which recent high-pressure NMR experiments indicate significant proton dynamics in the pressure-range of 20–95 GPa. We directly sample the potential seen by the proton and find a continuous transition from double- to single-well character over the pressure range of 2 to 130 GPa accompanied by proton dynamics in agreement with the NMR experiments.

PACS numbers: 71.15.Mb, 63.20.dk, 61.50.Ks, 62.50.-p

The discovery of an ice-VII inclusion in a diamond [1] from the Earth’s mantle highlights the importance of this high-pressure phase of water for planetary interiors beyond the icy satellites of Jupiter and Saturn in our solar system [2, 3], and potentially H<sub>2</sub>O-dominated exosolar planets [4, 5]. At room temperature ( $T$ ), water crystallizes as ice-VII at pressures ( $P$ ) above 2 GPa in a cubic structure (spacegroup Pn $\bar{3}$ m), based on a body centered cubic ( $bcc$ ) arrangement of oxygens with two possible proton positions along the diagonal O-O direction (dOOd) that are occupied randomly (Fig. 1 in the Supp. Matt.), but assumed to follow the ice-rules [6] [7]. With increasing  $P$ , the O-H $\cdots$ O bond continuously symmetrizes to form ice-X, a process that has been of great interest in high- $P$  physics and chemistry [8–25]. In ice-VII a double-well potential along the O-O direction can be found under correlated proton movement [14, 21] which changes significantly under compression. This double-well potential provides the basis for proton dynamics, recently observed with nuclear magnetic resonance (NMR) experiments in the diamond anvil cell [26]. Although numerous studies have investigated the properties of high- $P$  ice-VII for more than 35 years [8], no consensus on the symmetrization  $P$  has emerged. Proton dynamics and the underlying potential have been calculated from computationally expensive path-integral based simulations at individual  $P$  conditions only [21] ([27] for hexagonal ice), or indirectly from density-functional-theory (DFT) based approaches [16, 18, 20, 25]. Using Kohn-Sham (KS) DFT [28], we trace the potential by displacing all, six and a single proton along dOOd, to investigate proton dynamics and explore symmetrization under compression.

We build an ice-VII cell with 384 atoms (lattice constant  $l = 3.35$  Å), following the ice-rules [6]. All protons are simultaneously moved by the same amount along the respective O-O diagonal (22 steps), calculated energies are interpolated with a third-order spline, and the optimal proton position at each  $l$  is determined. We obtain a double-well potential (characterized by an energy barrier  $\Phi_m$  and the distance between minimum location and the center of the O-O diagonal,  $\delta_c$ ) at low compression (Fig. 1) and observe a continuous transition to a single well

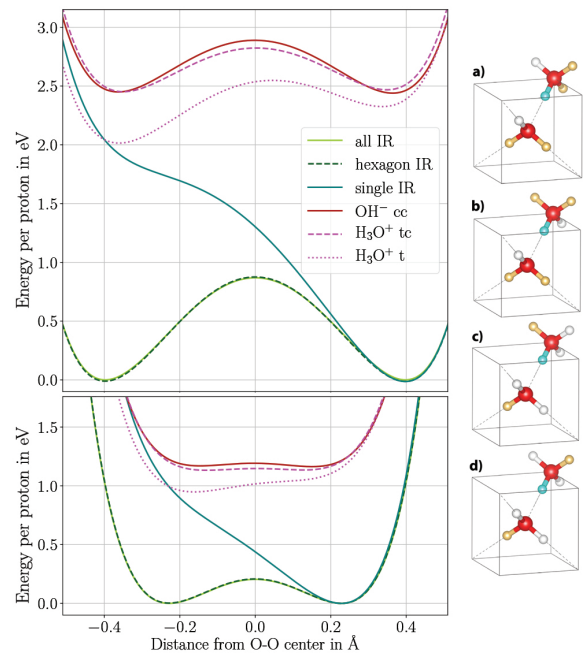


FIG. 1. Energy of different proton configurations for  $l = 3.35$  Å (top) and  $l = 2.95$  Å (bottom) and a-d) visualization of possible configurations with a single-proton ice-rule (IR) violation: Oxygen is shown in red, unoccupied hydrogen positions in white, occupied hydrogen positions in yellow and sampled hydrogen in teal: a) H<sub>3</sub>O<sup>+</sup> in cis configuration (cis-H<sub>3</sub>O<sup>+</sup>), b) trans-H<sub>3</sub>O<sup>+</sup>, c) cis-OH<sup>-</sup> and d) trans-OH<sup>-</sup>. Potentials displayed are for the collective motion of protons (all), the collective hexagonal configuration (hexagon) and a single proton (single), all obeying IR. Potentials for the IR-breaking arrangements are trans-H<sub>3</sub>O<sup>+</sup> (t), without and with conjugation (tc) of the associated charge defect, and cis-OH<sup>-</sup> in the conjugated configuration (cc). conjugated trans-H<sub>3</sub>O<sup>+</sup> and conjugated cis-OH<sup>-</sup> are shown as they bracket the potential of all conjugated IR-breaking structures.

with decreasing  $l$  (Fig. 2 in the Supp. Mat.). In the following, the optimized proton position obtained from the collective displacement of all protons at the respective  $l$  is used as the reference position, when only some protons are considered.

Moving a single proton along dOoD in the ice-rule conforming cell leads to an asymmetric single-well potential, with the minimum corresponding to one of the minima in the double-well obtained from the collective displacement of all protons (Fig. 1), and, once the double-well character is lost, converges to the same potential (Fig. 3 in the Supp. Mat.).

In previous path integral based studies [21], a collective motion of six protons in a hexagonal configuration was identified without breaking the ice-rules. We follow this suggestion and move six protons in such a configuration (Fig. 1 in the Supp. Mat.), while the others remain at the optimized position for the respective  $l$ . We obtain potentials almost perfectly corresponding to the all-proton case in terms of energy/proton (Fig. 1), with the double-well character steadily decreasing with decreasing  $l$  (Fig. 2). Under further compression, the high- $P$  single-well becomes increasingly localized (Fig. 4 in the Supp. Mat.). The potentials show a slight asymmetry caused by the non-central position of the hexagon in the simulation cell in combination with periodic boundary conditions.

By breaking the ice-rules, it is possible to create environments in which a single proton experiences a double-well potential when moved along the O-O diagonal. Four different cases of ice-rule breaking configurations (Fig. 1) can be distinguished based on the oxygen-proton ratio,  $\text{OH}^-$  and  $\text{H}_3\text{O}^+$ , and different configuration, i.e., (rotational) symmetry: (pseudo-)cis with protons aligned along dOoD, and trans with protons facing each other. Due to a violation of local charge neutrality, the potentials of all  $\text{OH}^-$  and  $\text{H}_3\text{O}^+$  configurations are higher in energy and asymmetric, as illustrated explicitly for trans- $\text{H}_3\text{O}^+$  in Fig. 1. To mitigate the asymmetry, we conjugate the charge defect along a path of water molecules to the edge of the simulation cell to minimize its influence (Fig. 1 of the Supp. Mat.) (*cf.* Figs. 5 and 6 in Supp. Mat. for the potentials).

Comparing  $\delta_c$  and  $\Phi_m$  for all six cases discussed above (Fig. 2), we find a splitting into two groups: Ice-rule violating structures lose the double-well character at a smaller compression,  $l \lesssim 2.8 - 2.85 \text{ \AA}$ , compared to the ice-rule conforming structures,  $l \lesssim 2.675 \text{ \AA}$  [29]. Nevertheless, the functional behavior of both parameters with compression, expressed in terms of lattice parameter  $l$ , is similar for all cases - following a quadratic function for  $\Phi_m$  and a square root for  $\delta_c$  (Fig. 2) [30]. Comparing the double-well potential from the path-integral simulations in Lin *et al.* [21] with our results, their  $\delta_c$  is in very good agreement with the hexagonal configuration;  $\Phi_m$  is larger in our calculations, with the difference most likely caused by their calculations being ensemble calculations

in contrast to our individual configuration approach and – more importantly – the classical treatment of protons in our calculations to this point.

Temperature has been neglected in the evaluation of the potentials. As we create unstable configurations during sampling, harmonic lattice dynamics simulations would show negative phonon modes, and in molecular dynamics the structure would fall back to an equilibrium. The good agreement between the path integral results [21] and our calculations with respect to  $\delta_c$  suggests that vibrational effects do not influence the width of the potential significantly. By evaluating results as a function of  $l$  and not  $P$ , thermal expansion does not influence the outcome. In order to compare to experimental data recorded as function of  $P$  rather than  $l$  and to include thermal expansion, we use the thermal equation of state by French and Redmer [22] to transform  $l$  to  $P$  at 300 K.

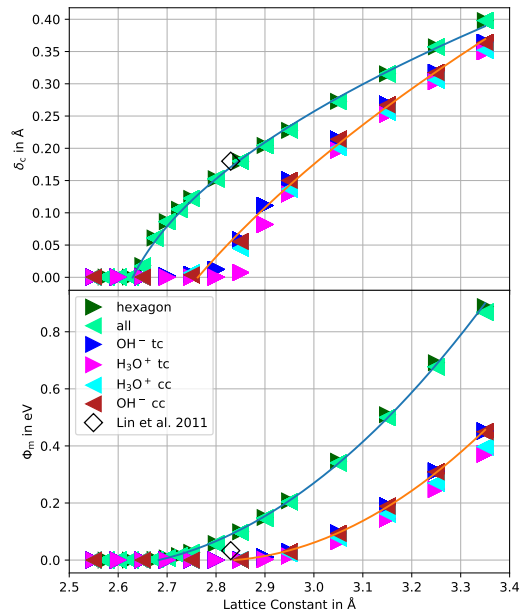


FIG. 2. Parameters describing the structure of the double-well potential as a function of lattice parameter  $l$ . (**top**)  $\delta_c$ , the distance between the center of the double-well and the minima. (**bottom**)  $\Phi_m$ , the height of the barrier. Solid lines are fits of a square root for  $\delta_c$  and a quadratic function for  $\Phi_m$  to the hexagonal (green) and trans- $\text{OH}^-$  points (orange). Black diamonds show result of path integral *ab-initio* molecular dynamics simulations at  $l = 2.84 \text{ \AA}$  [21].

Many high- $P$  techniques do not provide access to the potential itself, but the electron density close to the protons by X-rays [12, 15, 31, 32], and the response of the lattice to an excitation of phonon modes by Raman/infrared [10, 12, 33–35] or Brillouin [19] spectroscopy can be mea-

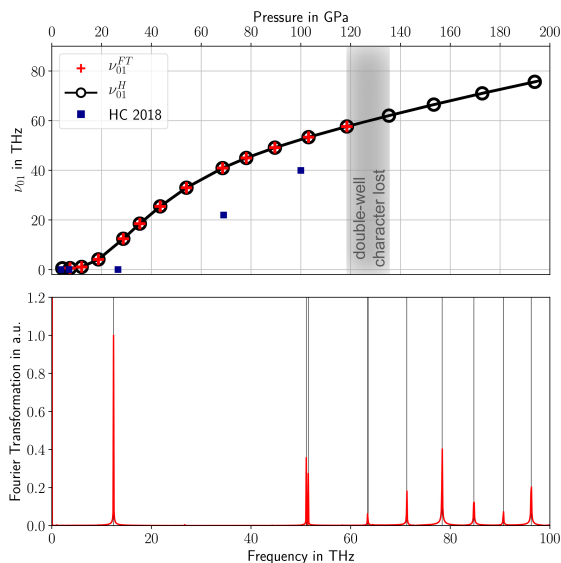


FIG. 3. Results of the dynamical calculation for the hexagonal configuration. **(bottom)** Transition frequency spectrum calculated from the eigenvalues of the Hamiltonian (black vertical lines) and the solution to the dynamic problem, represented by the Fourier transformation of the probability of finding the proton in the left side of the potential,  $p(k)$ , with amplitudes normalized to  $\nu_{01}$  (red) for  $l = 2.95$  Å. **(top)**  $\nu_{01}^H$  from the eigenvalue analysis (black circles) and position of  $\nu_{01}^{FT}$  in  $p(k)$  (red crosses) as a function of  $P$ . Dark blue squares show hydrogen jump rates calculated by Hernandez and Caracas [25] (HC 2018) on the basis of molecular dynamics simulations.

sured at high  $P$ . High- $P$  NMR, by contrast, enables the investigation of effective proton dynamics [26] by performing a line-shape analysis. In order to compare with the latter results, we use a matrix exponential formalism to solve the time ( $t$ ) dependent Schrödinger equation for a wave packet in the respective one-dimensional potentials obtained from the DFT-based sampling (see Supp. Mat. for details). The initial state is described by a generic 1D-Gaussian of the form

$$\Psi = \mathcal{I}^{-1} \cdot \mathcal{F}\left(\frac{x-x_0}{3a}\right) \cdot \frac{1}{\sqrt{a\sqrt{\pi}}} \exp\left(-0.5\left(\frac{x-x_0}{a}\right)^2\right), \quad (1)$$

where  $\hbar$  is the reduced Planck constant,  $x$  the position along dOOD,  $a$  and  $x_0$  the width and center of the Gaussian,  $m$  the proton mass;  $\mathcal{I}$  ensures normalization and  $\mathcal{F}$  is a mollifier [36], improving the localization of  $\Psi$ , leading to a significant speed-up and higher stability of the numerics, without affecting any physical features.

We assume that through spontaneous symmetry break-

ing the protons are located at one of the minima at  $t_0$  and therefore choose the initial state such that  $x_0$  coincides with one of the minima of the potential for each  $l$ , respectively.

An eigenvalue analysis of the Hamiltonian is helpful to understand the idea behind this choice with respect to the analysis of effective single-particle dynamics and the spectral features. If we construct the initial state as a superposition of the two lowest eigenstates, it is straightforward to show that the resulting wave packet oscillates between the minima with a frequency exactly corresponding to the difference in energies of both eigenstates ( $\nu_{01}^H$ ), representing the tunnelling frequency. As the eigenstates of the Hamiltonian are a basis set, any initial state can be decomposed into them, and the resulting dynamics includes all frequencies ( $\nu^H$ ) which correspond to the combinatorically possible differences between their energies. While exactly diagonalizing the Hamiltonian yields all  $\nu^H$  taking part in the dynamics, solving the problem with a physically motivated initial state additionally provides access to amplitudes.

We calculate the  $t$ -evolution of  $\Psi$  with respect to the potentials of the hexagonal as well as the four ice-rule violating configurations [37]. In each  $t$ -step, the probability of finding the proton in the left half of the double-well potential is given by  $p(x < 0) = \int_{-\infty}^0 |\Psi(x)|^2 dx$  (Fig. 7 of the Supp. Mat.). The Fourier transform of  $p(x < 0)$ ,  $p(k)$ , results in a  $\nu^{FT}$ -spectrum that perfectly coincides with the transitions based on the Hamiltonian (Fig. 3 for the hexagonal configuration), which can be seen as a check for the solver, in addition to energy and norm conservation.

Choosing  $x_0$  for the initial state as the minimum of the respective potential leads to a non-zero overlap between the ground state and the first excited state and therefore  $\nu_{01}^{FT} > 0$  as long as  $x_0$  is not central. Once the minimum of the potential, and consequently  $x_0$ , is at the center of dOOD, no overlap between the ground state (symmetric) and the first excited state (antisymmetric) is expected, and the amplitude of  $\nu_{01}^{FT}$  should vanish, indicating the completion of symmetrization.

The frequency  $\nu_{01}^H$ , calculated from the eigenvalues, increases with  $P$  in a square root-like fashion between 5 and  $\sim 100$ -120 GPa and linearly upon further  $P$ -increase to our maximum  $P \approx 200$  GPa (Fig. 3 for the hexagonal configuration). This change in slope indicates a change in dynamical behaviour independent of the particular form of the initial state, providing an additional (although less sensitive) analysis tool, and shows that the exact form of  $\Psi$ , in particular the addition of  $\mathcal{F}$ , only improves the analysis, but is not required.  $\nu_{01}^{FT}$ , calculated from  $p(k)$ , follows this trend to  $P \lesssim 130$  GPa, where we find a significant drop in amplitude (Fig. 4), suggesting that the  $\nu_{01}$  oscillation is no longer contributing to the dynamics of the system.

Proton jump frequencies calculated by Hernandez and

Caracas [25] are in quantitative agreement with our results for the hexagonal configuration, but shifted to slightly higher  $P$ , which is most likely a consequence of their classical treatment of the problem. The occupation of  $\nu_{01}^{FT}$  for the ice-rule violating configuration drops at a lower  $P$  (Fig. 4), reflecting the earlier transition to a single-well potential (Fig. 2).

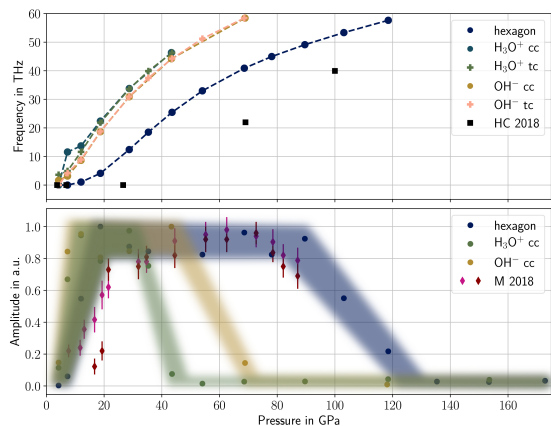


FIG. 4. **(top)** Excitation frequencies  $\nu_{01}^{FT}$  as a function of  $P$  at 300 K for the different proton configurations explored in this study. Black squares show hydrogen jump rates calculated by Hernandez and Caracas [25] (HC 2018) on the basis of molecular dynamics simulations. **(bottom)** Corresponding amplitudes of  $\nu_{01}^{FT}$  in  $p(k)$ . Amplitudes are normalized to the maximum value for the respective configuration [38]. Diamonds in magenta and purple show the result of a peak analysis of NMR experiments by Meier *et al.* [26] (M 2018).

If we compare the amplitude of  $\nu_{01}^{FT}$  in  $p(k)$  as a function of  $P$  with results by Meier *et al.* [26] (Fig. 4), we find that the hexagonal configuration reproduces the  $P$ -dependence of the NMR line-shape analysis at room  $T$  well: A strong increase in amplitude up to  $P \sim 20$  GPa, a plateau to  $P \sim 80 - 90$  GPa, and a subsequent drop. This supports the interpretation of Lin *et al.* [21] that charge balance tends to be maintained at low  $T$ , and therefore tunneling is correlated, represented by the hexagonal configuration.

We do not find a sharp phase transition in cubic ice between the emergence of ice-VII at  $\sim 2$  GPa and 200 GPa, well in the stability field of ice-X, but a gradual change from a double- to a single-well potential, and we predict related changes in proton dynamics. Based on our results we can distinguish regions of characteristic proton dynamics and potential (at room  $T$ ):

- (i) For  $2 \text{ GPa} < P < 20 \text{ GPa}$ , protons become increasingly delocalized, as the potential barrier decreases;
- (ii) for  $20 \text{ GPa} < P < 90 \text{ GPa}$ , protons tunnel in a

fashion well represented by correlated hexagons;

- (iii) for  $90 \text{ GPa} < P < 130 \text{ GPa}$ , symmetrization occurs and the amplitude of  $\nu_{01}^{FT}$  drops significantly as the potential barrier becomes small, but non-zero;
- (iv) for  $P \gtrsim 130 \text{ GPa}$ , the potential is fully symmetric and no proton dynamics is expected for an initially symmetric state.

In  $P$ -ranges (i) and (iii), varying energy and momentum transfer to the sample by different experimental methods may modify the probed potential, ranging from an excitation of the proton spin system without significant momentum or energy transfer to the lattice in NMR [26], through momentum transfer by collisions with neutrons [24], the excitation of lattice vibrations in Raman [33–35], infrared [10] and Brillouin [19, 39, 40] spectroscopy, to high-energy irradiation with X-rays [12, 15, 31, 32]. Based on this observation we suggest that experimental methods can be expected not to agree on a single transition  $P$  in a system like  $H_2O$  ice. Further, the limited experimental resolution in terms of  $P$ -sampling may lead to an over-interpretation of the nature of the phase transition, in some cases leading to the claim of a sharp transition [10, 32, 41].

## ACKNOWLEDGMENTS

FT and GSN were supported by Deutsche Forschungsgemeinschaft (DFG) within FOR 2440 (Matter under Planetary Interior Conditions) with grant STE1105/13 and TM with grant ME5206/3-1. We thank F. Ungar (TP III, Universität Bayreuth) for very helpful discussions. Computations were partly performed at the Leibniz Supercomputing Centre of the Bavarian Academy of Sciences and the Humanities. GPU accelerated computations are supported via an NVIDIA GPU Grant.

\* f.trybel@uni-bayreuth.de

- [1] O. Tschauner, S. Huang, E. Greenberg, V. B. Prakapenka, C. Ma, G. R. Rossman, A. H. Shen, D. Zhang, M. Newville, A. Lanzirotti, and K. Tait, *Science* **359**, 1136 (2018).
- [2] F. Nimmo and R. T. Pappalardo, *Journal of Geophysical Research: Planets* **121**, 1378 (2016).
- [3] M. K. Dougherty and L. J. Spilker, *Reports on Progress in Physics* **81**, 065901 (2018).
- [4] D. Valencia, D. D. Sasselov, and R. J. O’Connell, *The Astrophysical Journal* **665**, 14131420 (2007).
- [5] J. Monteux, G. J. Golabek, D. C. Rubie, G. Tobie, and E. D. Young, *Space Science Reviews* **214**, 39 (2018).
- [6] J. D. Bernal and R. H. Fowler, *The Journal of Chemical Physics* **1**, 515 (1933).

- [7] Each oxygen atom is covalently bound to two hydrogen atoms and each resulting water-like unit forms two hydrogen bonds to other oxygen atoms.
- [8] A. Polian and M. Grimsditch, *Phys. Rev. Lett.* **52**, 1312 (1984).
- [9] C. Lee, D. Vanderbilt, K. Laasonen, R. Car, and M. Parrinello, *Phys. Rev. B* **47**, 4863 (1993).
- [10] A. F. Goncharov, V. V. Struzhkin, M. S. Somayazulu, R. J. Hemley, and H. K. Mao, *Science* **273**, 218 (1996).
- [11] K. Aoki, H. Yamawaki, M. Sakashita, and H. Fujihisa, *Phys. Rev. B* **54**, 15673 (1996).
- [12] E. Wolanin, P. Pruzan, J. C. Chervin, B. Canny, M. Gauthier, D. Häusermann, and M. Hanfland, *Phys. Rev. B* **56**, 5781 (1997).
- [13] M. Bernasconi, P. L. Silvestrelli, and M. Parrinello, *Phys. Rev. Lett.* **81**, 1235 (1998).
- [14] M. Benoit, D. Marx, and M. Parrinello, *Nature* **392**, 258 (1998).
- [15] P. Loubeyre, R. LeToullec, E. Wolanin, M. Hanfland, and D. Hausermann, *Nature* **397**, 503 (1999).
- [16] M. Benoit, A. H. Romero, and D. Marx, *Phys. Rev. Lett.* **89**, 145501 (2002).
- [17] E. Sanz, C. Vega, J. L. F. Abascal, and L. G. MacDowell, *Phys. Rev. Lett.* **92**, 255701 (2004).
- [18] R. Caracas, *Phys. Rev. Lett.* **101**, 085502 (2008).
- [19] Y. Asahara, K. Hirose, Y. Ohishi, N. Hirao, and M. Murakami, *Earth and Planetary Science Letters* **299**, 474 (2010).
- [20] X. Z. Lu, Y. Zhang, P. Zhao, and S. J. Fang, *The Journal of Physical Chemistry B* **115**, 71 (2011).
- [21] L. Lin, J. A. Morrone, and R. Car, *Journal of Statistical Physics* **145**, 365 (2011).
- [22] M. French and R. Redmer, *Phys. Rev. B* **91**, 014308 (2015).
- [23] J. Tsuchiya and T. Tsuchiya, *The Journal of Chemical Physics* **146**, 014501 (2017).
- [24] S. Klotz, K. Komatsu, H. Kagi, K. Kunc, A. Sano-Furukawa, S. Machida, and T. Hattori, *Phys. Rev. B* **95**, 174111 (2017).
- [25] J.-A. Hernandez and R. Caracas, *The Journal of Chemical Physics* **148**, 214501 (2018).
- [26] T. Meier, S. Petitgirard, S. Khandarkhaeva, and L. Dubrovinsky, *Nature Communications* **9**, 2766 (2018).
- [27] C. Drechsel-Grau and D. Marx, *Physical Chemistry Chemical Physics* **19**, 2623 (2017).
- [28] All KS-DFT-based calculations are performed with QUANTUM ESPRESSO 6.1 [42, 43], where possible using GPU-acceleration [44]. We use the optBK88-vdW [45–51] approximation to exchange and correlation as found most suitable for various water properties [52]. Convergence tests with a threshold of  $10^{-4}$  Ry lead to a Monkhorst-Pack k-point grid [53] of  $1 \times 1 \times 1$  for the 384 atom cells and a cutoff energy for plane wave expansion of 130 Ry. VESTA 3 [54] is used for structural visualizations.
- [29] The respective potentials can be found in the Supp. Mat., Supp. Fig. 2-6.
- [30] Fit function from Fig. 2: Hexagon/all:  $1.42(x - 2.54)^2 - 0.03$ ,  $0.57(x - 2.59)^{0.5} - 0.10$  and trans- $\text{H}_3\text{O}^+$ :  $1.46(x - 2.79)^2 - 0.003$ ,  $0.90(x - 2.49)^{0.5} - 0.46$ .
- [31] M. Somayazulu, J. Shu, C.-s. Zha, A. F. Goncharov, O. Tschauer, H.-k. Mao, and R. J. Hemley, *The Journal of Chemical Physics* **128**, 064510 (2008).
- [32] E. Sugimura, T. Iitaka, K. Hirose, K. Kawamura, N. Sata, and Y. Ohishi, *Phys. Rev. B* **77**, 214103 (2008).
- [33] K. R. Hirsch and W. B. Holzapfel, *The Journal of Chemical Physics* **84**, 2771 (1986).
- [34] P. Pruzan, J. C. Chervin, E. Wolanin, B. Canny, M. Gauthier, and M. Hanfland, *Journal of Raman Spectroscopy* **34**, 591 (2003).
- [35] C.-S. Zha, J. S. Tse, and W. A. Bassett, *The Journal of Chemical Physics* **145**, 124315 (2016).
- [36] K. O. Friedrichs, *Transactions of the American Mathematical Society* **55**, 132 (1944).
- [37] The potential for the collective movement of all protons is not evaluated as the combined energy barrier of all protons in the system is significantly higher than for the hexagonal collective movement.
- [38] For the hexagonal configuration, the point at  $l = 2.85$  Å is missing, as the peak in the spectrum is not sufficiently resolved by the discrete calculation grid.
- [39] M. Ahart, M. Somayazulu, S. A. Gramsch, R. Boehler, H.-k. Mao, and R. J. Hemley, *The Journal of Chemical Physics* **134**, 124517 (2011).
- [40] J. S. Zhang, M. Hao, Z. Ren, and B. Chen, *Applied Physics Letters* **114**, 191903 (2019).
- [41] E. Sugimura, T. Komabayashi, K. Ohta, K. Hirose, Y. Ohishi, and L. S. Dubrovinsky, *The Journal of Chemical Physics* **137**, 194505 (2012).
- [42] P. Giannozzi, S. Baroni, N. Bonini, M. Calandra, R. Car, C. Cavazzoni, D. Ceresoli, G. L. Chiarotti, M. Cococcioni, I. Dabo, A. Dal Corso, S. de Gironcoli, S. Fabris, G. Fratesi, R. Gebauer, U. Gerstmann, C. Gougoussis, A. Kokalj, M. Lazzeri, L. Martin-Samos, N. Marzari, F. Mauri, R. Mazzarello, S. Paolini, A. Pasquarello, L. Paulatto, C. Sbraccia, S. Scandolo, G. Sclauzero, A. P. Seitsonen, A. Smogunov, P. Umari, and R. M. Wentzcovitch, *Journal of Physics: Condensed Matter* **21**, 395502 (2009).
- [43] P. Giannozzi, O. Andreussi, T. Brumme, O. Bunau, M. B. Nardelli, M. Calandra, R. Car, C. Cavazzoni, D. Ceresoli, M. Cococcioni, N. Colonna, I. Carnimeo, A. D. Corso, S. de Gironcoli, P. Delugas, R. A. D. Jr., A. Ferretti, A. Floris, G. Fratesi, G. Fugallo, R. Gebauer, U. Gerstmann, F. Giustino, T. Gorni, J. Jia, M. Kawamura, H.-Y. Ko, A. Kokalj, E. Küçükbenli, M. Lazzeri, M. Marsili, N. Marzari, F. Mauri, N. L. Nguyen, H.-V. Nguyen, A. O. de-la Roza, L. Paulatto, S. Poncé, D. Rocca, R. Sabatini, B. Santra, M. Schlipf, A. P. Seitsonen, A. Smogunov, I. Timrov, T. Thonhauser, P. Umari, N. Vast, X. Wu, and S. Baroni, *Journal of Physics: Condensed Matter* **29**, 465901 (2017).
- [44] J. Romero, E. Phillips, G. Ruetsch, M. Fatica, F. Spiga, and P. Giannozzi, in *International Workshop on Performance Modeling, Benchmarking and Simulation of High Performance Computer Systems* (2017).
- [45] A. D. Becke, *Phys. Rev. A* **38**, 3098 (1988).
- [46] M. Dion, H. Rydberg, E. Schröder, D. C. Langreth, and B. I. Lundqvist, *Phys. Rev. Lett.* **92**, 246401 (2004).
- [47] T. Thonhauser, V. R. Cooper, S. Li, A. Puzder, P. Hyldgaard, and D. C. Langreth, *Phys. Rev. B* **76**, 125112 (2007).
- [48] D. C. Langreth, B. I. Lundqvist, S. D. Chakarova-Käck, V. R. Cooper, M. Dion, P. Hyldgaard, A. Kelkkanen, J. Kleis, L. Kong, S. Li, *et al.*, *Journal of Physics: Condensed Matter* **21**, 084203 (2009).
- [49] J. Klimeš, D. R. Bowler, and A. Michaelides, *Journal of Physics: Condensed Matter* **22**, 022201 (2010).

- [50] T. Thonhauser, S. Zuluaga, C. A. Arter, K. Berland, E. Schröder, and P. Hyldgaard, *Phys. Rev. Lett.* **115**, 136402 (2015).
- [51] K. Berland, V. R. Cooper, K. Lee, E. Schröder, T. Thonhauser, P. Hyldgaard, and B. I. Lundqvist, *Reports on Progress in Physics* **78**, 066501 (2015).
- [52] M. J. Gillan, D. Alfè, and A. Michaelides, *The Journal of Chemical Physics* **144**, 130901 (2016).
- [53] H. J. Monkhorst and J. D. Pack, *Phys. Rev. B* **13**, 5188 (1976).
- [54] K. Momma and F. Izumi, *Journal of Applied Crystallography* **44**, 1272 (2011).

**Supplementary Material:**  
**Proton dynamics in high-pressure ice-VII from density functional theory**

Florian Trybel,<sup>1,\*</sup> Michael Cosacchi,<sup>2</sup> Thomas Meier,<sup>1</sup> Vollrath Martin Axt,<sup>2</sup> and Gerd Steinle-Neumann<sup>1</sup>

<sup>1</sup>*Bayerisches Geoinstitut, Universität Bayreuth, D-95440 Bayreuth, Germany*

<sup>2</sup>*Theoretische Physik III, Universität Bayreuth, D-95440 Bayreuth, Germany*

(Dated: June 30, 2020)

PACS numbers: 71.15.Mb, 63.20.dk, 61.50.Ks, 62.50.-p

### Potential Sampling

We trace the potential by displacing collectively all (Figure 2), six (in a hexagonal configuration, Figure 3) and a single proton (Figure 4-6) along the diagonal oxygen-oxygen direction (dOOd). In order to sample the different configurations, we choose the atoms closest to the center of the cell with the goal to minimize effects of the periodic boundary conditions (Figure 1) and obtain potentials shown in Figure 3-6. In the case of ice-rule violating structures involving  $\text{H}_3\text{O}^+$  and  $\text{OH}^-$  units, a strongly asymmetric potential is obtained. The asymmetry is caused by a violation of local charge balance as a consequence of breaking the ice-rules. In order to obtain nearly symmetric potentials, we conjugate the proton defect to the edge of the simulation cell along a path of oxygen atoms (blue) by moving the protons (yellow) accordingly (Figure 1). Resulting potentials (shifted to a common energetic zero) as a function of the lattice constant (discussed in detail in the main text) can be found in Figures 2-6.

### Numerical Approach to Solving Schrödinger's Equation for Proton Tunnelling

A python program is used to calculate the tunnelling frequencies solving the time-dependent Schrödinger equation in one dimension (1D) for a particle in an arbitrary potential. It is inspired by the pySchrodinger <https://github.com/jakevdp/pySchrodinger> code of Jake Vanderplas [1], but uses a matrix exponential formalism instead of a Fourier solver for the time propagation of the wave-function:

$$\Psi(x_i, t_{i+1}) = \exp\left(-\frac{i}{\hbar}\mathcal{H}(x_i)\Delta t\right)\Psi(x_i, t_i), \quad (1)$$

with

$$\mathcal{H} = -\frac{\hbar^2}{2m_p}\mathcal{D}(x_i) + \Phi(x_i), \quad (2)$$

where  $\mathcal{D}$  is the matrix representation of the 3rd order central difference scheme with a stencil reduction at the boundaries, and  $\Phi$  the diagonal matrix constructed from the 1D potential and its continuously differentiable

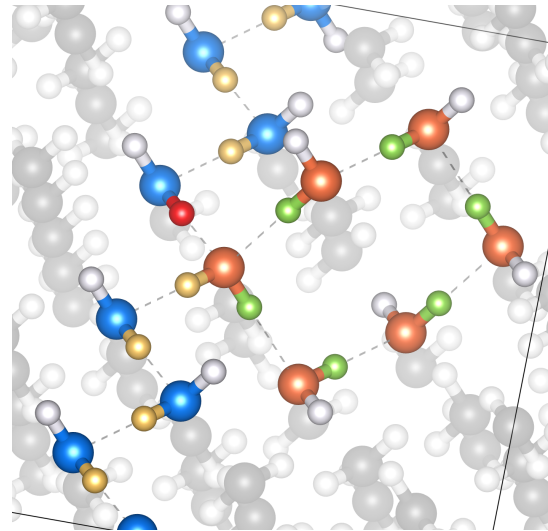


FIG. 1. Cut through the 4x4x4 ice-VII supercell. The sampling of the correlated hexagonal configuration is performed by moving the green protons in the ring of orange oxygen atoms. For the single proton sampling, the red proton is moved. To provide local charge neutrality, the ice-rule violating defects for the  $\text{OH}^-$  and  $\text{H}_3\text{O}^+$  configurations are moved to the edge of the simulation cell, along a path similar to the blue oxygen atoms.

continuation. In each  $t$ -step, the probability of finding the proton in the left half of the double well potential  $p(x < 0) = \int_{-\infty}^0 |\Psi(x)|^2 dx$  is calculated, and energy as well as norm conservation is checked.

### The Potential

The volume-dependent potential seen by the proton ( $\phi_x(V_i, x_i)$ ) is calculated stepwise for different cells, where the respective number of protons is moved to position  $x_i$  along dOOd. The calculated energies per proton are interpolated via a cubic spline, leading to  $\phi_x^s(V_i, x)$ . At small O-H distances (high energies), the DFT calculations are not reliably converging, therefore  $\phi_x^s(V_i, x)$  is extended using a 1D approximation to the Pauli-repulsion

potential  $\phi_P$  at small inter-ionic distances, such that the potential is twice continuously differentiable. We approximate  $\phi_P$  as

$$\phi_P = \left( \frac{\alpha}{x - x_0} \right)^{12}. \quad (3)$$

In order to construct a continuously differentiable continuation of the spline, it is necessary to satisfy the conditions

$$\phi_x^s(\pm x_m) = \phi_P(\pm x_m), \quad (4a)$$

$$\left. \frac{\partial \phi_x^s(x)}{\partial x} \right|_{\pm x_m} = \left. \frac{\partial \phi_P(x)}{\partial x} \right|_{\pm x_m}, \quad (4b)$$

where  $\pm x_m$  is the last point at which  $\phi_x^s$  is calculated explicitly. This leads to parameters  $\alpha$  and  $x_0$  in (3) being:

$$\alpha = \mp 12 \left( \left. \frac{\partial \phi_x^s(x)}{\partial x} \right|_{\pm x_m} \right)^{-1} \phi_x^s(\pm x_m)^{13/12}, \quad (5a)$$

$$x_0 = \pm x_m \pm 12 \left( \left. \frac{\partial \phi_x^s(x)}{\partial x} \right|_{\pm x_m} \right)^{-1} \phi_x^s(\pm x_m). \quad (5b)$$

### Initial State

In order to improve the localization of the initial state described in equation (1) of the main text, a mollifier of

the form

$$\mathcal{F}(z) = \begin{cases} \frac{1}{c_n} \exp((z^2 - 1)^{-1}), & \text{if } |z| < 1, \\ 0, & \text{if } |z| \geq 1, \end{cases} \quad (6)$$

with  $z = \frac{x - x_0}{3a}$  and  $c_n$  ensuring normalization of  $\mathcal{F}(z)$ , is used, and the proton is finally represented by

$$\Psi(V, T, x) = \mathcal{I}^{-1} \cdot \mathcal{F}\left(\frac{x - x_0}{3a}\right) \cdot \mathcal{G}(V, T, x), \quad (7)$$

$$\mathcal{I} = \int_X \left| \mathcal{F}\left(\frac{x - x_0}{3a}\right) \cdot \mathcal{G}(V, T, x) \right|^2 dx. \quad (8)$$

---

\* f.trybel@uni-bayreuth.de

- [1] WRF Data Science Studio, University of Washington.
- [2] L. Lin, J. A. Morrone, and R. Car, *Journal of Statistical Physics* **145**, 365 (2011).
- [3] C. Drechsel-Grau and D. Marx, *Physical Chemistry Chemical Physics* **19**, 2623 (2017).

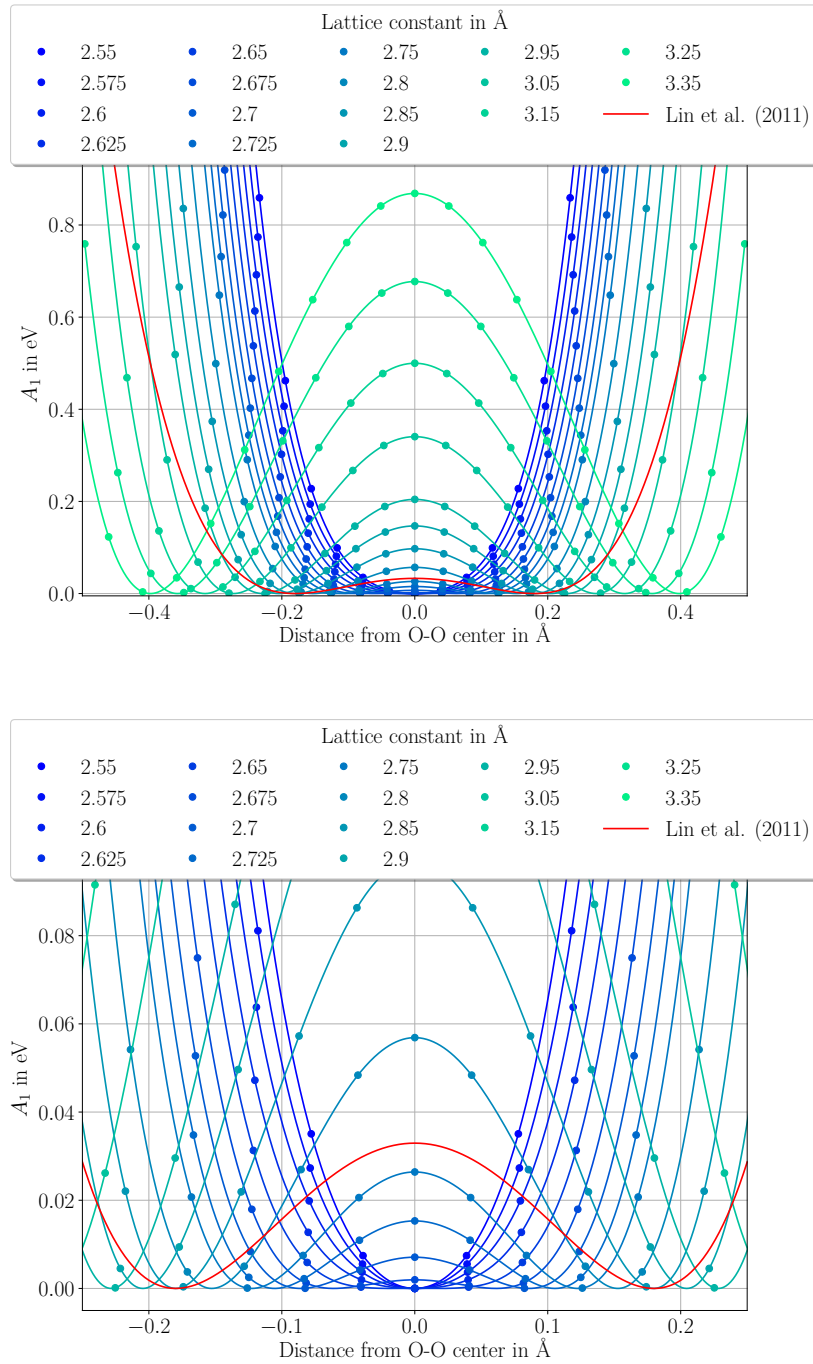


FIG. 2. Potentials obtained by collectively sampling all protons along dOOD. **(top)** The barrier in the double-well potential decreases with decreasing lattice constant (increasing compression) until the double-well character is lost at a lattice constant  $l \lesssim 2.675$  Å. **(bottom)** Rescaling the y-axis, we can see that the potentials continuously merge to a single-well with compression. During this process minima in the potential move closer to the center. The potential of Lin *et al.* [2] at 2.84 Å (red) is shown for comparison

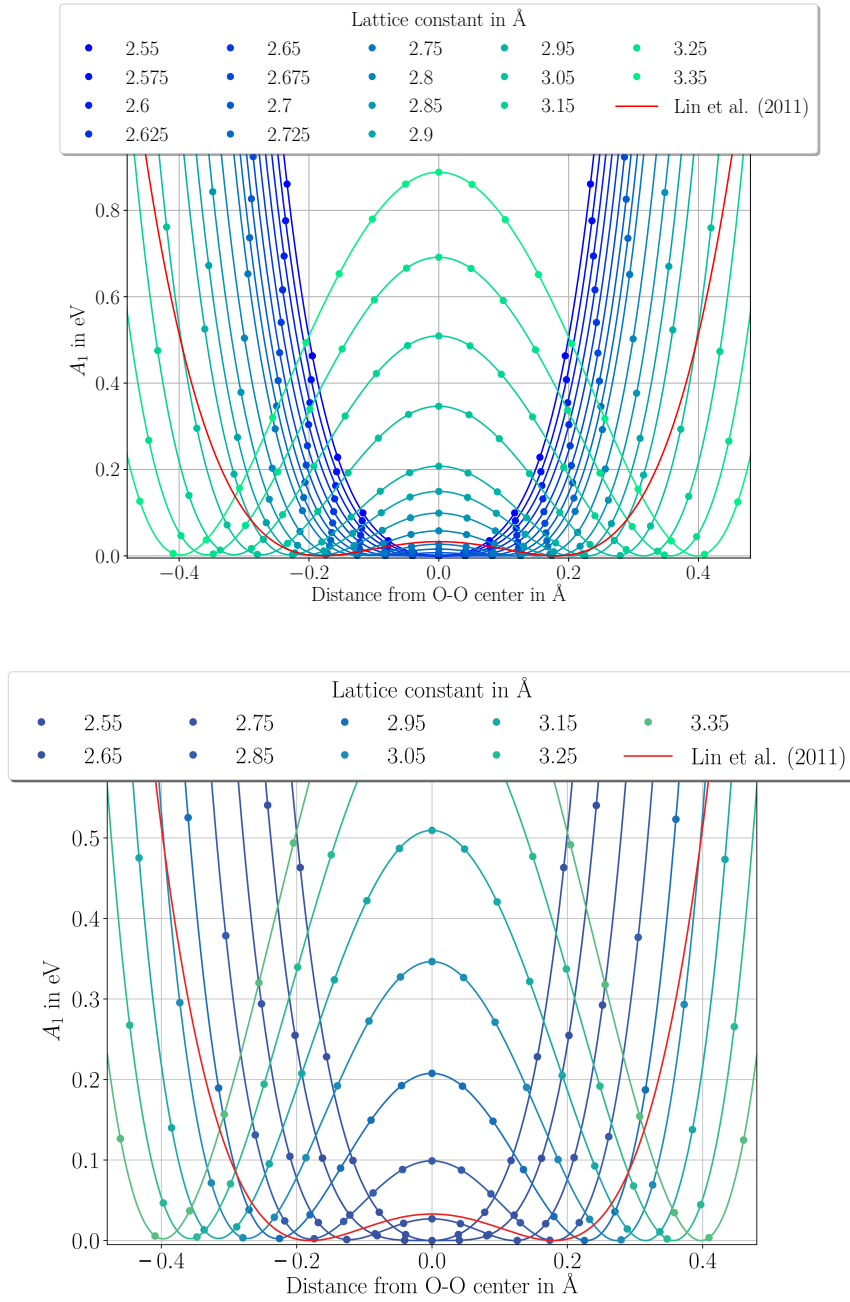


FIG. 3. Potentials of proton positions along dOOd, when six protons are shifted simultaneously in a hexagonal configuration as suggested by Lin *et al.* [2] and Drechsel-Grau and Marx [3]. **(top)** All sampled lattice constants and **(bottom)** a reduced set of results (zooming in on a smaller energy scale). With compression, the distance between the minima and the height of the barrier decreases until for lattice constant of  $l \lesssim 2.675$  Å the double-well character is lost. The form of the potentials is nearly equal to Figure 2, with a slight asymmetry due to the non-central position of the hexagon in the simulation cell (reflecting the effects of the periodic boundary conditions). The potential of Lin *et al.* [2] at 2.84 Å is shown in red.

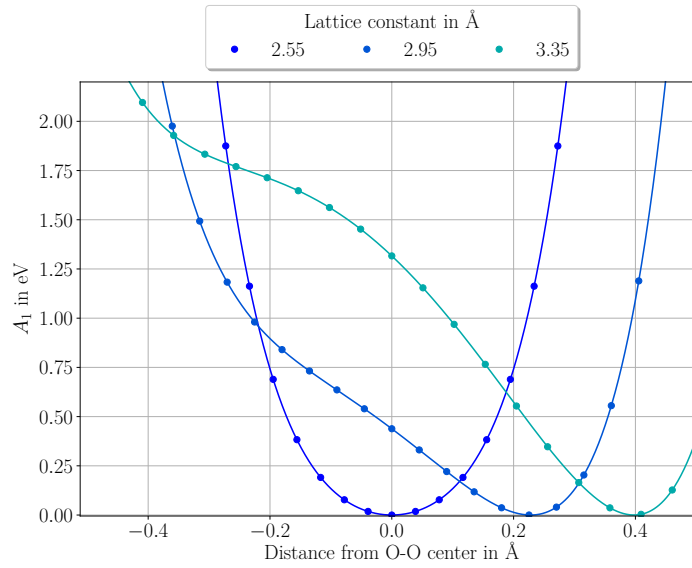


FIG. 4. Potentials obtained by sampling a single proton along dOOd in an ice-rule conforming configuration. The potential is strongly asymmetric with the minima closely matching one of the minima for the cases of the collectively all and hexagonal configurations. With compression, the asymmetry decreases and the potential approximates the cases for the collectively all/hexagonal configurations, with a slightly more pronounced localization.

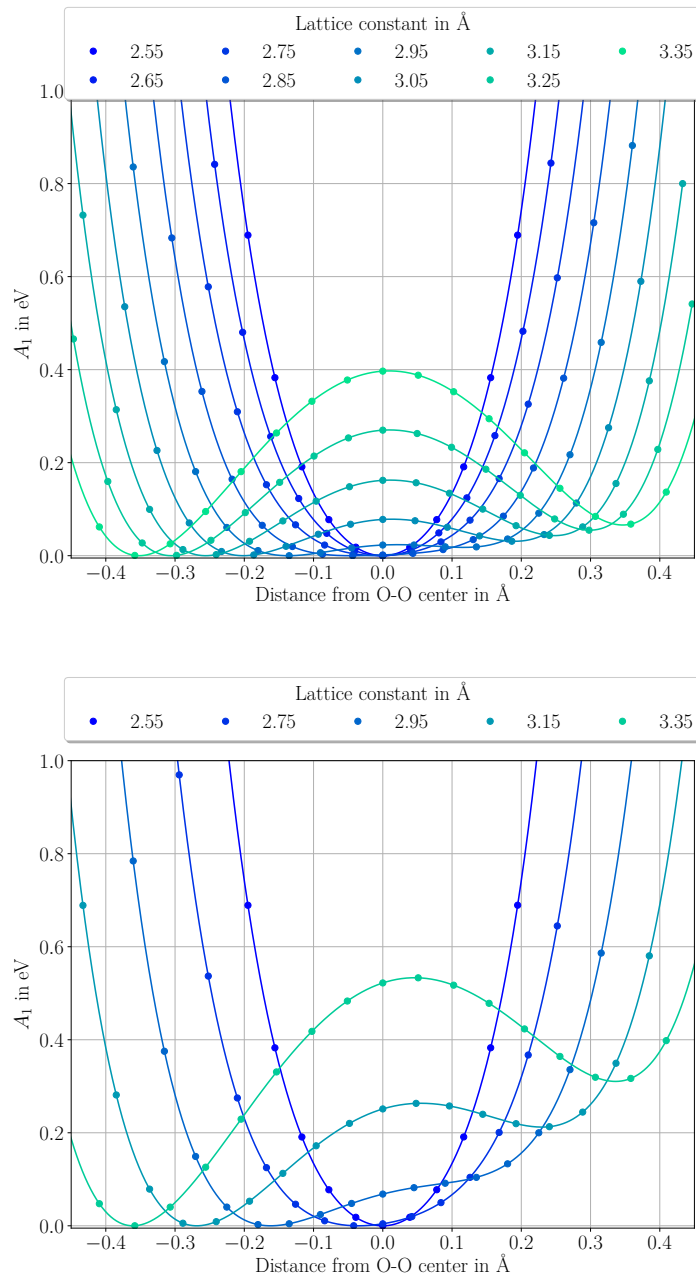


FIG. 5. Potential of proton positions along dOod, when the ice-rules are violated with **(top)** cis- $\text{H}_3\text{O}^+$  and **(bottom)** trans- $\text{H}_3\text{O}^+$  configurations (charge defects conjugated). The potentials show a significantly lower barrier than the collectively all or hexagonal configurations, and lose the double-well character at  $l \lesssim 2.85$  Å. The trans- $\text{H}_3\text{O}^+$  configuration shows a more asymmetric potential due to the position of the sampling point in the simulation cell.

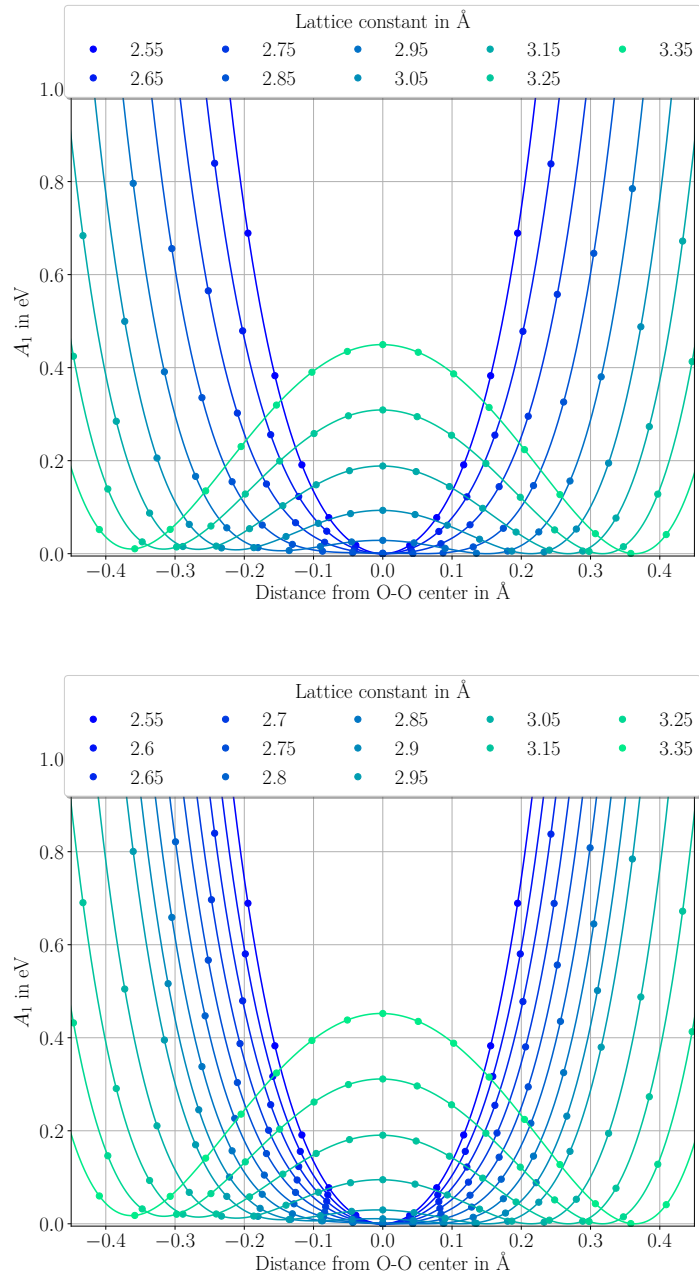


FIG. 6. Potential of proton positions along dOod, when the ice-rules are violated with (**top**) cis- $\text{OH}^-$  and (**bottom**) trans- $\text{OH}^-$  configuration (charge defects conjugated). The potentials lose the double-well character in agreement with the  $\text{H}_3\text{O}^+$  configurations at a lattice constant of  $l \lesssim 2.85$  Å.

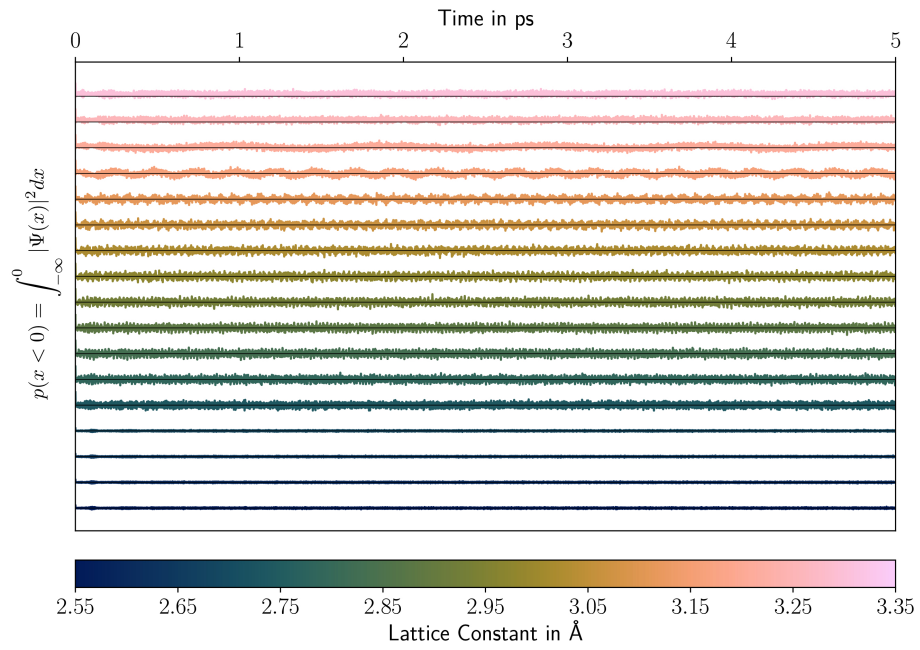


FIG. 7. Probability of finding the proton in the left half of the potential,  $p(x < 0)$ , as a function of time for the hexagonal configuration. The value of 0.5 is indicated by black lines.



## 5.2 Ice-VII - ice-X transition studied by time-resolved XRD in a dDAC

The following section contains the manuscript

*„Bulk modulus of H<sub>2</sub>O across the ice-VII – ice-X transition measured by time-resolved X-ray diffraction in dynamic Diamond Anvil Cell experiments“*

Alba S.J. Méndez, Florian Trybel, Rachel Husband, Gerd Steinle-Neumann,  
Hanns-Peter Liermann and Hauke Marquardt

Status: Submitted to *Physical Review B*

(25 June 2020)

and the related supplementary material.

## **Bulk modulus of H<sub>2</sub>O across the ice-VII – ice-X transition measured by time-resolved X-ray diffraction in dynamic Diamond Anvil Cell experiments**

A. S. J. Méndez\*<sup>1,2</sup>, F. Trybel<sup>2</sup>, R. J. Husband<sup>1</sup>, G. Steinle-Neumann<sup>2</sup>, H.-P. Liermann<sup>1</sup> and H. Marquardt<sup>3</sup>

<sup>1</sup>Deutsches Elektronen-Synchrotron (DESY), 22607 Hamburg, Germany; <sup>2</sup>Bayerisches Geoinstitut, Universität Bayreuth, 95440 Bayreuth, Germany; <sup>3</sup>Department of Earth Sciences, University of Oxford, OX1 3AN Oxford, UK.

\* Corresponding author: Alba San José Méndez (alba.mendez@desy.de)

We have studied the H<sub>2</sub>O ice-VII – ice-X phase transition by performing quasi-continuous synchrotron time-resolved X-ray diffraction measurements in a dynamic Diamond Anvil Cell experiments, reaching pressures of 180 GPa at room temperature. The dense pressure-coverage of our data allows us to directly derive the bulk modulus for H<sub>2</sub>O at high pressure. Our data document three major changes in the compression behavior in the ranges of 35-45, 50-55 and 90-110 GPa, likely corresponding to the formation of pre-transition dynamically disordered ice-VII and ice-X, and static ice-X, respectively. Our results confirm that ice-X has a very high bulk modulus.

### 1. INTRODUCTION

H<sub>2</sub>O ice is present in a large variety of planetary bodies, including the ice giants, Uranus and Neptune, mini-Neptune exoplanets<sup>1,2</sup> and icy satellites,<sup>3,4</sup> having a fundamental impact on the heat and chemical exchange in their interiors.<sup>5-8</sup> H<sub>2</sub>O ice might also be present in Earth's deep mantle, as well as other terrestrial planets, where it can form through mineral dehydration reactions occurring at relatively cold regions of the mantle.<sup>9-11</sup> The polymorphs ice-VII and ice-X are the stable forms of H<sub>2</sub>O ice that exist at pressures ( $P$ ) larger than 2 GPa, and their physical properties play a pivotal role in the structure and evolution of H<sub>2</sub>O-rich planetary bodies.

Ice-VII is a solid characterized by a body centered cubic (*bcc*) arrangement of oxygens, with H<sub>2</sub>O molecules linked via hydrogen bonds (O-H $\cdots$ O) such that the ice-rules are satisfied.<sup>12</sup> The high- $P$  phase ice-X is based on the same *bcc* oxygen lattice, but hydrogen atoms are located symmetrically between two oxygen atoms (O-H-O). It has been predicted that the ice-VII – ice-X transition proceeds through a proton order-disorder transition through which H<sub>2</sub>O molecules dissociate, triggered by changes in the energy potential for the O-H $\cdots$ O bond with  $P$ , leading to the formation of pre-transitional phases prior to complete bond symmetrization in ice-X.<sup>13-16</sup> At low  $P$ , the energy potential determining the position of the protons has been predicted to be of double-well character with a high energy barrier and a localized proton position coinciding with one of the two minima.<sup>17</sup> Computational studies<sup>13-17</sup> find three main changes in the energy potential of the H-bond across the ice-VII – ice-X transition:

(i) A lowering of the energy barrier with  $P$  triggers proton tunneling between the two minima, forming the translationally or dynamically disordered ice-VII (ice-VII'). (ii) As the potential barrier approaches zero with  $P$ , the proton distribution shifts to the center, forming the dynamically disordered ice-X (ice-X'). (iii) Symmetrization is complete when the energy potential adopts an effective narrow single-well form, localized at the mid-point between two oxygens (O-H-O), forming static ice-X.

Numerous experimental studies employing different techniques, i.e., X-ray<sup>18,19</sup> (XRD) and neutron diffraction,<sup>20</sup> Raman<sup>21</sup> and IR spectroscopy<sup>22-25</sup> as well as refractive index measurements,<sup>26</sup> reported anomalies between 40 and 75 GPa, possibly associated with the formation of the dynamically disordered phases. Diffraction<sup>18,20,27</sup> and IR-measurements<sup>18,20,23,25,27</sup> have reported O-H-O bond symmetrization in the  $P$ -range of 110-140 GPa, while Raman<sup>28</sup> and optical measurements<sup>26</sup> suggest an onset at  $P \approx 90$  GPa. However, these experimental techniques do not probe the proton dynamics directly, and the formation of the pre-transitional states cannot be unambiguously detected. Recently, Meier et al.<sup>29</sup> reported first direct observations of proton nuclei mobility for  $P=8-90$  GPa by a line-shape analysis of Nuclear Magnetic Resonance experiments.

Here we perform dynamic compression experiments in combination with time-resolved XRD in order to explore the compressive behavior of H<sub>2</sub>O across the ice-VII – ice-X transition up to 180 GPa using a dynamic Diamond Anvil Cell (dDAC) driven by a piezoelectric actuator.<sup>30,31</sup>

## 2. METHODS

### 2.1 Experimental setup

Three symmetric DACs are equipped with 150, 100 and 80  $\mu\text{m}$  diameter culet anvils (dDAC-1, dDAC-2 and dDAC-3), with two different gasket configurations (Table 1): (i) In dDAC-2 and dDAC-3, regular Re gaskets are pre-indented to a thickness of 30  $\mu\text{m}$  and holes of 50 and 40  $\mu\text{m}$  diameters are drilled, respectively. (ii) In dDAC-1, an amorphous gasket is employed in order to avoid the emergence of strong diffraction peaks from the Re gasket that may overwhelm the diffraction patterns of H<sub>2</sub>O with smaller scattering factors. A disk of an amorphous boron alloy (Fe<sub>0.79</sub>Si<sub>0.06</sub>B<sub>0.15</sub>) with a thickness of 30  $\mu\text{m}$  and a 50  $\mu\text{m}$  diameter hole is inserted in a Re gasket, pre-indented to the same thickness, following the procedure described in Méndez *et al.*<sup>32</sup>.

Milli-Q H<sub>2</sub>O is loaded along with Au powder (99.99% pure from Sigma Aldrich) as a  $P$ -marker and a ruby chip to monitor  $P$  in the sample during pre-compression. DACs are inserted in a “cap housing” coupled to a high-voltage piezoelectric actuator (PEA) as described in Jenei *et al.*<sup>31</sup> DAC and PEA are coupled by tightening the end cap at the back of the housing until a  $P$ -increase of 1-2 GPa is observed. The PEA is connected to an amplifier (Piezosystem Jena GmbH), remotely controlled via a waveform generator (Agilent 33522B). When voltage is applied, the PEA in contact with the DAC expands, pushing directly onto the piston and compressing the sample. Trapezoidal voltage-time waveforms are created by the Agilent Benchlink waveform builder software by Keysight and sent to the

PEA. We apply voltage-time waveforms with nominal compression rates ranging from 0.4-0.6 GPa/s – with dDAC-3 having the highest compression rate – that permits for sufficiently long exposure times while still achieving an excellent resolution in  $P$ -sampling (Table 1).

**Table 1.** Summary of experimental run conditions

Run #	Culet size ( $\mu\text{m}$ )	Gasket type	Sample-detector distance (mm)	Maximum pressure (GPa)	Experiment total time (s)	Nominal compression rate (GPa/s)	Exposure time L1/L2 (ms)	Images collected during compression
dDAC-1	150	Amorphous	418.42	90	300	0.5	500/100	428/2140
dDAC-2	100	Re	166.31	160	850	0.4	1000*	620
dDAC-3	80	Re	404.89	180	868	0.6	2000/2000	335

\*Only one detector was aligned with the sample in order to collect full diffraction rings.

## 2.2 X-ray diffraction

Monochromatic synchrotron X-rays with a fixed wavelength (0.4828 Å) are used for time-resolved diffraction experiments at the Extreme Conditions Beamline P02.2 at PETRA III, Hamburg, Germany.<sup>33</sup> A compound refractive lens-focused X-ray beam (2  $\mu\text{m}$  (h) x 8  $\mu\text{m}$  (v) FWHM) is aligned with the center of the sample chamber. Two GaAs 2.3 MPix LAMBDA detectors (L1 and L2) that allow for a repetition rate of up to 2 kHz are employed to perform fast collection of XRD images.<sup>34,35</sup>

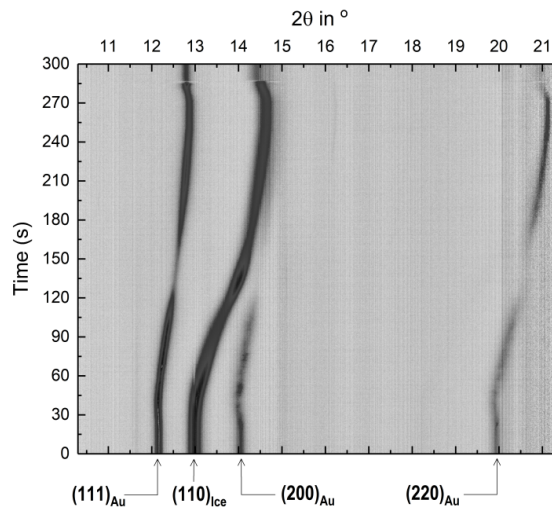


**Figure 1.** Typical contour plot showing the time-evolution of diffraction patterns (peaks) collected with L2 for dDAC-1 in time- $2\theta$  space; In our experiments, the (110) diffraction line of ice-VII,  $(110)_{\text{IceVII}}$ , is the most intense and can be traced over the full pressure-range of the individual experiments.

For dDAC-2, one detector is aligned with the sample center and placed at a short sample-to-detector distance (Table 1), ensuring the collection of full diffraction rings. For dDAC-1 and dDAC-3, two detectors (L1 and L2) are symmetrically-offset from the direct beam, capturing sections of the Debye–Scherrer diffraction rings. Tilting of the detector(s) and the sample-detector distance are calibrated using a Cr<sub>2</sub>O<sub>3</sub> standard (NIST 674b). In-house data analysis software is used for quick visualization of the collected data (Fig. 1) and a customized Python code is employed for detailed automatic processing of the integrated XRD patterns.

### 2.3 Diffraction pattern fitting

The detector images are radially integrated using the Dioptas software<sup>36</sup> to obtain 1D diffraction patterns as a function of the  $2\theta$ -angle (Fig. 2). During integration, the dead areas of the detectors are masked to improve the signal/noise ratio. Additionally, the most intense areas of the (10-11) diffraction ring of Re are masked in dDAC-2 in order to minimize the convolution with the (110) diffraction ring of H<sub>2</sub>O ice (Fig. 3).

A python routine is developed to deal with the large number of diffraction patterns (Table 1) and to automate peak fitting and tracking. Before integrated patterns are processed by the routine, we average over three points in  $2\theta$ -space and apply an infinite impulse response (IIR) filter forwards and backwards with zero phase shift to further improve the signal/noise ratio and the reliability as well as the speed of the fitting routine (Fig. 2). In order to analyze the recorded diffraction data, the peaks in the window  $2\theta=11.0^\circ$ - $20.0^\circ$  are fitted, assigned to a crystal structure and positions are tracked over the entire compression range in all diffraction patterns. In a first step, the positions of the expected peaks (indices identified via peak comparison with Dioptas) were calculated from the space group and a given initial compression using a routine from the *pymatgen* (Python Materials Genomics) library.<sup>37</sup> The calculated peak positions (*CPP*) are used as the initial positions for a model consisting of a Gaussian for each peak and a linear background correction. The model is optimized with a non-linear least-squares fit to obtain optimal peak positions (*OPP*) employing the *LMFIT* package.<sup>38</sup> The *OPP* of the individual Gaussians is subsequently compared with the prediction (*CPP*). If the *OPP* is at larger (smaller)  $2\theta$ -angle than *CPP*, compression is increased (decreased) until  $|OPP-CPP| < \epsilon$  is reached ( $\epsilon \leq 10^{-3}$ ). The optimization of the compression is performed with an adaptive step width to improve accuracy and runtime.

As the *P*-standard and the sample differ in compressional behavior, the peak positions are separately optimized: *P* is calculated using the optimized position of the (111) diffraction line of Au combined with the equation-of-state of Fei *et al.*<sup>39</sup>. Volume of H<sub>2</sub>O ice is determined from the (110) diffraction line. The (200) peak of the *P*-standard and a possible peak from the gasket (dDAC-2 and dDAC-3) are included to improve the model, but not considered in the optimization.

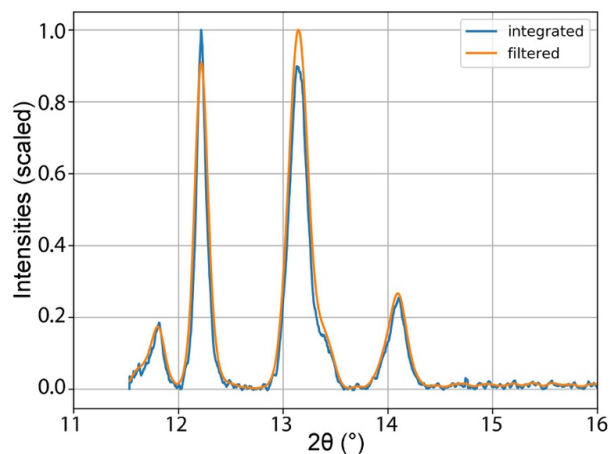


**Figure 2.** Exemplary integrated diffraction pattern for the dDAC-2 at 26 GPa. Blue shows the original pattern after integration of the detector image with Dioplas. Orange is the pattern after application of an IIR filter with zero phase shift.

Diffraction patterns are individually loaded with user input on the first compression estimate. Although the program can handle each spectrum individually, it is significantly more efficient to guess a starting compression from the previous  $P$ -step. This especially helps to resolve overlapping peaks, where a good initial guess is crucial. Such an interaction between  $(110)_{\text{Ice-II}}$  and  $(10-11)_{\text{Re}}$  is shown in Fig. 3. At low  $P$ ,  $(110)_{\text{Ice-II}}$  appears at a smaller  $2\theta$ -value than  $(10-11)_{\text{Re}}$ ; during compression, the peaks start to overlap at  $P > 20$  GPa and reverse order with respect to  $2\theta$  at  $P > 40$  GPa. The routine can resolve the individual peaks while they are partly overlapping by estimating a linear compression rate. However, if the peaks are completely overlapping, a reliable fit is not possible, and for dDAC-3 a small  $P$ -range (41-49 GPa) is therefore not processed. Nevertheless, we obtain, especially for dDAC-2 with a full diffraction ring, dense  $P$ - $V$  data with only small data scatter introduced by the fitting routine due to peak asymmetry and overlap. The error in volume ( $V$ ) is calculated from the minimal separable peak distance in the routine ( $0.05^\circ$  in  $2\theta$ ) and translated to  $V$  by calculating the difference between  $CPP$  shifted by this amount.

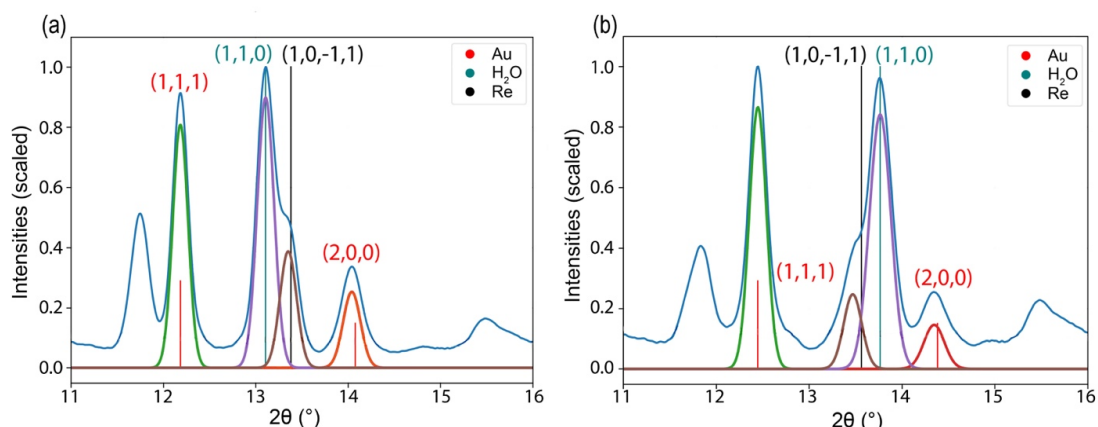


**Figure 3.** Diffraction patterns collected from dDAC-2 after application of the IRR filter (blue) at (a) 24 GPa and (b) 45 GPa with assigned indices and the theoretical peak positions (*CPP*) shown as vertical lines. The solid curves represent the Gaussian model peaks. A detector artifact appears in the patterns as a bump at 15.5° in  $2\theta$ .

#### 2.4 Bulk modulus calculation

The isothermal bulk modulus ( $K_T$ ) can be directly calculated from our dense  $P$ - $V$  dataset via  $K_T = -V \partial P / \partial V$ , with the advantage that no assumption has to be made with respect to the analytical form of an equation-of-state. Although the high resolution enables a numerical calculation, small artificial jumps in the  $P$ - $V$  data introduce strong features in the bulk modulus (Supp. Mat. Fig. 1). Therefore, we apply spline interpolation with smoothing<sup>40,41</sup> before calculating the bulk modulus via a central difference scheme and use only every 5th data point for dDAC-2 and dDAC-3 and every 20th point for dDAC-1 in order to reduce noise, while still preserving an excellent  $P$ -resolution, i.e., 1 GPa for dDAC-1 and 3 GPa for dDAC-2 and dDAC-3. The smoothing factors are chosen such that smooth variations of  $K_T$  with  $P$  are obtained, while simultaneously keeping the difference between data points and the spline  $<1\%$  over the complete compression-range for all experiments (Fig. 4b). The least smoothing is required for dDAC-2, reflecting that – by experimental design – this is expected to be the highest-quality experimental series. Therefore, dDAC-2 is used as a reference for the following discussion.

The error in  $K_T$  is propagated from the error in  $V$  with a central difference scheme. As the error in the  $2\theta$ -angle of the  $P$ -marker is at least one order of magnitude smaller than for ice (no asymmetry or overlap),  $P$  is assumed to be error-free.

### 3. RESULTS AND DISCUSSION

#### 3.1 Volume compression curve of H<sub>2</sub>O ice

Figure 4 shows the unit cell volume of H<sub>2</sub>O ice as a function of  $P$  from our experiments in comparison with previous XRD measurements<sup>18,19</sup> and equations-of-state.<sup>42,43</sup> Differences between the unit cell  $V$  measured in our three experimental runs fall within experimental uncertainties (Fig. 4a), suggesting that neither the choice of the gasket material (dDAC-1) nor the higher compression rate (dDAC-3) influence the compression behavior of H<sub>2</sub>O. The observed slight deviations between our experimental results, as well as to previously published measurements,<sup>18,19</sup> may stem from different factors including inhomogeneous strain in the sample in the absence of a  $P$ -transmitting medium or peak overlap between ice and the  $P$ -standard and/or gasket. Overall, our  $P$ - $V$  data are in good agreement with previous experimental results from Sugimura *et al.*<sup>18</sup> (Fig. 4c).

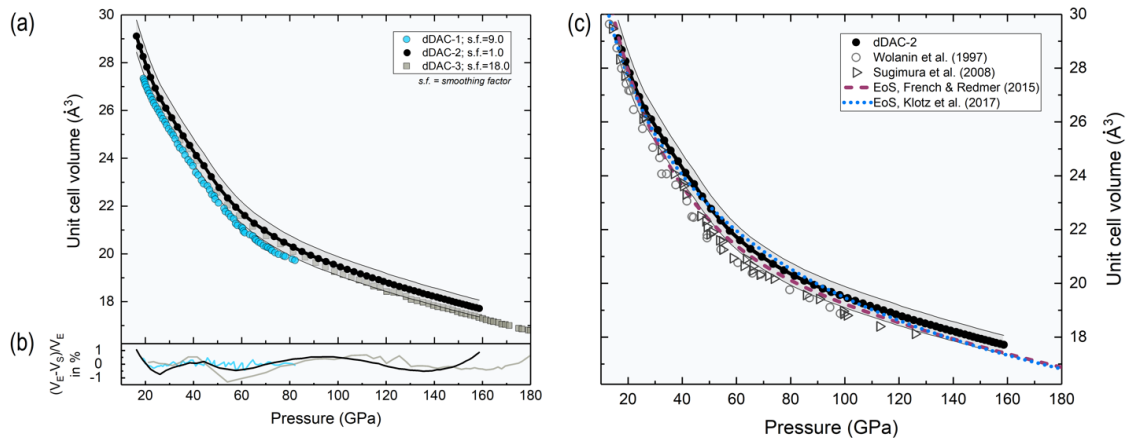


**Figure 4.** (a) Volume-pressure points for H<sub>2</sub>O ice as derived from dDAC-1 (blue solid circles), dDAC-2 (black solid circles) and dDAC-3 data (grey solid squares). Data are splined with smoothing factors of 9.0 (dDAC-1), 1.0 (dDAC-2) and 18.0 (dDAC-3), with the interpolation shown for dDAC-2 (black curve) and an error band using the resolution limit of the fitting routine (shaded region). (b) Difference between the data points and the spline is <1% over the complete compression range for all experiments. (c) Previous XRD measurements in static DAC experiments by Wolanin *et al.*<sup>19</sup> (pink open circles) and Sugimura *et al.*<sup>18</sup> (white right-pointing triangles) are plotted in comparison to the volume-pressure data from dDAC-2. The maroon and blue dotted curves represent the equations-of-state by French & Redmer<sup>42</sup> and Klotz *et al.*<sup>43</sup>, respectively, the latter extrapolated beyond the pressure-range of the experiments (14 GPa).

Our data generally agree with equations-of-state based on both experimental data<sup>43</sup> and computational results,<sup>42</sup> even though some small but systematic deviations in  $P$ -trends exist in the  $P$ -range 50-100 GPa (Fig. 4c) which coincides with formation of the disordered ice phase(s), likely triggered by nuclear

quantum effects occurring in the range  $50 \lesssim P \lesssim 70$  GPa.<sup>13,14</sup> French & Redmer<sup>42</sup> compute an analytical thermodynamic potential from ab-initio calculations based on classical proton trajectories. Although their calculations were supplemented with a quantum correction, they did not include tunnelling effects, which affect the protonic motion and explain the deviation to our results. The equation of state by Klotz *et al.*<sup>43</sup> is based on the extrapolation of neutron diffraction data measured up to 14 GPa, which is a too low pressure for observing significant proton tunnelling effects.

### 3.2 Bulk modulus of H<sub>2</sub>O ice at high pressures

The evolution of  $K_T$  with  $P$  based on the dDAC-2 experiment is shown in Fig. 5 (see Supp. Mat. Fig. 2 for dDAC-1, dDAC-3). For  $P \lesssim 35$  GPa, our  $K_T$ -measurements are in good agreement with most of the previous results,<sup>44-46</sup> with the exception of Asahara *et al.*<sup>47</sup>.

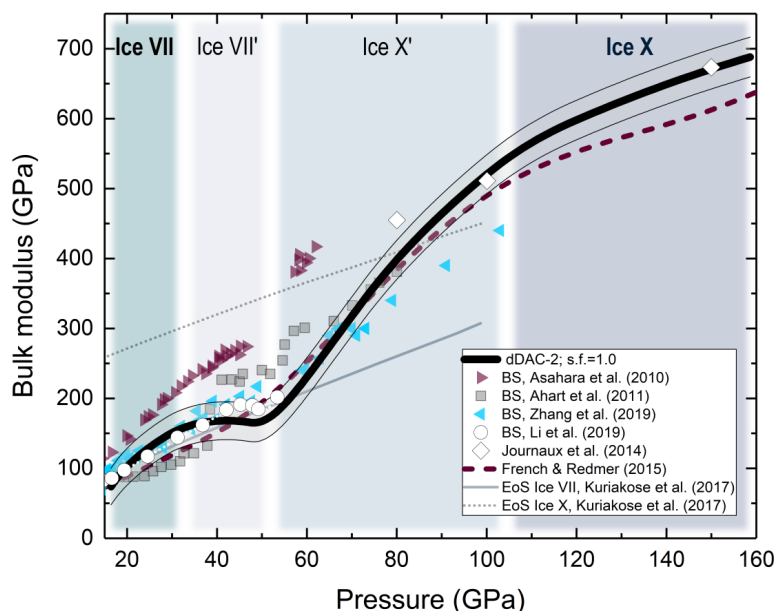


**Figure 5.** Bulk modulus of H<sub>2</sub>O ice as a function of pressure calculated from the smoothed spline interpolation of the volume-pressure data from dDAC-2 in comparison to previous studies. Right-pointing triangles, solid squares, left-pointing triangles and solid circles represent Brillouin inelastic scattering (BS) data (Ref. 44-47). The solid and dotted thin grey lines show equations-of-state for ice-VII and ice-X, respectively (Ref. 48). Open diamonds represent computational predictions of the bulk modulus of ice-X (Ref. 49). The dashed maroon line refers to computational results (Ref. 42). Background colours represent the approximate pressure-range for the stability of ice-VII, ice-VII', ice-X' and ice-X based on the changes in bulk modulus observed in our work.

At higher  $P$ , however, previous results for  $K_T$  increasingly diverge and generally disagree with our data. Three main changes in the slope of  $K_T$  are clearly captured by our experiments:

- (i) A softening at  $P=35-45$  GPa indicates the transition towards a more compressible state (Fig. 4), supporting previous findings.<sup>18</sup> We associate this change with the formation of disordered ice-VII', in agreement with Brillouin spectroscopy measurements by Li *et al.*<sup>45</sup> who suggested that the softening observed in their data for  $P=42-53$  GPa is caused by the presence of a pre-transitional state of ice-VII. This softening, however, has not been observed in other Brillouin studies.<sup>44,46,47</sup> Zhang *et al.*<sup>46</sup> recorded a nearly constant  $P$ -dependence of the bulk modulus from 20 to 100 GPa, the results from Ahart *et al.*<sup>44</sup> show an increase of the bulk modulus at 40 GPa. Some of the disagreement between published Brillouin spectroscopy results are likely related to challenges in measuring compressional wave velocities at  $40 \lesssim P \lesssim 60$  GPa due to overlap of the sample peaks with signals from the diamond anvils. Results reported by Asahara *et al.*<sup>47</sup> generally show a significantly larger modulus compared to other work, with a steep hardening at 50 GPa. A possible reason for this is the marked elastic anisotropy of ice-VII and the possibility that velocities along certain directions were favored by crystallographic preferred orientation and/or selective elasto-optic coupling between the probing laser and specific phonon propagation direction.<sup>50</sup>
- (ii) A steep increase in  $K_T$  starting at  $P \approx 50-55$  GPa marks the formation of a less compressible phase, in agreement with the onset of hydrogen symmetrization predicted by computations at  $P \approx 50$  GPa,<sup>13</sup> and may also be associated to anomalies in the infrared spectra of H<sub>2</sub>O ice reported for  $P=55-62$  GPa.<sup>23,51,52</sup> We attribute this feature to the formation of ice-X'.<sup>18</sup>
- (iii) A distinct change in  $P$ -dependence of  $K_T$  at  $P=90-110$  GPa, which is in excellent agreement with computational predictions,<sup>42,49</sup> but has not been documented by previous experiments on the elastic properties of ice-VII.<sup>18,24,26-28</sup> We attribute this change to the formation of static ice-X.

The observed  $P$ -evolution of  $K_T$  across the ice-VII – ice-X transition in our experiments can be correlated with the variations in proton nuclei mobility observed by Meier *et al.*<sup>29</sup> for the O-H $\cdots$ O bond, and explained by the predicted evolution of the energy barrier of the double-well potential.<sup>17,53</sup> Meier *et al.*<sup>29</sup> documented a significant increase in tunnelling probability for  $P=20-50$  GPa, i.e., in the  $P$ -range where the formation of ice-VII' is expected. Our observation of a softening of  $K_T$  for ice-VII observed for  $P=35-40$  GPa may be explained by a decrease in the ‘‘proton pressure’’ caused by higher mobility.<sup>18,53</sup> The steep increase in  $K_T$  we observe for  $P > 50$  GPa (Fig. 5) may reflect the proton centering process, and the formation of ice-X'. Full proton localization might cause a change of the  $P$ -derivative in our  $K_T$ -data for  $P=90-110$  GPa.

## 4. CONCLUSIONS

We have collected quasi-continuous X-ray diffraction data across the ice-VII – ice-X transition and up to  $P=180$  GPa in dynamically driven diamond-anvil-cell experiments. We derive the bulk modulus of H<sub>2</sub>O ice directly from our P-V data. We find three main changes in the pressure-dependence at 35-45, 50-55 and 90-110 GPa and associate them with the formation of ice-VII', ice-X' and ice-X, respectively. These transitions are not sharp; certainly not of first order (no volume collapse), unlikely of second order (no discontinuous changes in bulk modulus). This association suggests that the compressive behavior of H<sub>2</sub>O at high pressure is sensitive to proton ordering. Our results further confirm computational predictions that the bulk modulus of ice-X is distinctly higher than that of ice-VII.

## Acknowledgements

This research was supported through the DFG Research Unit FOR 2440 (grants MA4534/5-1 and STE1105/13). We acknowledge DESY (Hamburg, Germany), a member of the Helmholtz Association HG, for providing the experimental facility PETRA III and beamline P02.2. We acknowledge B. Winkler and the BMBF project 05K13RF1 for the purchase of the laser cutting machine for preparing gaskets. We thank Martin French for sharing water high-pressure data. We thank Tiziana Boffa Balaran, Niccolò Satta and Thomas Meier for helpful discussions.

## References

- <sup>1</sup> J.J. Lissauer *et al.*, *Nature* **470**, 53 (2011).
- <sup>2</sup> R. Redmer, T.R. Mattsson, N. Nettelmann, and M. French, *Icarus* **211**, 798 (2011).
- <sup>3</sup> R. Jaumann, R.N. Clark, F. Nimmo, A.R. Hendrix, B.J. Buratti, T. Denk, J.M. Moore, P.M. Schenk, S.J. Ostro, and R. Srama, in *Saturn from Cassini-Huygens*, edited by M.K. Dougherty, L.W. Esposito, and S.M. Krimigis (Springer Netherlands, Dordrecht, 2009), pp. 637–681.
- <sup>4</sup> S.A. Kattenhorn and L.M. Prockter, *Nat. Geosci.* **7**, 762 (2014).
- <sup>5</sup> B. Journaux, I. Daniel, S. Petitgirard, H. Cardon, J.-P. Perrillat, R. Caracas, and M. Mezouar, *Earth Planet. Sc. Lett.* **463**, 36 (2017).
- <sup>6</sup> L. Noack, D. Höning, A. Rivoldini, C. Heistracher, N. Zimov, B. Journaux, H. Lammer, T. Van Hoolst, and J.H. Bredehöft, *Icarus* **277**, 215 (2016).
- <sup>7</sup> C. Sotin, O. Grasset, and A. Mocquet, *Icarus* **191**, 337 (2007).
- <sup>8</sup> A.D. Fortes and M. Choukroun, *Space. Sci. Rev.* **153**, 185 (2010).
- <sup>9</sup> J.-F. Lin, V. V. Struzhkin, S. D. Jacobsen, M. Y. Hu, P. Chow, J. Kung, H. Liu, H.-k. Mao and R. J. Hemley, *Geophys. Res. Lett.* **32**, L11306 (2005).
- <sup>10</sup> B. Schwager and R. Boehler, *High Pressure Res.* **28**, 431 (2008).
- <sup>11</sup> O. Tschauer, S. Huang, E. Greenberg, V.B. Prakapenka, C. Ma, G.R. Rossman, A.H. Shen, D. Zhang, M. Newville, A. Lanzirrotti, and K. Tait, *Science* **359**, 1136 (2018).
- <sup>12</sup> J.D. Bernal and R.H. Fowler, *J. Chem. Phys.* **1**, 515 (1933).
- <sup>13</sup> W.B. Holzapfel, *J. Chem. Phys.* **56**, 712 (1972).
- <sup>14</sup> M. Benoit, D. Marx, and M. Parrinello, *Nature* **392**, 258 (1998).
- <sup>15</sup> M. Benoit, A.H. Romero, and D. Marx, *Phys. Rev. Lett.* **89**, 145501 (2002).

- <sup>16</sup> M. Benoit and D. Marx, *ChemPhysChem* **6**, 1738 (2005).
- <sup>17</sup> L. Lin, J.A. Morrone, and R. Car, *J. Stat. Phys.* **145**, 365 (2011).
- <sup>18</sup> E. Sugimura, T. Iitaka, K. Hirose, K. Kawamura, N. Sata, and Y. Ohishi, *Phys. Rev. B* **77**, 214103 (2008).
- <sup>19</sup> E. Wolanin, Ph. Pruzan, J.C. Chervin, B. Canny, M. Gauthier, D. Häusermann, and M. Hanfland, *Phys. Rev. B* **56**, 5781 (1997).
- <sup>20</sup> M. Guthrie, R. Boehler, J.J. Molaison, B. Haberl, A.M. dos Santos, and C. Tulk, *Phys. Rev. B* **99**, 184112 (2019).
- <sup>21</sup> A.F. Goncharov, N. Goldman, L.E. Fried, J.C. Crowhurst, I. Feng W. Kuo, C.J. Mundy, and J.M. Zaug, *Phys. Rev. Lett.* **94**, 125508 (2005).
- <sup>22</sup> K. Aoki, H. Yamawaki, M. Sakashita, and H. Fujihisa, *Phys. Rev. B* **54**, 15673 (1996).
- <sup>23</sup> A.F. Goncharov, V.V. Struzhkin, M.S. Somayazulu, R.J. Hemley, and H.K. Mao, *Science* **273**, 218 (1996).
- <sup>24</sup> M. Song, H. Yamawaki, H. Fujihisa, M. Sakashita, and K. Aoki, *Phys. Rev. B* **60**, 12644 (1999).
- <sup>25</sup> M. Song, H. Yamawaki, H. Fujihisa, M. Sakashita, and K. Aoki, *Phys. Rev. B* **68**, 014106 (2003).
- <sup>26</sup> C.-S. Zha, R.J. Hemley, S.A. Gramsch, H. Mao, and W.A. Bassett, *J. Chem. Phys.* **126**, 074506 (2007).
- <sup>27</sup> P. Loubeyre, R. LeToullec, E. Wolanin, M. Hanfland, and D. Häusermann, *Nature* **397**, 503 (1999).
- <sup>28</sup> C.-S. Zha, J.S. Tse, and W.A. Bassett, *J. Chem. Phys.* **145**, 124315 (2016).
- <sup>29</sup> T. Meier, S. Petitgirard, S. Khandarkhaeva, and L. Dubrovinsky, *Nat. Commun.* **9**, 2766 (2018).
- <sup>30</sup> W.J. Evans, C.-S. Yoo, G.W. Lee, H. Cynn, M.J. Lipp, and K. Visbeck, *Rev. Sci. Instrum.* **78**, 073904 (2007).
- <sup>31</sup> Zs. Jenei *et al.*, *Rev. Sci. Instrum.* **90**, 065114 (2019).
- <sup>32</sup> A.S.J. Méndez, H. Marquardt, R.J. Husband, I. Schwark, J. Mainberger, K. Glazyrin, A. Kurnosov, C. Otzen, N. Satta, and J. Bednarcik, *Rev. Sci. Instrum.* **91**, 073906 (2020).
- <sup>33</sup> H.-P. Liermann *et al.*, *J. Synchrotron Radiat.* **22**, 908 (2015).
- <sup>34</sup> D. Pennicard *et al.*, *J. Instrum.* **13**, C01026 (2018).
- <sup>35</sup> D. Pennicard, S. Lange, S. Smoljanin, H. Hirseemann, H. Graafsma, M. Epple, M. Zuvic, M.-O. Lampert, T. Fritzsche, and M. Rothermund, *J. Phys. Conf. Ser.* **425**, 062010 (2013).
- <sup>36</sup> C. Prescher and V.B. Prakapenka, *High Pressure Res.* **35**, 223 (2015).
- <sup>37</sup> S.P. Ong, W.D. Richards, A. Jain, G. Hautier, M. Kocher, S. Cholia, D. Gunter, V.L. Chevrier, K.A. Persson, and G. Ceder, *Comput. Mater. Sci.* **68**, 314 (2013).
- <sup>38</sup> Matt Newville *et al.*, *Lmfit/Lmfit-Py 1.0.1* (Zenodo, 2020).
- <sup>39</sup> Y. Fei, A. Ricolleau, M. Frank, K. Mibe, G. Shen, and V. Prakapenka, *PNAS* **104**, 9182 (2007).
- <sup>40</sup> P. Dierckx, *J. Comput. Appl. Math.* **1**, 3 (1975).
- <sup>41</sup> P. Dierckx, *SIAM J. Numer. Anal.* **19**, 1286 (1982).
- <sup>42</sup> M. French and R. Redmer, *Phys. Rev. B* **91**, 014308 (2015).
- <sup>43</sup> S. Klotz, K. Komatsu, H. Kagi, K. Kunc, A. Sano-Furukawa, S. Machida, and T. Hattori, *Phys. Rev. B* **95**, 174111 (2017).
- <sup>44</sup> M. Ahart, M. Somayazulu, S.A. Gramsch, R. Boehler, H. Mao, and R.J. Hemley, *J. Chem. Phys.* **134**, 124517 (2011).
- <sup>45</sup> X. Li, W. Shi, X. Liu, and Z. Mao, *Amer. Miner.* **104**, 1307 (2019).
- <sup>46</sup> J.S. Zhang, M. Hao, Z. Ren, and B. Chen, *Appl. Phys. Lett.* **114**, 191903 (2019).
- <sup>47</sup> Y. Asahara, K. Hirose, Y. Ohishi, N. Hirao, and M. Murakami, *Earth Planet. Sci. Lett.* **299**, 474 (2010).
- <sup>48</sup> M. Kuriakose, S. Raetz, Q.M. Hu, S.M. Nikitin, N. Chigarev, V. Tournat, A. Bulou, A. Lomonosov, P. Djemia, V.E. Gusev, and A. Zerr, *Phys. Rev. B* **96**, 134122 (2017).
- <sup>49</sup> B. Journaux, R. Caracas, P. Carrez, K. Gouriet, P. Cordier, and I. Daniel, *Phys. Earth Planet. In.* **236**, 10 (2014).
- <sup>50</sup> S. Speziale, H. Marquardt, and T.S. Duffy, *Rev. Mineral. Geochem.* **78**, 543 (2014).
- <sup>51</sup> A.F. Goncharov, V.V. Struzhkin, H. K. Mao, and R.J. Hemley, *Phys. Rev. Lett.* **83**, 1998 (1999).
- <sup>52</sup> V.V. Struzhkin, A.F. Goncharov, R.J. Hemley, and H. K. Mao, *Phys. Rev. Lett.* **78**, 4446 (1997).
- <sup>53</sup> M. Benoit and D. Marx, *ChemPhysChem* **6**, 1738 (2005).

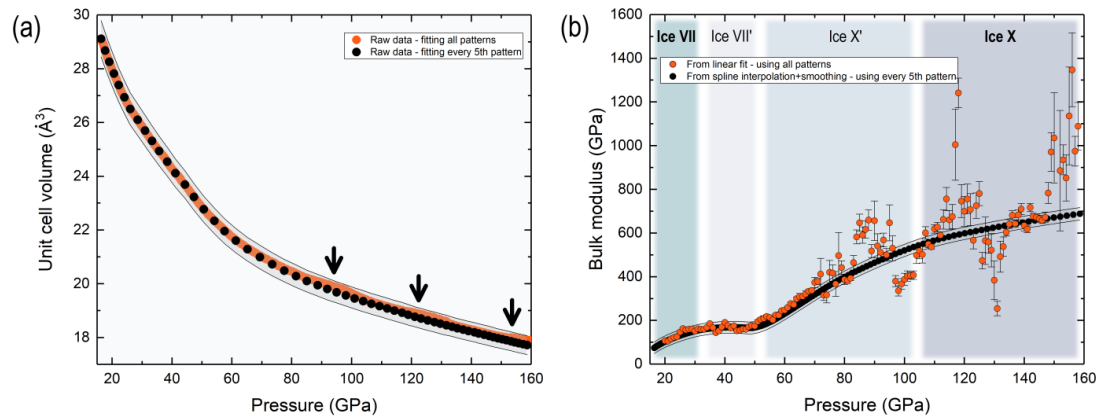
**Supplementary Material: Bulk modulus of H<sub>2</sub>O across the ice-VII – ice-X transition  
measured by time-resolved X-ray diffraction in dynamic Diamond Anvil Cell  
experiments**

A. S. J. Méndez<sup>1,2</sup>, F. Trybel<sup>2</sup>, R. J. Husband<sup>1</sup>, G. Steinle-Neumann<sup>2</sup>, H.-P. Liermann<sup>1</sup> and H. Marquardt<sup>3</sup>

<sup>1</sup>Deutsches Elektronen-Synchrotron (DESY), 22607 Hamburg, Germany; <sup>2</sup>Bayerisches Geoinstitut, Universität Bayreuth, 95440 Bayreuth, Germany; <sup>3</sup>Department of Earth Sciences, University of Oxford, OX1 3AN Oxford, UK

### 1. Data reduction

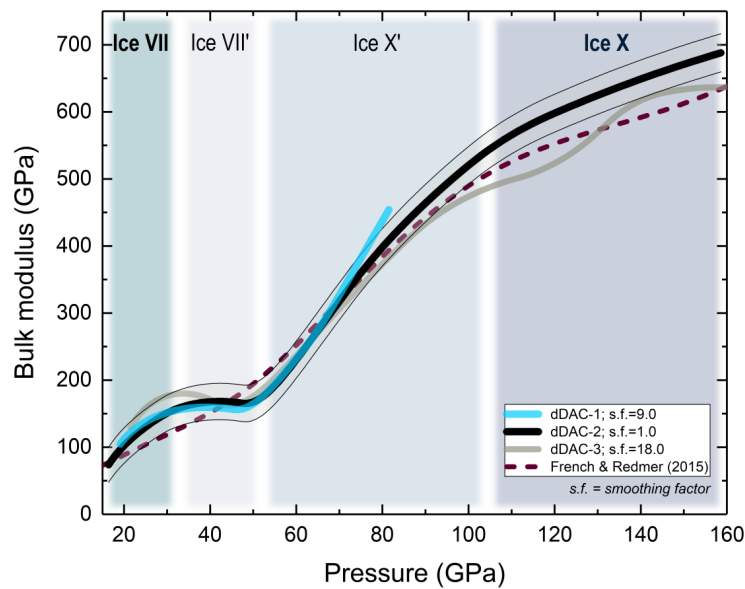
The fine pressure steps that characterize our quasi-continuous compression data are, in general, below the fitting resolution, especially for high values of the bulk modulus where the sample is highly incompressible. Under such conditions, small shifts in  $2\theta$ -space of the traced reflections cannot be resolved by the fitting program. Additionally, the presence of overlapping peaks further complicates fitting. These factors can introduce artificial jumps in the  $P$ - $V$  data that are magnified in the derivative (Supp. Mat. Fig. 1). As an alternative, we increase the  $P$ -steps by fitting every 5<sup>th</sup> diffraction pattern in dDAC-2, obtaining a  $P$ - $V$  curve with a smooth trend.



**Supp. Mat. Fig. 1.** (a) Pressure-volume curves for dDAC-2. Orange circles correspond to analysed raw data for 599 diffraction patterns, black circles represent  $P$ - $V$  data obtained after fitting every 5<sup>th</sup> pattern (error indicated by thin solid lines) as described in Section 2.3. Black arrows point to small artificial jumps in the  $P$ - $V$  data, introduced by the fitting routine due to overlap of the  $(110)_{\text{Ice VII}}$  peak with the  $(200)_{\text{Au}}$  peak at high  $P$  (Fig. 4b). (b) Bulk modulus as a function of pressure derived from dDAC-2 data, following two different procedures: (i) Calculated from the slope<sup>-1</sup> of a line fitted to  $P$ - $V$  over  $P$ -ranges of 2.5 GPa, evaluated every 1 GPa (orange circles); oscillations at 80, 120 and 150 GPa arise from the fluctuations observed in  $P$ - $V$  (black arrows in panel a). (ii) Derived from the procedure described in Section 2.4 using every 5<sup>th</sup> point (black circles).

## 2. Run Comparison

Bulk moduli  $K_T$  derived from dDAC-1, dDAC-2 and dDAC-3 are plotted against  $P$  in Supp. Mat. Fig. 2, in comparison with computational results from French & Redmer.<sup>42</sup> Overall, the  $P$ -dependence of  $K_T$  agrees between the three experiments and with the computational results. The three main changes in  $P$ -dependence of  $K_T$  – discussed for the dDAC-2 data in the main text – are also visible in dDAC-3, despite slight fluctuations noticeable above 100 GPa. These fluctuations originate from modulations in the  $P$ - $V$  curve introduced by the fitting routine. Nevertheless, the magnitude of these fluctuations falls within experimental uncertainty.



**Supp. Mat. Fig. 2.** Bulk modulus as a function of pressure as derived from dDAC-1, dDAC2 and dDAC-3 data. The dashed maroon line shows computational results (Ref. 42). Background colours represent the approximate pressure-range for the stability of ice-VII, ice VII', ice-X' and ice-X based on the changes in bulk modulus observed in our work.

### 5.3 Pressure-Induced Hydrogen-Hydrogen Interaction in FeH

The following section contains the manuscript:

*„Pressure-Induced Hydrogen-Hydrogen Interaction  
in Metallic FeH revealed by NMR“*

Thomas Meier, Florian Trybel, Saiana Khandarkhaeva, Gerd Steinle-Neumann, Stella Chariton, Timofey Fedotenko, Sylvain Petitgirard, Michael Hanfland, Konstantin Glazyrin, Natalia Dubrovinskaia and Leonid Dubrovinsky

Status: Published

Phys. Rev. X 9, 031008 – Published 17 July 2019

The Supplemental Material consisting of an animation of all ELF maps and electronic density of states calculations in combination with experimental data can be found under:

<http://link.aps.org/supplemental/10.1103/PhysRevX.9.031008>.

## Pressure-Induced Hydrogen-Hydrogen Interaction in Metallic FeH Revealed by NMR

Thomas Meier,<sup>1,\*</sup> Florian Trybel,<sup>1</sup> Saiana Khandarkhaeva,<sup>1</sup> Gerd Steinle-Neumann,<sup>1</sup> Stella Chariton,<sup>1</sup> Timofey Fedotenko,<sup>2</sup> Sylvain Petitgirard,<sup>3</sup> Michael Hanfland,<sup>4</sup> Konstantin Glazyrin,<sup>5</sup> Natalia Dubrovinskaia,<sup>2</sup> and Leonid Dubrovinsky<sup>1</sup>

<sup>1</sup>*Bayerisches Geoinstitut, University of Bayreuth, D-95447 Bayreuth, Germany*

<sup>2</sup>*Material Physics and Technology at Extreme Conditions, Laboratory of Crystallography, University of Bayreuth, D-95447 Bayreuth, Germany*

<sup>3</sup>*Institute of Geochemistry and Petrology, Department of Earth Sciences, Eidgenössische Technische Hochschule Zürich, S-8092, Switzerland*

<sup>4</sup>*European Synchrotron Radiation Facility (ESRF), F-38043 Grenoble Cedex, France*

<sup>5</sup>*Deutsches Elektronen-Synchrotron (DESY), D-22603, Hamburg, Germany*



(Received 4 March 2019; revised manuscript received 13 May 2019; published 17 July 2019)

Knowledge of the behavior of hydrogen in metal hydrides is the key for understanding their electronic properties. Here, we present an <sup>1</sup>H-NMR study of cubic FeH up to 202 GPa. We observe a distinct deviation from the ideal metallic behavior between 64 and 110 GPa that suggests pressure-induced H-H interactions. Accompanying *ab initio* calculations support this result, as they reveal the formation of an intercalating sublattice of electron density, which enhances the hydrogen contribution to the electronic density of states at the Fermi level. This study shows that pressure-induced H-H interactions can occur in metal hydrides at much lower compression and larger H-H distances than previously thought and stimulates an alternative pathway in the search for novel high-temperature superconductors.

DOI: [10.1103/PhysRevX.9.031008](https://doi.org/10.1103/PhysRevX.9.031008)

Subject Areas: Condensed Matter Physics

### I. INTRODUCTION

Hydrides and hydrogen-rich compounds continue to attract considerable attention as the search for effective and “green energy” materials intensifies [1,2]. Recent theoretical [3], computational [4–6], and experimental [7,8] results indicate that hydrides may hold the key to a deep understanding of high-temperature superconductivity and the synthesis of compounds exhibiting high critical temperatures ( $T_c$ ). Sulphur hydride (H<sub>3</sub>S), with a  $T_c$  of 200 K at a pressure ( $P$ ) of approximately 150 GPa [9], is a prominent example of such metal-hydride (MH) systems.

A systematic analysis of computational results [10,11] suggests that two properties are particularly important for achieving high- $T_c$  superconductivity in metallic MH: (i) a significant contribution of hydrogen to the electronic density of states at the Fermi energy  $N(E_F)$  and (ii) strong effects of hydrogen vibrations on the electronic structure of the material (i.e., electron-phonon coupling). Unfortunately, the lack of experimental methods that provide access to electronic states of hydrogen in MHs at such  $P$  prohibits a direct confirmation of this hypothesis.

\*thomas.meier@uni-bayreuth.de

Published by the American Physical Society under the terms of the [Creative Commons Attribution 4.0 International license](https://creativecommons.org/licenses/by/4.0/). Further distribution of this work must maintain attribution to the author(s) and the published article's title, journal citation, and DOI.

Recent developments in our group led to the implementation of nuclear magnetic resonance (NMR) spectroscopy in diamond anvil cells (DACs) at pressures approaching 100 GPa using magnetic flux tailoring Lenz lenses [12–14]. NMR spectroscopy is widely recognized [15–19] for its sensitivity to small electronic effects. In particular, Knight shift measurements provide a well-established technique to investigate the density of states of conduction electrons at the Fermi energy, enabling the detection of deviations from free-electron gas behavior or even electronic topological transitions of the Fermi surface and direct evidence of the Meissner-Ochsenfeld effect in the metal's superconducting state.

In density-functional-theory-based calculations, Peng *et al.* [20] demonstrate that in clathratelike metal hydrogen systems, such as LaH<sub>10</sub> or YH<sub>10</sub>, the nearest H-H distances should be  $\leq 1.5$  Å for the development of significant hydrogen-hydrogen interactions. In nonmagnetic fcc FeH, stable above 25 GPa [21], average H-H distances are in the range of 2.6–2.3 Å at 200 GPa [22], suggesting that  $P$ -induced H-H correlations are unlikely. As the synthesis of fcc FeH in a DAC is well established and the crystal structure well defined, hydrogenation and composition of FeH samples can be closely controlled. Therefore, fcc iron monohydride can be regarded as a reference system for our NMR-based approach to the investigation of the electronic structure of hydrogen in metal hydrides.

## II. EXPERIMENTAL METHODS

Two identical DACs of type BX90 [23] are prepared with two beveled diamond anvils with 100  $\mu\text{m}$  culets. Rhenium gaskets are indented to about 15  $\mu\text{m}$  thickness, and 40  $\mu\text{m}$  holes are laser cut in the flat face of the preindentation to form the sample cavity. Using physical and chemical vapor deposition techniques, the anvils are covered by a 1  $\mu\text{m}$ -thick layer of copper, and the metallic rhenium gaskets are sputtered with a 500 nm-thick layer of  $\text{Al}_2\text{O}_3$  for electrical insulation. Subsequently, using a focused ion beam, three Lenz lenses (LLs) are cut out of the copper layers covering the diamond anvils: (i) along the anvil's pavillion, (ii) on the beveled area, and (iii) on the 100  $\mu\text{m}$  culets [Fig. 1(a)]. This procedure is necessary to avoid damage due to sharp edges from the 8° bevel and the culet rim when cupping under compression occurs. The nuclear magnetic resonators used in this study can be regarded as a generalization of the recently introduced double-stage Lenz lenses [14], enabling its use for single-beveled diamond anvils with culet sizes of  $\leq 100 \mu\text{m}$ .

The cells are loaded by flooding the sample chamber with paraffin oil and then mixing fine iron powder of natural composition (Sigma-Aldrich, 4N purity) into it. Pressure in the sample chamber is estimated by the frequency shift of the first-order Raman peak of the diamond at its edge in the center of the sample cavity [Fig. 1(b)] [24,25].

The radio-frequency (rf) excitation coils are made using two identical 3 mm coils consisting of five turns of 150  $\mu\text{m}$

Teflon-insulated copper wire. Each coil is fixed around the diamonds on the respective backing plates and connected to form a Helmholtz coil, ensuring optimal inductive coupling into the LL resonator structures. NMR measurements are conducted at a magnetic field of 1 T using a sweepable electron spin resonance magnet with a 50-mm magnet pole distance and a Techmac Redstone spectrometer for solid-state NMR applications. NMR measurements prior to cell loading do not exhibit any detectable hydrogen signals within typical experimental parameters, showing the absence of spurious hydrogen signals stemming from other parts of the NMR probe.

From rf nutation experiments, an optimal 90° pulse of 4  $\mu\text{s}$  at an average pulse power of 40 W is established. This value does not change over the course of the experiment and is found to be valid for both DACs used. For measurements of spin-lattice relaxation rates, a saturation recovery pulse train consisting of 16 consecutive pulses is used. From the relation  $B_1 = \pi/(2\gamma_n t_{\pi/2})$ , with  $\gamma_n$  the nuclear gyromagnetic ratio and  $t_{\pi/2}$  the  $\pi/2$  pulse length, a  $B_1$  field of 4.7 mT is deduced. Using the FEMM 4.2 package, the high-frequency  $B_1$  field distribution across the 40  $\mu\text{m} \times 15 \mu\text{m}$  sample cavity is calculated using experimental parameters similar to the nutation experiments. An average  $B_1$  field of 4.8 mT is found, in excellent agreement with the nutation experiments. The introduced LL resonators show the required sensitivity.

All resonance frequency shifts are referenced relative to the hydrogen signal of the paraffin hydrogen reservoir

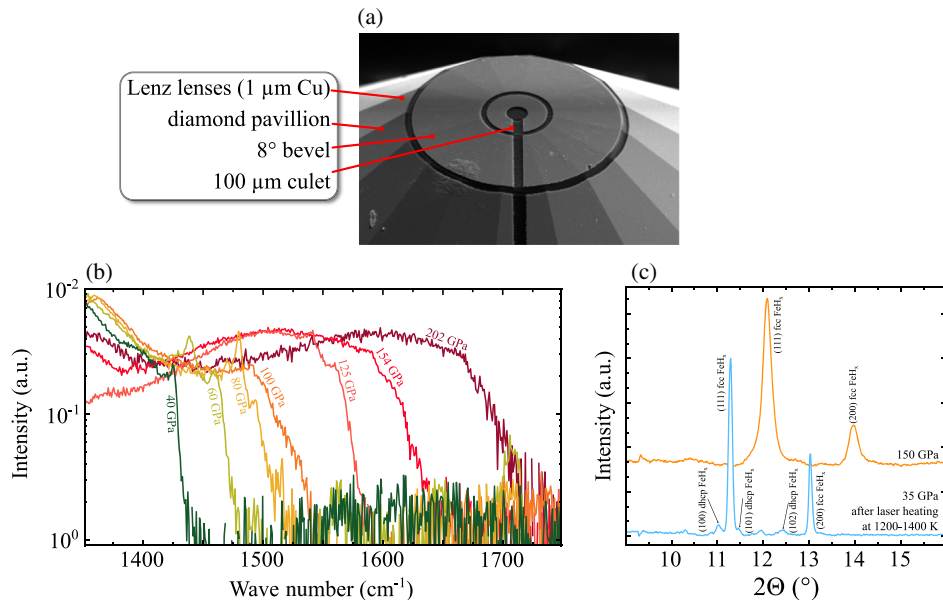


FIG. 1. (a) SEM image of the NMR Lenz lens resonator structure deposited and formed on the surface of a 100- $\mu\text{m}$  diamond anvil, (b) Raman spectra of the diamond edge at the center of the 100- $\mu\text{m}$  culets used for pressure calibration, and (c) x-ray diffraction patterns after sample synthesis (laser heating) at 35 GPa (blue line) and after compression to 150 GPa (orange line).

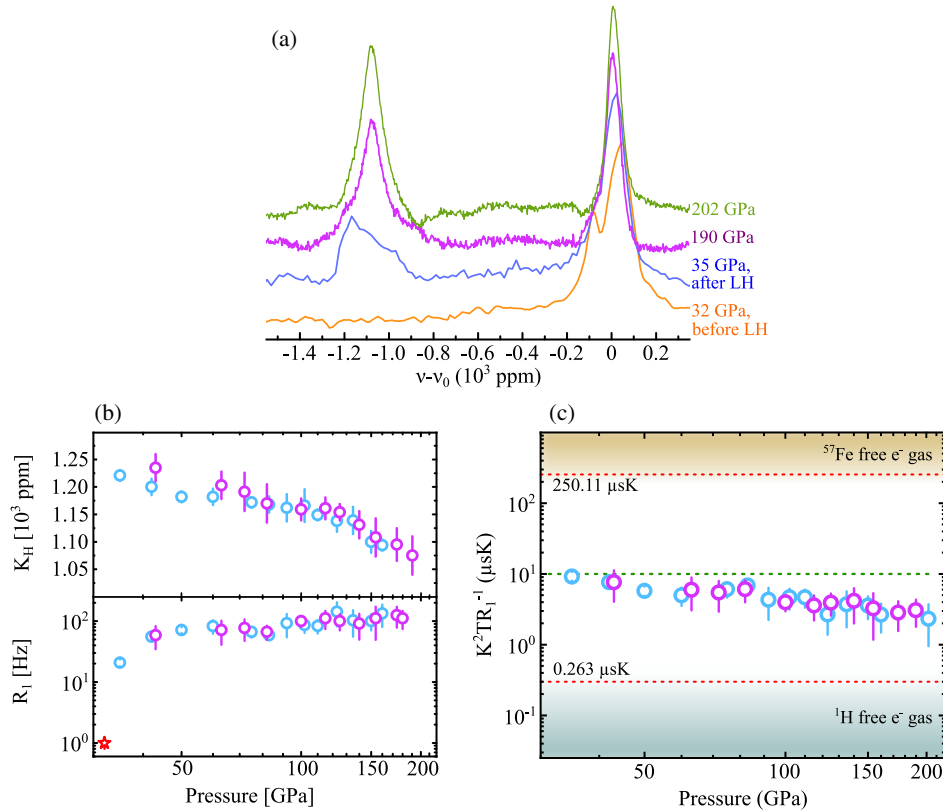


FIG. 2. (a) Hydrogen NMR spectra. Shown are spectra before laser heating at 32 GPa (orange line), directly after laser heating (blue line), and after compression to 190 and 202 GPa (purple and green line, respectively). (b) Summary of Knight shift  $K_H$  relative to the hydrogen reservoir (top) and the spin-lattice relaxation rates  $R_1$  (bottom). Blue and purple data points refer to data collected in cells 1 and 2, respectively. The red data point refers to the relaxation rate of the hydrogen reservoir prior to sample synthesis. (c) Pressure dependence of the Korrington ratio. Shaded areas qualitatively depict the regions expected for pure iron (top) and metallic hydrogen (bottom).

after laser heating. The values for the Knight shift (Fig. 2) are higher by a factor of 6 than for other transition metal hydrides [26]. The choice of the reference material can, in principle, lead to an intrinsic overestimate as we deviate from the standard shift reference, tetramethylsilane (TMS) [27]. However, TMS does not induce the reaction to form FeH at a high  $P$  and temperature ( $T$ ), to the best of our knowledge.

The DACs are pressurized initially to about 30 GPa, into the stability field of nonmagnetic hcp Fe, and subsequently laser heated to 1200 K. X-ray diffraction (XRD) powder patterns taken at PETRA III (beam line P02) and ESRF (ID-15) show reflections from FeH and no residual Fe signal [Fig. 1(c)], suggesting that iron has fully reacted with hydrogen from the paraffin reservoir. The most prominent diffraction peaks are those of fcc FeH previously identified [21,28]; a small amount of dhcp FeH $_x$  is also indexed.

As fcc FeH $_x$  is unstable at ambient conditions, the actual chemical composition cannot be measured directly using recovered samples. Narygina *et al.* [21] suggest that the

hydrogenation factor  $x$  can be estimated by considering the volume expansion of the fcc unit cell in response to the dissolution of hydrogen on the octahedral interstitial lattice sites of fcc Fe by

$$x = (V_{\text{FeH}_x} - V_{\text{Fe}}) / \Delta V_{\text{H}}, \quad (1)$$

with  $V_{\text{FeH}_x}$  and  $V_{\text{Fe}}$  the atomic volumes of iron hydride and fcc iron, respectively.  $\Delta V_{\text{H}}$  is the volume expansion due to hydrogenation. As the latter parameter is not well defined by other fcc-structured 3d transition metals at ambient conditions, the actual hydrogenation value  $x$  is estimated by comparing the recorded data with equations of state of FeH [21] and fcc iron [29]. Using this procedure,  $x = 1.0(1)$  in both DACs is found, close to stoichiometry. Further XRD measurements at 150 GPa suggest that fcc FeH remains stable with similar composition throughout the whole  $P$  range of this study.

Prior to laser heating,  $^1\text{H}$ -NMR spectra are recorded [Fig. 2(a)]: As the origin of the hydrogen signal is the

$C_nH_{2n+2}$  reservoir, a single NMR signal positioned at the Larmor frequency for hydrogens is observed. The center of gravity of the paraffin signal is found at 45.0737 MHz, corresponding to a polarizing magnetic field of  $B_0 = 1.058$  mT within the sample cavity. Small deviations of up to 10% in  $B_0$  are found to originate from a slightly different positioning of the DACs within the region of the highest magnetic field of the electromagnet but can be neglected, since the hydrogen reservoir serves as an internal reference. The recorded spectra of paraffin at 32 (cell 1) and 29 GPa (cell 2) are found to be similar to earlier  $^1\text{H}$ -NMR spectra of  $C_nH_{2n+2}$  in terms of linewidths and relaxation rates [12]. After laser heating, an additional intense signal is found at lower frequencies at about  $-1200$  ppm relative to the hydrogen reference [Fig. 2(a)]. Comparing signal intensities from spectra recorded after full relaxation of both independent spin systems, we determine an intensity ratio of about 4:7 of FeH to  $C_nH_{2n+2}$  in cell 1 and 1:5 in cell 2. These ratios are found to be constant at all  $P$ , suggesting that further reaction of hydrogen with the iron powder during cold compression cycles does not occur.

### III. COMPUTATIONAL DETAILS

All *ab initio* calculations performed are based on the Kohn-Sham density functional theory and are performed with QUANTUM ESPRESSO [30,31] using the projector augmented wave approach [32]. We use the generalized gradient approximation by Perdew-Burke-Ernzerhof [33] to exchange and correlation with corresponding potential files; for Fe, we use a valence electron configuration that includes electronic states  $3s$  and higher, applicable to extreme pressure [34].

Convergence tests for the electronic band structure and density of state calculations lead to reciprocal space sampling with a Monkhorst-Pack [35]  $k$ -point grid of  $32 \times 32 \times 32$  and a cutoff energy for the plane wave expansion of 120 Ry. In addition to the total electronic density of states, site and orbital projections are computed, with particular attention to the crystal field splitting of the  $3d$  electronic states into the  $e_g$  and  $t_{2g}$  orbitals.

In order to identify regions of charge localization, we use the electron localization function (ELF) [36] that quantifies the probability of finding two electrons in close proximity by the ratio of a computed charge density and its spatial derivative to the value of the homogeneous electron gas of the same density.

### IV. KNIGHT SHIFT IN IRON HYDRIDE

As both stable iron hydride phases, fcc and dhcp, are thought to be metallic [37,38], the influence of hyperfine interaction of conduction electrons with the nuclei must be taken into account to explain the NMR signal. For transition metal hydrides, the magnetic susceptibility ( $\chi$ ) can be written as a sum of several contributions,  $\chi = \chi_s + \chi_d + \chi_o + \chi_{\text{dia}}$ ,

stemming from spin interactions with  $s$ - or  $d$ -conduction electrons, the orbital paramagnetic, and the diamagnetic contribution of the ion cores, respectively. Therefore, the electron-nuclear hyperfine interaction, described in terms of the Knight shift  $K_{\text{tot}}$  and the spin-lattice relaxation rate  $R_1$  [39,40], are caused by various mechanisms [41]:

$$\begin{aligned} K_{\text{tot}} &= K_s + K_d + K_o \\ &= \frac{1}{A\mu_B} (H_{\text{hf}}^s \chi_s + H_{\text{hf}}^d \chi_d + H_{\text{hf}}^o \chi_o) \end{aligned} \quad (2)$$

and

$$\begin{aligned} R_1 &= 4\pi\mu_0^2 \gamma_n^2 \hbar k_B T \{ [H_{\text{hf}}^s N_s(E_F)]^2 \\ &\quad + [H_{\text{hf}}^d N_d(E_F)]^2 q + [H_{\text{hf}}^o N_d(E_F)]^2 p \}, \end{aligned} \quad (3)$$

where  $A$  is Avogadro's constant and  $\mu_B$  the Bohr magneton. The hyperfine fields  $H_{\text{hf}}^s$ ,  $H_{\text{hf}}^d$ , and  $H_{\text{hf}}^o$  at the nucleus under investigation originate from the following mechanisms: (i) contact interaction of  $s$  conduction electrons with the nucleus, (ii) core polarization of  $s$  orbitals caused by uncompensated  $d$  electrons, and (iii) the effect of orbital motions of  $d$  electrons.  $N_s(E_F)$  and  $N_d(E_F)$  in Eq. (2) are the  $s$ - and  $d$ -electron density of states at the Fermi energy, respectively. The factors  $p$  and  $q$  are reduction factors depending on  $d$ -orbital degeneracy at  $E_F$ .

For a free-electron Fermi gas, we can substitute  $\chi_{(s,d)} = 2\mu_0\mu_B^2 N_{(s,d)}(E_F)$  in Eq. (2), leading to a reduced representation of the Knight shift:

$$\begin{aligned} K_{\text{tot}} &= 2\mu_0\mu_B [H_{\text{hf}}^s N_s(E_F) + H_{\text{hf}}^d N_d(E_F)] \\ &\quad + \frac{1}{A\mu_B} H_{\text{hf}}^o \chi_o. \end{aligned} \quad (4)$$

Equation (4) demonstrates that various mechanisms producing hyperfine fields at the hydrogen site need to be taken into account. However, as the  $1s$  electronic states of hydrogen and the  $4s$  states of iron typically lie far below and above the Fermi energy, respectively, it seems reasonable to assume their contribution to  $K_{\text{tot}}$  to be negligible to first approximation in FeH.

The effect of orbital motion of  $3d$  electrons on the hydrogen Knight shift ( $K_H$ ) is expected to be virtually nonexistent, as such an interaction would dominate Eq. (4) and lead to positive values of  $K_H$  which are not observed in other MH systems measured at ambient conditions [41–44]. Also, considering the good correlation between  $K_H$  and  $N_{t_{2g}}(E_F)$  (discussed in greater detail below), an influence of spin orbit coupling on the  $^1\text{H}$ -NMR spectra can be ruled out (Fig. 3). Therefore, both Eqs. (3) and (4) are reduced to their  $d$ -electron core polarization contribution, with a Korringa-type [45] relation given by

$$\frac{K_H^2 T}{R_1} = \frac{\hbar}{4\pi k_B} \left( \frac{\gamma_e}{\gamma_n} \right)^2 q. \quad (5)$$

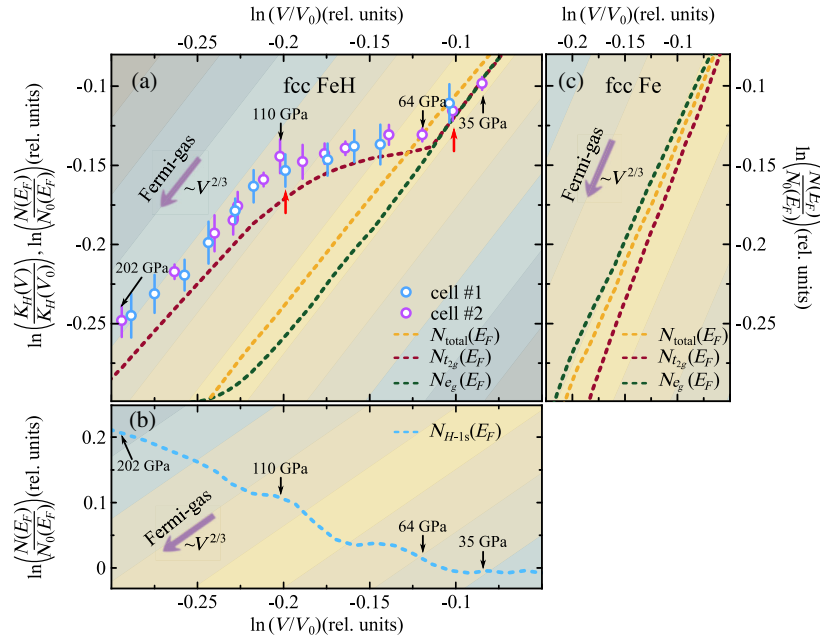


FIG. 3. Comparison of experimental data and *ab initio* electronic density of states calculations. (a) Double logarithmic power plot of relative changes in  $K_H$  and  $N(E_F)$  as a function of the relative volume. Experimental data points (blue and purple) have been normalized to  $V_0$  using the equation of state from Narygina *et al.* [21] and extrapolated values of  $K_H(V_0)$ . Note that using complementary equation of state data from Thompson *et al.* [28] or Pépin *et al.* [22] does not affect our conclusions. The dashed lines (splines through computed values) show the dependence of  $N_{total}(E_F)$ ,  $N_{t_{2g}}(E_F)$ , and  $N_{e_g}(E_F)$ . The diagonal color strips are guides to the eye depicting a  $\propto V^{2/3}$  scaling for free-electron Fermi-gas-like behavior [as  $N(E) \propto V\sqrt{E}$  and  $E_F \propto V^{-2/3}$  [46],  $N(E_F) \propto V \cdot \sqrt{V^{-2/3}} \propto V^{2/3}$ ]. Black arrows denote respective pressures points; red arrows show data recorded under decompression. (b) Evolution of  $N_{H-1s}(E_F)$ . Indicated pressure markers are related to the experimental data points from (a). (c) Volume dependence of  $N_{total}(E_F)$ ,  $N_{t_{2g}}(E_F)$ , and  $N_{e_g}(E_F)$  for fcc Fe over a similar compression range.

For cubic lattices, the reduction factor  $q$  can be described by  $q = \frac{1}{3}f^2 + \frac{1}{2}(1-f)^2$ , where  $f$  is the fractional character of  $t_{2g}$  orbitals at the Fermi surface [47,48], determining the deviation from the free-electron value given by  $S = [\hbar/(4\pi k_B)](\gamma_e/\gamma_n)^2$  [15], with  $\gamma_e$  the gyromagnetic ratio of the electron.

In general, the Korringa-ratio constitutes an indicator for metallicity of a given material [15] using the volume independence of Eq. (5). As the Korringa ratio depends on only physical constants, values for the free-electron gas behavior for every metallic system can be readily estimated. For FeH, two different limiting scenarios can be identified: (i) pure  $^{57}\text{Fe}$  metal with  $K^2T/R_1 = 250.11 \mu\text{sK}$  and (ii) electronic Fermi-gas-like behavior of metallic hydrogen with a value of  $0.263 \mu\text{sK}$ . The Korringa ratio for the binary system consisting of Fe and H can be anticipated to lie in between these extreme values.

## V. RESULTS AND DISCUSSION

At approximately 30 GPa and before laser heating, only a single NMR signal is observed [Fig. 2(a)], originating

from the paraffin hydrogen reservoir which has been characterized in earlier experiments [12]. After FeH synthesis at 1200 K, an additional  $^1\text{H-NMR}$  signal appears at about  $-1200$  ppm relative to the paraffin hydrogen reservoir (Fig. 2). If this huge shift is due to the occurrence of  $K_H$  in the metallic state [39], nuclear relaxation, as described by Heitler and Teller [49], must occur as well. We observe, indeed, that, in response to FeH synthesis, the spin-lattice relaxation rates ( $R_1$ ) increase by more than one order of magnitude from approximately 1 Hz in the hydrogen reservoir to approximately 20 Hz in the spin system associated with the additional signal [Fig. 2(b)].

Combining shift and relaxation rates, the Korringa ratio [Eq. (5)] should yield values intermediate to those for pure  $^{57}\text{Fe}$  metal and a Fermi-gas-like value of the proton site [Fig. 3(c)]. The value of the Korringa ratio recorded directly after sample synthesis is found to be approximately  $10 \mu\text{sK}$ , halfway in magnitude between these two values [Fig. 2(c)]. Therefore, the appearance of the additional signal can be attributed to the formation of metallic FeH in the DAC. Similar  $^1\text{H-NMR}$  spectra of other metal-hydride systems, synthesized at ambient conditions, confirm this

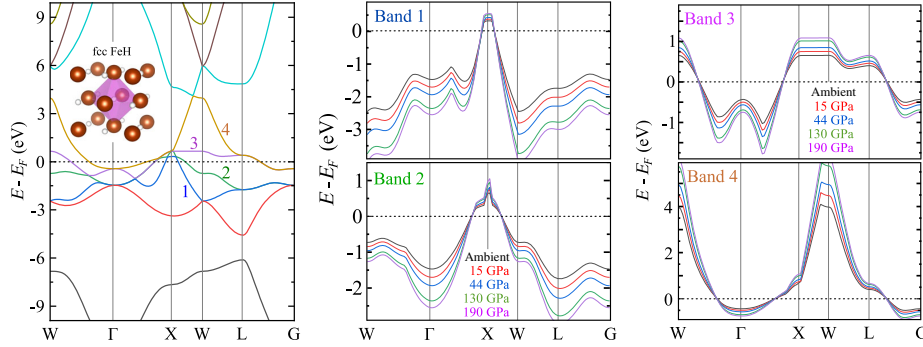


FIG. 4. Calculated band structure of fcc FeH. The left panel shows the band structure at ambient pressure, the two right panels the pressure evolution of four bands crossing the Fermi energy ( $E_F$ ), identified on the left.

conclusion [41,50]. Figure 2(c) also shows the pressure evolution of the Korringa ratio which should be volume independent in metallic systems [Eq. (5)]. However, a distinct  $P$  dependence is observed between 30 and 202 GPa. To investigate this phenomenon, we focus on the analysis of the volume dependence of  $K_H$ .

Figure 3 shows a double logarithmic power plot of the relative volumes, using the equation of state from Narygina *et al.* [21], against relative changes in the Knight shift. Three distinct regions can be identified: (i) Up to 64 GPa, the exponent of the Knight shift ratio closely follows a Fermi-gas electronic behavior with  $\propto V^{2/3}$ , (ii) a deviation from metallic scaling exponents occurs between 64 and 110 GPa, and (iii) the reoccurrence of free-electron gas behavior from 110 GPa to highest  $P$ . After compression and data collection up to 202 GPa, one of the DAC experiments is decompressed to approximately 100 GPa and subsequently to 33 GPa [red arrows in Fig. 3(a)]. NMR spectra collected on decompression agree with those obtained during compression, showing that the observed effect is fully reversible. As x-ray diffraction data do not show any sign of a structural phase transition [22,28], the origin of this observation should be linked to changes in the electronic environment of the hydrogens in FeH.

The computed electronic band structure (Fig. 4) and density of states do not indicate any discontinuities close to  $E_F$ , such as van Hove singularities [51]. Therefore, topological transitions of the Fermi surface [52], which would influence both spin shift and relaxation rates, can be excluded. Values of the total density of states at  $E_F$ ,  $N_{\text{total}}(E_F)$ , as well as its projection on the  $3d-t_{2g}$  and  $e_g$  states,  $N_{t_{2g}}(E_F)$  and  $N_{e_g}(E_F)$ , respectively, from the calculations are included in Fig. 3(a). The volume dependence of  $N_{t_{2g}}(E_F)$  closely follows the NMR spin shifts to 64 GPa. Above this  $P$ , experimental data points and  $N_{t_{2g}}(E_F)$  diverge beyond experimental errors.

The hydrogen Knight shift is the sum of interactions due to core polarization of uncompensated  $d$  orbitals and

contact interaction of  $s$  electrons with the nuclei [Eq. (4)]. At ambient conditions, the latter interaction can be regarded as negligible due to the density of states at  $E_F$  being almost zero for the hydrogen  $1s$  electron,  $N_{H-1s}(E_F)$  [Fig. 3(b)]. The contribution of  $N_{H-1s}(E_F)$  to the total density of states begins to increase around 64 GPa and continuously rises with  $P$ , up to 202 GPa, the highest  $P$  considered. This effect can qualitatively explain the observed offset between experimental data and calculated density of state values.

Figure 3(c) shows the respective volume dependence of the density of states at  $E_F$  of the  $3d$  electrons for fcc-Fe over the same compression range as the FeH data. The  $P$ -dependent effects observed on the density of states of the  $3d-t_{2g}$  orbitals in fcc FeH [Fig. 3(a)] are not present in fcc Fe. This difference allows us to conclude that they are caused by the presence of hydrogen atoms. Both the scaling anomaly in  $N_{t_{2g}}(E_F)$  and the continuous increase in  $N_{H-1s}(E_F)$  with compression suggest a shift of conduction electron density between iron and hydrogen atoms in FeH.

In order to elucidate this possibility, we map the ELF in three different crystal planes [(1 0 0), (1 1 0), and (1 1 2)] at compressions between  $V/V_0 = 1.0$  and  $V/V_0 = 0.61$  (21 steps) and consider the correlations between the evolution of the ELF maps and the data shown in Fig. 3 (Movie S1 in Supplemental Material [53]); Fig. 5 presents the ELF maps for  $V/V_0 = 0.9$  and  $V/V_0 = 0.69$ , corresponding to approximately 30 and approximately 200 GPa, respectively.

At  $V/V_0 = 0.9$ , electron clouds associated with Fe and H atoms are localized, evidencing the ionic character of FeH. Regions exhibiting Fermi-gas electronic behavior, i.e., ELF values of 0.5, start to develop and spread at  $V/V_0 < 0.88$ , which are particularly pronounced in the (110) and (112) planes. These regions of increased electron density connect at  $V/V_0 < 0.78$ , corresponding to pressures of 80–90 GPa, forming an interconnecting network with respect to the hydrogen nuclei. At  $V/V_0 < 0.73$ , the nearest-neighbor H-H bonds are bridged as well. Strikingly, the deviation from free-electron gas behavior

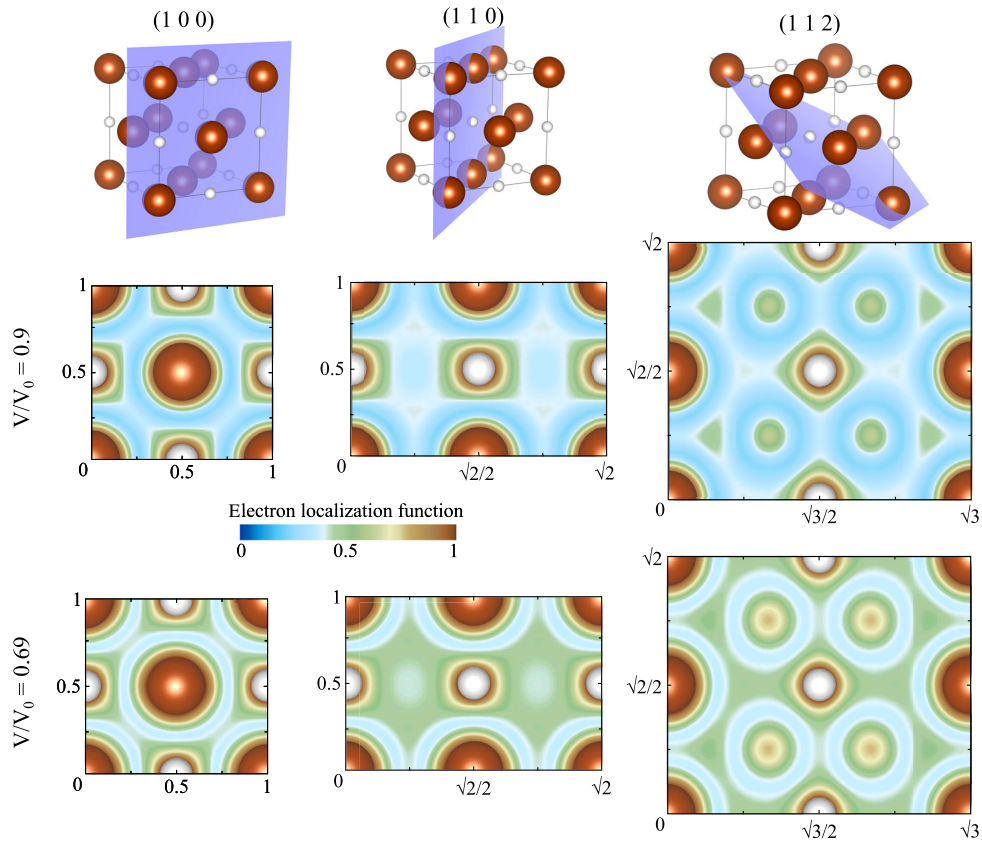


FIG. 5. Electron localization function maps in three major crystal planes at a compression of  $V/V_0 = 0.9$  and  $0.69$ , corresponding to 30 and 200 GPa, respectively (for further compression points, see Movie S1 in Supplemental Material [53]). Brown spheres represent iron atoms, white spheres hydrogen. Green areas (ELF  $\sim 0.5$ ) correspond to Fermi-gas-like regions of free electrons.

observed for  $V/V_0 = 0.88$  coincides with the increase of electron density in the interstitial regions of FeH. The reemergence of Fermi-gas behavior above 110 GPa corresponds to the connection of these areas of enhanced electron density. The pronounced increase in  $N_{H-1s}(E_F)$  also correlates qualitatively with both the formation and connection of these areas.

## VI. CONCLUSIONS

Combining experimental observations from NMR measurements and *ab initio* computational results, we propose the following qualitative explanation for the high- $P$  evolution of FeH: With increasing  $P$ , the electron density from partially uncompensated  $3d-t_{2g}$  Fe orbitals in FeH is pushed towards the hydrogen electron clouds. The successive addition of charges leads to the formation of an intercalating free-electron sublattice of connected hydrogen atoms, exhibiting a continuous enhancement of the electronic density of states of hydrogen at  $E_F$ . Our data suggest that this effect can be observed by NMR when average H-H

distances become smaller than approximately  $2.5 \text{ \AA}$ , which is significantly larger than expected based on previous computational work.

This result suggests that  $P$ -induced interactions between hydrogen and the transition metal atoms as well as between H atoms themselves can occur and influence electronic properties of metal hydrides at much lower  $P$  than previously anticipated. The experimental findings, supported by *ab initio* calculations, suggest that other candidates for phonon-mediated high- $T_c$  superconductivity may be found far off the proclaimed “lability belt,” including the rare-earth sodalite-clathrate superhydrides [54].

The data supporting the findings of this study are available from the corresponding author upon reasonable request.

## ACKNOWLEDGMENTS

We thank Nobuyoshi Miyajima and Katharina Marquardt for help with the FIB milling. We also thank Caterina Melai, Serena Dominijanni, and Catherine McCammon for help

with XRD measurements. N. D. and L. D. thank the German Research Foundation [Deutsche Forschungsgemeinschaft (DFG) Projects No. DU 954/11-1, No. DU 393/13-1, and No. DU 393/9-2] and the Federal Ministry of Education and Research, Germany (BMBF, Grant No. 5K16WC1) for financial support. S. P. and F. T. were financed by the German Research Foundation (DFG Projects No. PE 2334/1-1 and No. STE 1105/13-1, both in the research unit FOR 2440).

T. M. and L. D. designed the experiment. T. M., S. K., and S. P. prepared the DACs and NMR resonators. S. K. performed focused ion beam cutting as well as structure refinement after laser heating. L. D. performed the sample synthesis in the DACs. S. C. and T. F. as well as S. D. and C. M. performed XRD measurements at DESY and ESRF, respectively. F. T. and G. S.-N. performed the calculations and analyzed the results. T. M., F. T., G. S.-N., N. D. and L. D. performed the data analysis and wrote the manuscript.

- 
- [1] R. Mohtadi and S. I. Orimo, *The Renaissance of Hydrides as Energy Materials*, *Nat. Rev. Mater.* **2**, 16091 (2016).
- [2] L. Zhang, Y. Wang, J. Lv, and Y. Ma, *Materials Discovery at High Pressures*, *Nat. Rev. Mater.* **2**, 17005 (2017).
- [3] L. P. Gor'kov and V. Z. Kresin, *Pressure and High- $T_c$  Superconductivity in Sulfur Hydrides*, *Sci. Rep.* **6**, 25608 (2016).
- [4] E. Zurek, R. Hoffmann, N. W. Ashcroft, A. R. Oganov, and A. O. Lyakhov, *A Little Bit of Lithium Does a Lot for Hydrogen*, *Proc. Natl. Acad. Sci. U.S.A.* **106**, 17640 (2009).
- [5] T. Jarlborg and A. Bianconi, *Breakdown of the Migdal Approximation at Lifshitz Transitions with Giant Zero-Point Motion in the  $H_3S$  Superconductor*, *Sci. Rep.* **6**, 24816 (2016).
- [6] A. Bianconi and T. Jarlborg, *Superconductivity above the Lowest Earth Temperature in Pressurized Sulfur Hydride*, *Europhys. Lett.* **112**, 37001 (2015).
- [7] A. P. Drozdov, M. I. Erements, and I. A. Troyan, *Superconductivity above 100 K in  $PH_3$  at High Pressures*, *arXiv:1508.06224*.
- [8] M. Somayazulu, M. Ahart, A. K. Mishra, Z. M. Geballe, M. Baldini, Y. Meng, V. V. Struzhkin, and R. J. Hemley, *Evidence for Superconductivity above 260 K in Lanthanum Superhydride at Megabar Pressures*, *Phys. Rev. Lett.* **122**, 027001 (2019).
- [9] A. P. Drozdov, M. I. Erements, I. A. Troyan, V. Ksenofontov, and S. I. Shylin, *Conventional Superconductivity at 203 Kelvin at High Pressures in the Sulfur Hydride System*, *Nature (London)* **525**, 73 (2015).
- [10] D. V. Semenok, I. A. Kruglov, A. G. Kvashnin, and A. R. Oganov, *On Distribution of Superconductivity in Metal Hydrides*, *arXiv:1806.00865*.
- [11] D. V. Semenok, A. G. Kvashnin, I. A. Kruglov, and A. R. Oganov, *Actinium Hydrides  $AcH_{10}$ ,  $AcH_{12}$ , and  $AcH_{16}$  as High Temperature Conventional Superconductors*, *J. Phys. Chem. Lett.* **9**, 1920 (2018).
- [12] T. Meier, N. Wang, D. Mager, J. G. Korvink, S. Petitgirard, and L. Dubrovinsky, *Magnetic Flux Tailoring through Lenz Lenses for Ultrasmall Samples: A New Pathway to High-Pressure Nuclear Magnetic Resonance*, *Sci. Adv.* **3**, eaao5242 (2017).
- [13] T. Meier, S. Petitgirard, S. Khandarkhaeva, and L. Dubrovinsky, *Observation of Nuclear Quantum Effects and Hydrogen Bond Symmetrisation in High Pressure Ice*, *Nat. Commun.* **9**, 2766 (2018).
- [14] T. Meier, S. Khandarkhaeva, S. Petitgirard, T. Körber, A. Lauerer, E. Rössler, and L. Dubrovinsky, *NMR at Pressures up to 90 GPa*, *J. Magn. Reson.* **292**, 44 (2018).
- [15] G. C. Carter, L. H. Bennett, and D. J. Kahan, *Metallic Shifts in NMR*, first ed. (Pergamon Press, Oxford, 1977).
- [16] S. H. Baek, H. Lee, S. E. Brown, N. J. Curro, E. D. Bauer, F. Ronning, T. Park, and J. D. Thompson, *NMR Investigation of Superconductivity and Antiferromagnetism in  $CaFe_2As_2$  under Pressure*, *Phys. Rev. Lett.* **102**, 227601 (2009).
- [17] N. Fujiwara, N. Mori, Y. Uwatoko, T. Matsumoto, N. Motoyama, and S. Uchida, *Spin Fluctuation in  $Sr_2Ca_{12}Cu_{24}O_{41}$  under High Pressure up to 3.0 GPa*, *Physica (Amsterdam)* **388C–389C**, 229 (2003).
- [18] T. Meier, *Journey to the Centre of the Earth: Jules Vernes' Dream in the Laboratory from an NMR Perspective*, *Prog. Nucl. Magn. Reson. Spectrosc.* **106–107**, 26 (2018).
- [19] T. Meier, S. Reichardt, and J. Haase, *High-Sensitivity NMR beyond 200,000 Atmospheres of Pressure*, *J. Magn. Reson.* **257**, 39 (2015).
- [20] F. Peng, Y. Sun, C. J. Pickard, R. J. Needs, Q. Wu, and Y. Ma, *Hydrogen Clathrate Structures in Rare Earth Hydrides at High Pressures: Possible Route to Room-Temperature Superconductivity*, *Phys. Rev. Lett.* **119**, 107001 (2017).
- [21] O. Narygina, L. S. Dubrovinsky, C. A. McCammon, A. Kurnosov, I. Y. Kantor, V. B. Prakapenka, and N. A. Dubrovinskaia, *X-Ray Diffraction and Mössbauer Spectroscopy Study of fcc Iron Hydride FeH at High Pressures and Implications for the Composition of the Earth's Core*, *Earth Planet. Sci. Lett.* **307**, 409 (2011).
- [22] C. M. Pépin, A. Dewaele, G. Geneste, P. Loubeyre, and M. Mezouar, *New Iron Hydrides under High Pressure*, *Phys. Rev. Lett.* **113**, 265504 (2014).
- [23] I. Kantor, V. Prakapenka, A. Kantor, P. Dera, A. Kurnosov, S. Sinogeikin, N. Dubrovinskaia, and L. Dubrovinsky, *BX90: A New Diamond Anvil Cell Design for X-Ray Diffraction and Optical Measurements*, *Rev. Sci. Instrum.* **83**, 125102 (2012).
- [24] Y. Akahama and H. Kawamura, *High-Pressure Raman Spectroscopy of Diamond Anvils to 250 GPa: Method for Pressure Determination in the Multimegabar Pressure Range*, *J. Appl. Phys.* **96**, 3748 (2004).
- [25] Y. Akahama and H. Kawamura, *Pressure Calibration of Diamond Anvil Raman Gauge to 310 GPa*, *J. Appl. Phys.* **100**, 043516 (2006).
- [26] M. S. Conradi, M. P. Mendenhall, T. M. Ivancic, E. A. Carl, C. D. Browning, P. H. L. Notten, W. P. Kalisvaart, P. C. M. M. Magusin, R. C. Bowman, S. J. Hwang, and N. L. Adolphi, *NMR to Determine Rates of Motion and Structures in Metal-Hydrides*, *J. Alloys Compd.* **446–447**, 499 (2007).
- [27] G. Maniara, K. Rajamoorthi, S. Rajan, and G. W. Stockton, *Method Performance and Validation for Quantitative*

- Analysis by  $^1\text{H}$  and  $^{31}\text{P}$  NMR Spectroscopy. Applications to Analytical Standards and Agricultural Chemicals*, *Anal. Chem.* **70**, 4921 (1998).
- [28] E. C. Thompson, A. H. Davis, W. Bi, J. Zhao, E. E. Alp, D. Zhang, E. Greenberg, V. B. Prakapenka, and A. J. Campbell, *High-Pressure Geophysical Properties of Fcc Phase  $\text{FeH}_x$* , *Geochem. Geophys.* **19**, 305 (2018).
- [29] T. Komabayashi and Y. Fei, *Internally Consistent Thermodynamic Database for Iron to the Earth's Core Conditions*, *J. Geophys. Res. Solid Earth* **115**, B03202 (2010).
- [30] P. Giannozzi *et al.*, *QUANTUM ESPRESSO: A Modular and Open-Source Software Project for Quantum Simulations of Materials*, *J. Phys. Condens. Matter* **21**, 395502 (2009).
- [31] P. Giannozzi *et al.*, *Advanced Capabilities for Materials Modelling with Quantum ESPRESSO*, *J. Phys. Condens. Matter* **29**, 465901 (2017).
- [32] P. E. Blöchl, *Projector Augmented-Wave Method*, *Phys. Rev. B* **50**, 17953 (1994).
- [33] J. P. Perdew, K. Burke, and M. Ernzerhof, *Generalized Gradient Approximation Made Simple*, *Phys. Rev. Lett.* **77**, 3865 (1996).
- [34] L. Stixrude, *Structure of Iron to 1 Gbar and 40 000 K*, *Phys. Rev. Lett.* **108**, 055505 (2012).
- [35] H. J. Monkhorst and J. D. Pack, *Special Points for Brillouin-Zone Integrations*, *Phys. Rev. B* **13**, 5188 (1976).
- [36] A. D. Becke and K. E. Edgecombe, *A Simple Measure of Electron Localization in Atomic and Molecular Systems*, *J. Chem. Phys.* **92**, 5397 (1990).
- [37] C. Elsässer, J. Zhu, S. G. Louie, B. Meyer, M. Fähnle, and C. T. Chan, *Ab Initio Study of Iron and Iron Hydride: II. Structural and Magnetic Properties of Close-Packed Fe and FeH*, *J. Phys. Condens. Matter* **10**, 5113 (1998).
- [38] C. Elsässer, H. Krimmel, M. Fähnle, S. G. Louie, and C. T. Chan, *Ab Initio Study of Iron and Iron Hydride: III. Vibrational States of H isotopes in Fe, Cr and Ni*, *J. Phys. Condens. Matter* **10**, 5131 (1998).
- [39] W. D. Knight, *Nuclear Magnetic Resonance Shift in Metals*, *Phys. Rev.* **76**, 1259 (1949).
- [40] C. H. Townes, C. Herring, and W. D. Knight, *The Effect of Electronic Paramagnetism on Nuclear Magnetic Resonance Frequencies in Metals*, *Phys. Rev.* **77**, 852 (1950).
- [41] R. Goring, R. Lukas, and K. Bohmhammel, *Multipulse NMR Investigation of Band Structure in Titanium Hydride: Proton Knight Shift and Spin-Lattice Relaxation*, *J. Phys. C* **14**, 5675 (1981).
- [42] S. Kazama and Y. Fukai, *Local Electronic Environment of Protons in  $\text{VH}_x$  Alloys: Knight Shift and  $T_1$  of Proton NMR*, *J. Phys. Soc. Jpn.* **42**, 119 (1977).
- [43] S. Kazama and Y. Fukai, *High Resolution Measurements of Proton NMR in  $\text{VH}_x$ ,  $\text{NbH}_x$  and  $\text{TaH}_x$ : Proton Knight Shift and Magnetic Susceptibility*, *J. Less-Common Met.* **53**, 25 (1977).
- [44] D. S. Schreiber and L. D. Graham, *On the Proton Knight Shift in Metallic  $\text{VH}_{0.66}$* , *J. Chem. Phys.* **43**, 2573 (1965).
- [45] J. Korringa, *Nuclear Magnetic Relaxation and Resonance Line Shift in Metals*, *Physica (Utrecht)* **16**, 601 (1950).
- [46] G. Czycholl, *Theoretische Festkörperphysik*, third ed. (Springer, Berlin, 2008).
- [47] Y. Yafet and V. Jaccarino, *Nuclear Spin Relaxation in Transition Metals*, *Phys. Rev.* **133**, A1630 (1964).
- [48] A. Narath and H. T. Weaver, *Effects of Electron-Electron Interactions on Nuclear Spin-Lattice Relaxation Rates and Knight Shifts in Alkali and Noble Metals*, *Phys. Rev.* **175**, 373 (1968).
- [49] W. Heitler and E. Teller, *Time Effects in the Magnetic Cooling Method. I*, *Proc. R. Soc. A* **155**, 629 (1936).
- [50] S. D. Goren, C. Korn, H. Riesemeier, E. Rossler, and K. Lüders, *Titanium Knight Shift in Titanium Hydride*, *Phys. Rev. B* **34**, 6917 (1986).
- [51] G. E. Volovik, *Topological Lifshitz Transitions*, *Low Temp. Phys.* **43**, 47 (2017).
- [52] I. M. Lifshitz, *Anomalies of Electron Characteristics of a Metal in the High Pressure Region*, *Sov. Phys. JETP* **11**, 1130 (1960).
- [53] See Supplemental Material at <http://link.aps.org/supplemental/10.1103/PhysRevX.9.031008> for animation of all ELF maps and electronic density of states calculations in combination with experimental data.
- [54] C. Heil, S. Di Cataldo, G. B. Bachelet, and L. Boeri, *Superconductivity in Sodalite-like Yttrium Hydride Clathrates*, *Phys. Rev. B* **99**, 220502 (2019).

## 5.4 Proton Mobility in Metallic Copper Hydride

The following section contains the manuscript and the supplementary material:

*„Proton Mobility in Metallic Copper Hydride from High Pressure  
Nuclear Magnetic Resonance “*

Thomas Meier\*, Florian Trybel\*, Giacomo Criniti, Dominique Laniel, Saiana  
Khandarkhaeva, Egor Koemets, Timofey Fedotenko, Konstantin Glazyrin, Michael  
Hanfland, Maxim Bykov, Gerd Steinle-Neumann, Natalia Dubrovinskaia  
and Leonid Dubrovinsky

Status: Submitted to *Physical Review B*  
(Submitted 21 July 2020, Revised 21 August 2020)

and the related supplementary material

## Proton Mobility in Metallic Copper Hydride from High Pressure Nuclear Magnetic Resonance

Thomas Meier<sup>1\*</sup>, Florian Trybel<sup>1</sup>, Giacomo Criniti<sup>1</sup>, Dominique Laniel<sup>2</sup>, Saiana Khandarkhaeva<sup>1</sup>, Egor Koemets<sup>1</sup>, Timofey Fedotenko<sup>2</sup>, Konstantin Glazyrin<sup>3</sup>, Michael Hanfland<sup>4</sup>, Maxim Bykov<sup>5</sup>, Gerd Steinle-Nemann<sup>1</sup>, Natalia Dubrovinskaia<sup>2,6</sup> and Leonid Dubrovinsky<sup>1</sup>

<sup>1</sup>Bayerisches Geoinstitut, Universität Bayreuth, 95440 Bayreuth, Germany

<sup>2</sup>Material Physics and Technology at Extreme Conditions, Laboratory of Crystallography, Universität Bayreuth, 95440 Bayreuth, Germany

<sup>3</sup>Deutsches Elektronen-Synchrotron (DESY), 22603 Hamburg, Germany

<sup>4</sup>European Synchrotron Radiation Facility (ESRF), 38043 Grenoble Cedex, France

<sup>5</sup>Department of Mathematics, Howard University, 2400 Sixth Street NW, Washington, DC 20059 (USA)

<sup>6</sup>Department of Physics, Chemistry and Biology (IFM), Linköping University, SE-581 83, Linköping, Sweden

\*[thomas.meier@uni-bayreuth.de](mailto:thomas.meier@uni-bayreuth.de)

The atomic and electronic structures of Cu<sub>2</sub>H and CuH have been investigated by high-pressure nuclear magnetic resonance spectroscopy up to 96 GPa, X-ray diffraction up to 160 GPa and density functional theory-based calculations. Metallic Cu<sub>2</sub>H was synthesized at a pressure of 40 GPa, and semi-metallic CuH at 90 GPa, found stable up to 160 GPa. For Cu<sub>2</sub>H, experiments and computations show an anomalous increase in the electronic density of state at the Fermi level for the hydrogen 1s states and the formation of a hydrogen network in the pressure-range 43-58 GPa, together with high <sup>1</sup>H mobility of  $\sim 10^{-7}$  cm<sup>2</sup>/s. A comparison of these observations with results on FeH suggests that they could be common features in metal hydrides.

### 1. Introduction

Discovered in 1844 [1], metal hydrides are now of great interest in light of their potential as hydrogen storage and high-temperature superconducting materials [2–5]. Characterizing their stability, composition, electronic and transport properties provides crucial insight for a variety of applications, but metal hydrides continue to be enigmatic due to the highly variable metal-hydrogen bond. Following hydrogen uptake at elevated pressure ( $P$ ) (and temperature  $T$ ), the electronic structure of metal hydrides can change significantly, giving rise to their semiconducting [6], metallic [7] to even superconducting behavior [3].

Hexagonal copper hydride (with wurtzite-type structure) was one of the first metal hydrides discovered in the XIX century [1]. As a highly reactive compound, it readily decomposes to the elements [8]. Over the past two decades, a number of high- $P$  copper hydrides were synthesized in the diamond anvil cell (DAC):

(i) Using dehydrogenated Cu and H<sub>2</sub>, cubic CuH<sub>0.4</sub> with an *fcc* arrangement of Cu atoms was formed at  $P > 14$  GPa [9]. By contrast, in the same work no reaction was observed when Cu foil was used as a starting material, suggesting that CuH<sub>0.4</sub> does not form at equilibrium, rather, Burtovyy and Tkacz [9] inferred that the presence of small crystallites from the dehydrogenated copper hydride seems required for nucleation.

(ii) At  $P > 18$  GPa and room  $T$ , trigonal Cu<sub>2</sub>H with the anti-CdI<sub>2</sub> structure was synthesized and found stable up to 50 GPa [10]. Donnerer *et al.* [10] also observed an *fcc*-based copper hydride after decompression of trigo-

nal Cu<sub>2</sub>H and recompression to 12.5 GPa, with a reported composition of CuH<sub>0.15</sub>, a significantly lower degree of hydrogenation.

(iii) Laser heating of pure copper grains with excess hydrogen resulted in the formation of Cu<sub>2</sub>H at  $\sim 30$  GPa, and CuH<sub>0.65</sub> at  $\sim 50$  GPa [11] (cubic with an *fcc* arrangement of Cu atoms), the group 11 metal hydride with the highest documented hydrogen content at high  $P$  found to this day.

Experimental probes in the DAC, the most important device used to generate high  $P$  in solid state research of novel hydrides, have not been able to directly investigate electronic and dynamic properties of the hydrogen sublattice until recently. By combining magnetic flux tailoring techniques [12–14] and a modified DAC design [18,26], the accessible  $P$ -range for <sup>1</sup>H Nuclear Magnetic Resonance (NMR) spectroscopy in the DAC was recently extended from  $P < 10$  GPa [17,18] to beyond 100 GPa [15,19].

A  $P$ -induced enhancement of H-H interaction in iron monohydride (FeH) – documented by an increased electron density of states at the Fermi level for the hydrogen 1s state ( $N_{\text{H-1s}}(E_F)$ ) – was described recently by our group [15] employing <sup>1</sup>H-NMR spectroscopy in combination with electronic structure calculations, which was accompanied by the formation of a sublattice of increased electron localisation connecting the hydrogen positions. However, similar studies have not yet been conducted for comparable metal hydrides to test the generality of such features. Here, we present results on copper hydrides using a combination of powder and single crystal synchrotron X-ray diffraction (XRD), *in-situ* high- $P$  <sup>1</sup>H-NMR spectroscopy, and density functional theory (DFT) based computations, which enabled us to

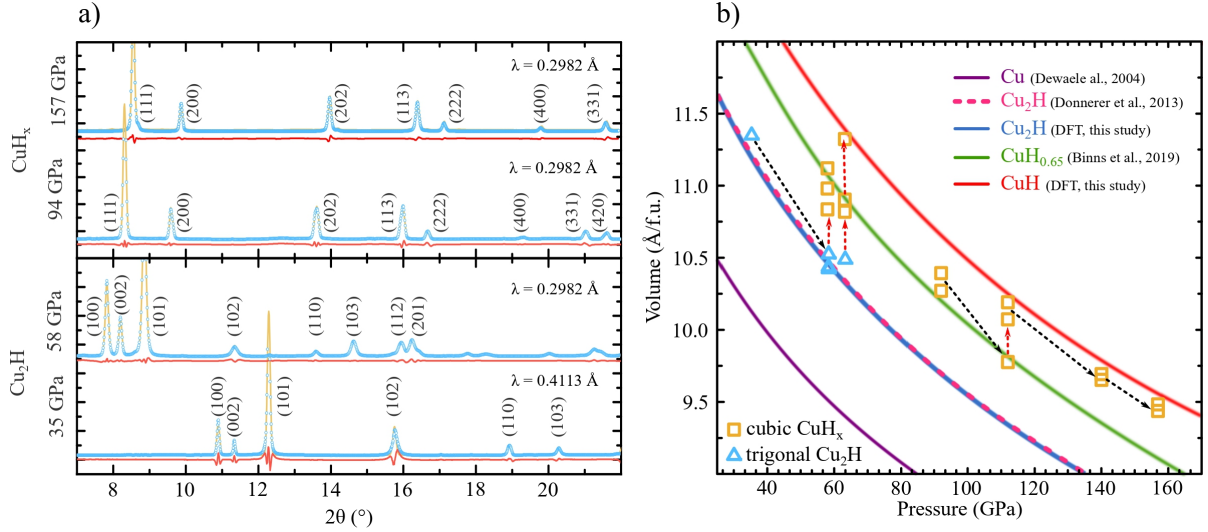


Figure 1: a) Examples of powder X-ray diffraction patterns of  $\text{Cu}_2\text{H}$  and  $\text{CuH}_x$  synthesized at different pressures; yellow lines are Rietveld fits to the experimental data (blue dots); red lines denote the residuals. Indexed peaks are for the  $P\bar{3}m1$   $\text{Cu}_2\text{H}$  and  $Fm\bar{3}m$   $\text{CuH}_x$  structures. b) Equations-of-state of the copper hydride phases and pure Cu: the equations-of-state for pure copper [41] and  $\text{CuH}_{0.65}$  [11] are shown in purple and green, respectively. The pink dashed line denotes the equation-of-state for  $P\bar{3}m1$   $\text{Cu}_2\text{H}$  [10]. The results of a third order Birch-Murnaghan fit to the DFT ground-state energies are shown by a blue curve for  $\text{Cu}_2\text{H}$  and in red for  $\text{CuH}$ . The equation-of-state parameters can be found in Table S1 in the Supplemental Material. Open orange squares ( $\text{CuH}_x$ ) and blue triangles ( $\text{Cu}_2\text{H}$ ) represent diffraction data, and the arrows illustrate the experimental pathways of heating (red) and compression (black).

establish their structural and electronic properties, and determine  $^1\text{H}$  mobility, and quantitatively compare to results for FeH [15].

## II. Methods

In this work,  $\text{CuH}_x$  compounds were synthesized by direct reaction of pure copper and paraffin in the laser-heated DAC [15,20]. Gaskets were manufactured by pre-indenting a 250  $\mu\text{m}$  thick rhenium foil to  $\sim 25$  and  $\sim 15$   $\mu\text{m}$ , respectively, and the hole for the sample chamber was laser drilled in the center of the flat indentation. All cells were loaded with paraffin oil (Sigma Aldrich Ltd.), serving as hydrogen reservoir, NMR reference signal and  $P$ -transmitting medium. High-quality copper powder (5N purity) was added with an estimated volume ratio of 1:10 to 1:15, in order to ensure hydrogen excess. The reaction of copper with paraffin was conducted at varying  $P$  by first compressing the DAC and then using double-sided laser heating in continuous wave mode with a nominal laser power of about 25-40 W to create  $T$  in excess of 2000 K.

### A. X-ray diffraction

Two DACs with culets of 250  $\mu\text{m}$  and 120  $\mu\text{m}$  in diameter were used for XRD experiments. Reaction of paraffin oil during laser-heating with copper was confirmed by a change in optical properties of the sample and by

the appearance of the Raman peak of micro-diamonds formed from the carbon in the paraffin oil. Pressure inside the DAC was determined using the equations-of-state of unreacted copper, the rhenium gasket material and the micro-diamonds;  $P$  estimated from the Raman shift of micro-diamonds [21] was consistent with that obtained from the diamond edge of the anvils used for  $P$ -determination in the NMR experiments. Temperature was determined by multiwavelength spectroradiometry.

High-resolution XRD measurements were performed at beamlines ID15 of the European Synchrotron Radiation Facility (ESRF) in Grenoble, France, and P02.2 of Petra III (DESY) in Hamburg, Germany. At beamline ID15, an X-ray beam of 30.142 keV (0.41134  $\text{\AA}$ ) and a large-area MAR555 flat panel detector were used. At beamline P02.2, an X-ray beam of 42.87 keV (0.2982  $\text{\AA}$ ) and a Perkin Elmer XRD1621 flat panel detector were used.

Phase identification was carried out based on powder diffraction patterns integrated from still and wide-scan images, using the DIOPTAS software [22]. Cell parameters were determined from LeBail refinement of selected powder diffraction patterns using JANA2006 [23]. A background correction was applied manually or by a Chebyshev polynomial, and peaks were fitted with pseudo-Voigt functions.

Single-crystal X-ray diffraction data was collected under cell rotation between  $-35^\circ$  and  $35^\circ$  to improve con-

straints on crystal symmetry. The data was analyzed using CrysAlisPro, including integration of intensities, frame scaling and empirical absorption corrections. Structural solutions and refinements were performed using the ShelX package [24,25] in the WinGX software [26].

## B. Nuclear Magnetic Resonance Measurements

Four DACs for NMR measurements were prepared following the procedure described previously [18,26]. Diamond anvils with pairs of 250  $\mu\text{m}$  and 100  $\mu\text{m}$  culets were covered with a 1  $\mu\text{m}$  layer of copper using physical vapor deposition. By focused ion beam milling, Lenz lens structures were cut from the copper layer to form a double- and triple-stage NMR resonator setup for the 250  $\mu\text{m}$  and 100  $\mu\text{m}$  anvils, respectively. To insure insulation between the resonators and the metallic gasket, the latter was covered by 500 nm of  $\text{Al}_2\text{O}_3$  using chemical vapor deposition. Helmholtz excitation coils were manufactured from 80  $\mu\text{m}$  thick PTFE (Teflon) insulated copper wire consisting of 4 to 5 turns with an inner diameter of  $\sim 3$  mm. Both coils were fixed onto the diamond backing plates such that the copper coated anvils are at the coils' center. After cell loading and closure, the excitation coils were connected to form a Helmholtz coil-like arrangement.

The NMR cells were inserted into a standard in-house built NMR probe for use with a magnetic field of  $\sim 1030$  mT generated by an electron spin resonance magnet, corresponding to a resonance frequency ( $\omega_0$ ) of the hydrogen nuclei of 43.851 MHz. In order to limit radio frequency excitation to a region of interest of  $\sim 2000$  ppm (90 kHz at 1030 mT), we recorded high- $P$   $^1\text{H}$ -NMR spectra using amplitude-modulated band-selective pulses with uniform response and pure phase (E-BURP) [27]. Relaxation times ( $T_1$ ) were obtained using an I-BURP/E-BURP inversion recovery sequence.  $^1\text{H}$ -NMR spectra were found broadened (Figure S1 in the Supplemental Material) by pronounced Knight shift anisotropies ( $\Delta K$ ).

In order to extract the isotropic values of the Knight shift ( $K_H$ ), we developed a Python script for line-shape simulations adopted to the special experimental needs of high- $P$  NMR. Simulation of the NMR line-shapes (exemplary shown in Figure S2 in the Supplemental Material) was carried out following [28–30]. We used the standard expression for the resonance frequency distribution  $\omega$  for a given  $\Delta K$  and  $K_H$ ,

$$\omega(\alpha, \beta) = \omega_0 K_H + \Delta K \cdot \left( \frac{3\cos^2\beta - 1}{2} + \frac{\eta}{2} \sin^2\beta \cos(2\alpha) \right), \quad (1)$$

where the Euler angles  $\alpha$  and  $\beta$  describe the orientation of the crystallites with respect to the external magnetic field  $B_0$ .

We used the Haerberlein convention for the NMR shift tensor [31],

$$\begin{aligned} \Delta K &= K_{zz} - \frac{K_{xx} + K_{yy}}{2}, \quad (2) \\ K_H &= \frac{K_{xx} + K_{yy} + K_{zz}}{3}, \quad (3) \\ \eta &= \frac{K_{yy} - K_{xx}}{K_{zz}} \text{ with } |K_{zz}| > |K_{xx}| > |K_{yy}|. \quad (4) \end{aligned}$$

The asymmetry parameter  $\eta$  accounts for the deviation from sphericity of the Knight shift tensor  $K$ .

The line-shape function used to fit the spectra is

$$P(\omega) = \int_{-1}^1 \frac{\mu}{4\pi} \sin(\beta(\omega, \alpha)) \left| \frac{\partial \beta(\omega, \alpha)}{\partial \omega} \right| d(\cos(2\alpha)), \quad (5)$$

where  $\beta(\omega, \alpha)$  is the inverse function of equation (1) with respect to  $\beta$ , and  $\mu$  accounts for the multiplicity of spectral functions. In order to obtain  $K_H$ , we calculated  $P(\omega)$  for given  $\omega_0$ , and optimized with respect to the experimental data by varying  $\Delta K$ ,  $K_H$  and  $\eta$  (Figure S3 in the Supplemental Material).

## C. Density Functional Theory Calculations

All electronic structure calculations were performed with Quantum Espresso [32,33] with the projector augmented wave (PAW) approach [34]. We used the generalized gradient approximation by Perdew-Burke-Ernzerhofer (PBE) [35] to exchange and correlation with the corresponding PAW-PBE potential files. For both Fe and Cu, a valence electron configuration that includes electronic states 3s and higher is applied, appropriate to extreme  $P$  [36]. Convergence tests for static electronic structure simulations led to a cutoff energy for the plane-wave expansion of 170 Ry (Cu) and 120 Ry (Fe) and to reciprocal space sampling with a Monkhorst-Pack [38] grid of 32x32x32. In addition to the total electronic density-of-states (DOS), site and orbital projections were computed (Figure S4 in the Supplemental Material), with particular attention to the crystal field splitting of the 3d electronic states. Equations-of-state of CuH and CuH<sub>2</sub> were fitted based on the ground state energies for various unit cell volumes ( $V$ ) using a Birch-Murnaghan formulation [38]. Fit parameters are summarized in Table S1 of the Supplemental Material.

Molecular dynamics (MD) simulations were performed for cells of 54 and 96 atoms for Cu<sub>2</sub>H and FeH, respectively, with a Monkhorst-Pack [37] grid of 2x2x2. Calculations were performed in the canonical ensemble, and  $T$  was controlled by an Anderson thermostat [39].

We employed a timestep of 0.1 fs to account for the fast hydrogen dynamics [40] and ran the simulations for a duration of 1.6 ps. Diffusion coefficients were calculated from the mean square displacements obtained via MD trajectories (Figure S5 in the Supplemental Material).

### III. Results and Discussion

#### A. Structure and Composition of Cu-Hydrides

After laser heating at  $P=35$  GPa, a trigonal  $\text{Cu}_2\text{H}$  compound (space group  $P\bar{3}m1$ ) formed, as determined by powder (Figure 1a, Table S2 in the Supplemental Material) and single crystal diffraction (Tables S3 and S4 in the Supplemental Material). The trigonal symmetry of  $\text{Cu}_2\text{H}$  is based on a distorted hexagonal structure, with *hcp*-forbidden peaks present (e.g., 001, 003). This phase remained stable under compression to at least  $P=90$  GPa at room  $T$ . At  $P=35$  and 58 GPa, its atomic volumes (per Cu atom,  $V/\text{Cu}$ ) are 11.27(2) and 10.44(1)  $\text{\AA}^3$ , in agreement with values expected from the equations-of-state previously reported from experiments [10] and computed here (Figure 1b).

Laser heating of  $\text{Cu}_2\text{H}$  or pristine copper with paraffin at  $P>50$  GPa resulted, in agreement with previous observations [11], in the formation of a cubic phase with an *fcc* arrangement of Cu atoms. The same phase has been found stable upon laser heating of the sample up to  $P\approx 160$  GPa, the highest  $P$  reached in this study. Its  $V/\text{Cu}$  at  $P=58, 94,$  and 112 GPa (11.11(2), 10.27(4), 9.80(6)  $\text{\AA}^3$ ) agree with those derived from the equation-of-state of *fcc*-structured  $\text{CuH}_{0.65}$  [11] (Figure 1b).

After repeated heating and  $T$ -quench of the cubic phase at  $P\geq 110$  GPa, an increase of  $V/\text{Cu}$  was observed (Figure 1b) and values eventually became larger than expected for previously reported copper hydrides: at  $P=157$  GPa, for example,  $V/\text{Cu}$  reaches 9.48(2)  $\text{\AA}^3$  vs. 9.03  $\text{\AA}^3$  for  $\text{CuH}_{0.65}$  [11] and 7.79  $\text{\AA}^3$  for Cu [41] based on the reported equations-of-state. Thus, our data suggest that at  $P\geq 110$  GPa, we synthesized a copper hydride with a larger hydrogen content than previously reported at high  $P$  [10,11].

An exact determination of the hydrogen content of Cu-compounds formed in different experiments is difficult, but we note that the DFT-based results reproduce the experimental equation-of-state for trigonal  $\text{Cu}_2\text{H}$  well (Figure 1b). The experimental data compares similarly well with the DFT-based calculations on the equation-of-state for NaCl-structured CuH (Figure 1b), and we therefore infer that the cubic copper hydride we synthesized at high  $P$  under  $T$ -cycling has a ratio of Cu/H=1 (CuH), (Table S1 in the Supplemental Material). Laser heating at  $P=140$  GPa produced no further increase in  $V$

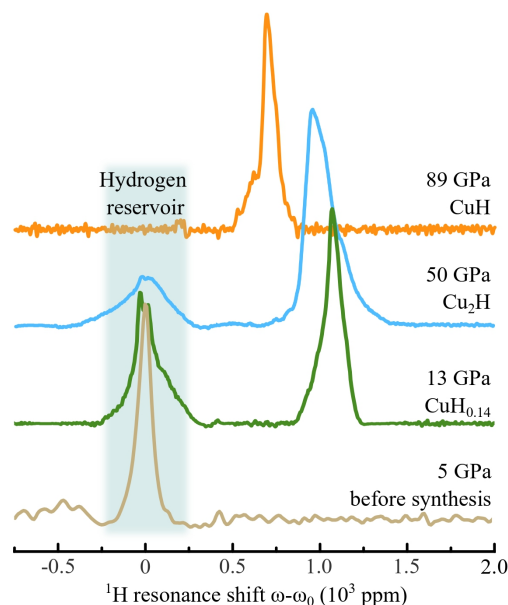


Figure 2: Representative  $^1\text{H}$ -NMR spectra of copper hydrides,  $\text{CuH}$ ,  $\text{Cu}_2\text{H}$ , and  $\text{CuH}_{0.15}$ , formed after laser heating of copper-paraffin loaded cells at 89 GPa and 50 GPa, and on decompression at 13 GPa.

for CuH, implying that either the H reservoir was exhausted or that the Cu hydride reached its maximum H storing capacity.

#### B. NMR Data and Interpretation

The chemical compositions of copper hydrides and their respective stability fields provide the basis for the discussion and interpretation of  $^1\text{H}$ -NMR data. Figure 2 shows representative  $^1\text{H}$ -NMR spectra of the copper hydrides at different pressures (*cf.* Figure S1 in the Supplemental Material for all  $^1\text{H}$ -NMR spectra). The NMR signal from the copper-paraffin sample ( $P=5$  GPa before heating) originates solely from the paraffin reservoir, and both the full width at half maximum (FWHM) of the NMR signal and the relaxation rate agree well with previous studies [14,15]. As  $\omega_0$  of the paraffin reservoir does not change considerably with  $P$  (Figure 2), it was used as a reference. Additional signals appeared after laser heating at  $P=50$  and 89 GPa, assigned to  $\text{Cu}_2\text{H}$  and CuH, respectively. During decompression of  $\text{Cu}_2\text{H}$  to  $P\leq 16$  GPa, the spectrum was interpreted as that of  $\text{CuH}_{0.15}$ , given the agreement in terms of transition  $P$  with previous experimental work [10,42]. The successive decrease of the resonance shift with increasing amount of hydrogen is in agreement with other metal hydrides synthesized at ambient  $P$  [43–47].

Figure 3a shows the relative changes of  $K_{\text{H}}$  as a function of compression  $V/V_0$  for the three copper hydrides synthesized, CuH,  $\text{Cu}_2\text{H}$ , and  $\text{CuH}_{0.15}$  (for  $K_{\text{H}}$  as a function of the hydrogen-hydrogen distances  $r_{\text{HH}}$ , see Figure

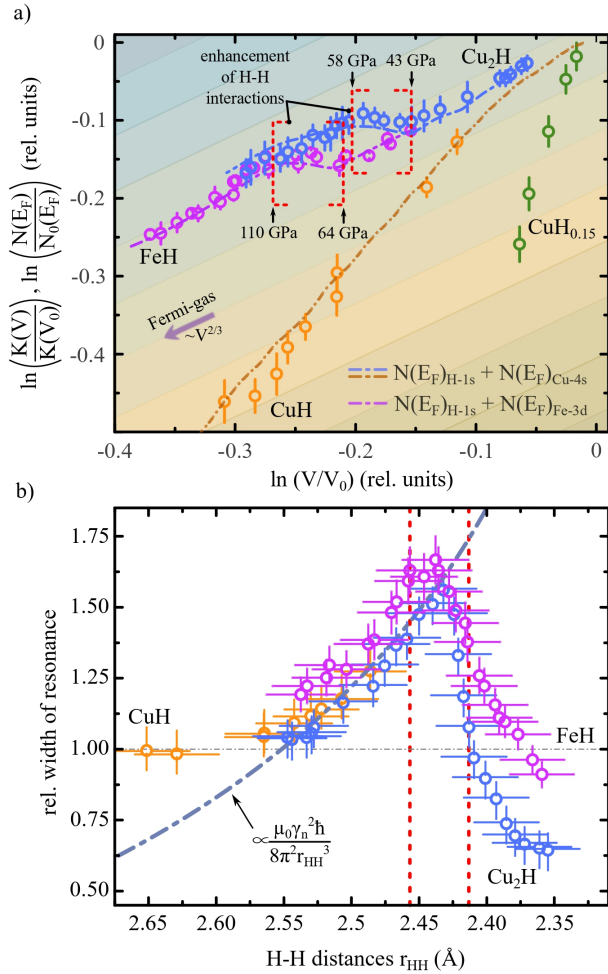


Figure 3: Comparison of experimental NMR data and DFT-based electronic structure calculations. a) Double logarithmic power plot of relative changes in the NMR Knight shift  $K_H(V)$  and the electron density-of-states at the Fermi energy  $N(E_F)$  as a function of compression. Experimental data (blue, magenta, orange and green) are normalized to  $K_H(V_0)$  using  $V_0$  from the respective equation-of-state from Tkacz et al. [42] (CuH<sub>0.15</sub>) and DFT computations from this study (CuH and Cu<sub>2</sub>H) (Table S1 in the Supplemental Material); The blue, magenta and orange dashed lines (splines through computed values) show the respective volume dependence of  $N(E_F)$ . Diagonal color stripes are guides to the eye representing a  $\propto V^{2/3}$  scaling for free-electron Fermi-gas-like behavior [15]. Black arrows denote respective pressures points. Data and results for FeH were taken from our previous work [15]. b) Relative FWHM line-widths of <sup>1</sup>H-NMR spectra as a function of the H-H distance  $r_{HH}$  for CuH, Cu<sub>2</sub>H, and FeH. The dotted blue line depicts the theoretical line-width dependence for pure dipolar broadening and vertical red dashed lines show the  $r_{HH}$  corresponding to the pressure intervals marked by the arrows in a).

S3 a) in the Supplemental Material), as well as for cubic FeH from our previous work [15]. Cu<sub>2</sub>H and FeH follow a slope expected for a free electron gas-like system ( $K_H \propto V^{2/3}$  [15]), while both CuH<sub>0.15</sub> and CuH violate Fermi gas ideality, indicating that these phases might at

best be considered as bad metals or semi-metals, in agreement with recent DFT calculations [48].

The  $V$ -dependence of  $K_H$  for Cu<sub>2</sub>H displays a deviation from free electron gas behavior for  $43 \text{ GPa} \lesssim P \lesssim 58 \text{ GPa}$ , similar to FeH for  $64 \text{ GPa} \lesssim P \lesssim 110 \text{ GPa}$  [15]. This effect can also be seen in the dependence of the electronic DOS at the Fermi energy  $N(E_F)$  from the DFT-simulations, consisting of the sum of the 4s electron DOS of Cu and the 1s electron DOS of H (Figure 3a). Interestingly, the contribution of the hydrogen 1s electron to  $N(E_F)$  for Cu<sub>2</sub>H and FeH (Figure 4a) gradually increases with decreasing distance between hydrogens ( $r_{HH}$ ) (Figure S4 in the Supplemental Material), similar to the total DOS (Figure 3a). This observation suggests that conduction electron density from the uncompensated 4s states in Cu<sub>2</sub>H or the uncompensated 3d- $t_{2g}$  states in FeH [15] is transferred to  $M_{H-1s}(E_F)$ , respectively. By contrast,  $M_{H-1s}(E_F)$  of semi-metallic CuH shows a strongly negative slope (Figure 4a). Given the striking similarity of the observed behavior in  $K_H$  and  $N(E_F)$  for Cu<sub>2</sub>H with that of FeH [15], we infer that they can be explained by the same  $P$ -induced formation of a sublattice of increased electron localization connecting the hydrogen positions accompanied by an increasing  $M_{H-1s}(E_F)$  in trigonal Cu<sub>2</sub>H at  $P \gtrsim 40 \text{ GPa}$ .

Figure 3b shows the dependence of the relative proton NMR resonance line-widths on  $r_{HH}$  in both metallic phases, Cu<sub>2</sub>H and FeH, and in semi-metallic CuH. For  $r_{HH} > 2.45 \text{ \AA}$  ( $P=43 \text{ GPa}$  for Cu<sub>2</sub>H and  $P=64 \text{ GPa}$  for FeH), line-widths of the NMR signals for both transition metal hydrides and semi-metallic CuH increase with  $P$  due to dipolar coupling of hydrogen spin-1/2 nuclei, indicated by a  $\Delta\omega \propto r_{HH}^{-3}$  slope [49,50]. At higher  $P$ , i.e.,  $r_{HH} < 2.45 \text{ \AA}$ , the NMR absorption line-widths for Cu<sub>2</sub>H (Figure S1 in the Supplemental Material) and FeH decrease significantly. Values of  $\Delta K$  and  $\eta$  for Cu<sub>2</sub>H from spectral simulations were found to be almost pressure independent at  $r_{HH} > 2.45 \text{ \AA}$ . For smaller  $r_{HH}$  (i.e., at higher  $P$ ),  $\Delta K$  decreases abruptly and  $\eta \approx 0.0$  (Figure S3 in the Supplemental Material), and spectra approach a Voigtian line shape (Figure S1 in the Supplemental Material) which we attributed to the modification of electronic structure in Cu<sub>2</sub>H at similar  $r_{HH}$  as previously reported for FeH [15].

The deviation of  $K_H$  from a Fermi-gas like behavior can be estimated via the Korringa ratio ( $K_H^2 T / R_1$ , with the relaxation rate  $R_1 = 1/T_1$ ), normalized with its free electron gas equivalent [51,52],  $\frac{h}{8\pi^2 k_B T} \left(\frac{\gamma_e}{\gamma_n}\right)^2$ , where  $k_B$  is the Boltzmann and  $h$  Planck's constant,  $\gamma_e$  and  $\gamma_n$  are the gyromagnetic ratios of the electron and the hydrogen nucleus, respectively. We find this ratio to be larger than one for  $r_{HH} \gtrsim 2.45 \text{ \AA}$ , indicating significant electron-

electron correlation for both FeH and Cu<sub>2</sub>H. For smaller  $r_{\text{HH}}$  the ratio approaches unity (Figure S6 in the Supplemental Material); this finding suggests that enhanced Fermi contact hyperfine interactions dominate the electronic structure at high  $P$ .

Since diffraction data and computational results on Cu<sub>2</sub>H (this study) and FeH [15,20] do not show signs of structural transitions within the experimental  $P$ -range, line narrowing effects cannot be related to atomic rearrangements. Rather, line-width changes for two different transition metal hydrides at comparable  $r_{\text{HH}}$  suggest that electronic and dynamic effects on the hydrogen spin system must be considered.

### C. Proton Diffusivities

Hydrogen spin-lattice relaxation rates  $R_1$  in metal hydrides originate from two mechanisms, representing electronic hyperfine interactions  $R_1^e$  and proton diffusion  $R_1^d$  [53]:

(i)  $R_1^e$  of hydrogen nuclei – from the interaction with conduction electron spins – can be calculated by a Korringa-like behavior for a Fermi-gas [51,52] with

$$K_{\text{H}}^2 = \frac{h}{8\pi^2 k_{\text{BT}}} \left( \frac{\gamma_e}{\gamma_{\text{H}}} \right)^2 R_1^e, \quad (6)$$

as described above.  $K_{\text{H}}$  originates from contact hyperfine interaction between the hydrogen 1s electron orbital and the proton via

$$K_{\text{H}} = \frac{2\mu_0 \mu_{\text{B}}}{A} H_{\text{hf}}^s N(E_{\text{F}}), \quad (7)$$

with  $\mu_0$  the permeability of free space,  $A$  Avogadro's number,  $\mu_{\text{B}}$  the Bohr magneton, and  $H_{\text{hf}}^s$  the hyperfine field [15].

(ii) A modulation of the relaxation rate – from the diffusive motion of hydrogen nuclei ( $R_1^d$ ) in crystalline systems – can be expected to be well described by the theory of Bloembergen, Pound and Purcell [54] by the use of a single correlation time for a stochastic undirected motion of hydrogen atoms as

$$R_1^d = \frac{3\pi}{10} \frac{\gamma_{\text{H}}^4 h^2 N_0}{aD}, \quad (8)$$

where  $N_0$  is the number density of atoms,  $D$  the hydrogen diffusion coefficient, and  $a$  the distance of closest approach which is at the order of  $r_{\text{HH}}$ .

Calculating the relaxation rate  $R_1$  (Figure S6 in the Supplemental Material) in the extreme narrowing limit [49], i.e.,  $R_1 = R_1^e + R_1^d$ , from the experimental line-widths via the relationship  $R_1 \approx \pi \cdot \Delta\omega$  and subtracting the conduction electron contribution  $R_1^e$  calculated via equation (6) gives access to  $D$  of the protons in transition metal hydrides at high  $P$ , following early work at ambient  $P$  [55,56]. Figure 4b shows experimentally

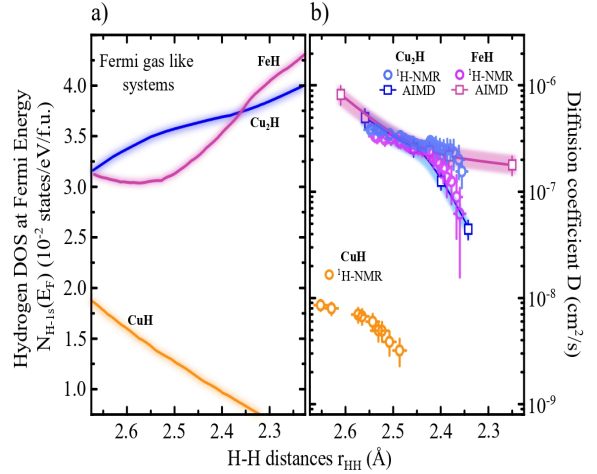


Figure 4: Comparison of electronic structure and proton diffusivities. a) Hydrogen 1-s electron density-of-state contribution  $N_{\text{H-1s}}(E_{\text{F}})$  for CuH, Cu<sub>2</sub>H and FeH as a function of the H-H distance in the structures (pressure increasing to the right). b) Proton diffusion coefficients extracted from NMR data (blue, purple and orange circles) and computed via DFT-based molecular dynamics simulations (blue and magenta squares and lines) for metallic Cu<sub>2</sub>H and FeH, and the semimetal CuH. The values fall into two groups: (i) high  $N_{\text{H-1s}}(E_{\text{F}})$  values and high diffusivity for the metallic compounds and (ii) small  $N_{\text{H-1s}}(E_{\text{F}})$  values accompanied by a smaller diffusion coefficient in CuH.

derived and computed  $D$  as a function of  $r_{\text{HH}}$  for Cu<sub>2</sub>H, FeH, and semi-metallic CuH.

Values for  $D$  decrease from  $D_{\text{Cu}_2\text{H}} \sim 3.8(4) \cdot 10^{-7}$  cm<sup>2</sup>/s at 15 GPa and  $D_{\text{FeH}} \sim 3.3(6) \cdot 10^{-7}$  cm<sup>2</sup>/s at 33 GPa to  $D_{\text{Cu}_2\text{H}} \sim 1.6(9) \cdot 10^{-7}$  cm<sup>2</sup>/s and  $D_{\text{FeH}} \sim 0.8(9) \cdot 10^{-7}$  cm<sup>2</sup>/s at 96 and 202 GPa, respectively. A steeper slope of  $D$  for  $r_{\text{HH}} < 2.42$  Å coincides with a decrease in spin-lattice relaxation time  $T_1$  for  $V/V_0 \lesssim 0.8$ , observed in both Cu<sub>2</sub>H (Figure S3 in the Supplemental Material) and FeH. Proton diffusivity in CuH was found approximately two orders of magnitude smaller than that for Cu<sub>2</sub>H. Hydrogen diffusion coefficients calculated from DFT molecular dynamics simulations (Figures 4b and S5 in the Supplemental Material) agree with our <sup>1</sup>H-NMR derived results. The correlation between an increased density-of-states at  $E_{\text{F}}$  and high values of  $D$  in the metallic hydrides, Cu<sub>2</sub>H and FeH, support a causal relation.

Proton mobility investigated in other metal hydride systems by means of standard as well as pulsed-field gradient NMR typically found  $D$  in the range  $10^{-13}$ - $10^{-7}$  cm<sup>2</sup>/s [53,57–59]. Diffusivities for Cu<sub>2</sub>H and FeH are at the upper limit of this broad range, suggesting that proton self-diffusion plays a more significant role in high- $P$  metal hydrides than in hydrides stabilized at ambient conditions. Given the fact that comparable metal hydrides, such as TiH<sub>1.66</sub> [59] and VH<sub>0.39-0.85</sub> [55], show significantly lower  $D$ -values for the protons in the range

$10^{-13}$ - $10^{-10}$  cm<sup>2</sup>/s at larger  $r_{\text{HH}}$ , it stands to reason that proton self-diffusion in H-rich polyhydrides, such as LaH<sub>10</sub>, YH<sub>10</sub> or CaH<sub>6</sub> with  $r_{\text{HH}} < 1.2$  Å [60–62], approaches values several orders of magnitude larger than for Cu<sub>2</sub>H and FeH. Recent computational results [63,64] suggest that atomic quantum fluctuations and significant hydrogen zero-point energies strongly influence the high- $P$  stability of these H-rich polyhydrides. Thus, *ab-initio* computations on diffusivity including nuclear quantum effects would shed further light on these phenomena.

#### IV. Conclusion

In this work, three stable copper hydride phases of varying hydrogen content (CuH<sub>0.15</sub>, Cu<sub>2</sub>H and CuH) were synthesized at high pressure in the diamond anvil cell. For Cu<sub>2</sub>H, we found an ideal metallic trend in the <sup>1</sup>H-NMR Knight shift, with an unexpected change in slope in a pressure-range of 43-58 GPa, associated with an increase of conduction electron density-of-states at the Fermi energy of the hydrogens 1s electron orbitals, similar to our earlier observations in metallic FeH [18]. For FeH, the increase was observed at  $P = 64$ -110 GPa and found to be correlated with the formation of a sublattice of increased electron density between the hydrogen atoms, intercalating the metal host lattice.

A line-shape and relaxation-rate analysis of the NMR spectra revealed, in agreement with molecular dynamics simulations, a significantly increased diffusivity of protons in the metallic hydride compounds (Cu<sub>2</sub>H and FeH), in contrast to the semi-metallic CuH with proton diffusivity two orders of magnitude slower, accompanied by a significantly smaller electron density-of-states at the Fermi energy. Correlating these effects with the average H-H distances, we find that in both metallic hydride compounds hydrogen-interactions significantly increase

at almost identical  $r_{\text{HH}} \approx 2.45$  Å, implying that the observed high diffusivities may only weakly depend on the host transition metal ions. This insight may provide an important step in the future search and design of novel hydride-based superconductors at high pressure for which a H-sublattice of increased electron density was predicted to be a requirement for high-temperature superconductivity [60].

#### Acknowledgements

We thank Nobuyoshi Miyajima for help with the FIB milling. The authors thank the German Research Foundation (Deutsche Forschungsgemeinschaft, DFG, Project Nos. DU 954/11-1, DU 393/13-1, DU 393/9-2, ME 5206/3-1, and STE 1105/13-1 in the research unit FOR 2440) and the Federal Ministry of Education and Research, Germany (BMBF, Grant No. 05K19WC1) for financial support. D.L. thanks the Alexander von Humboldt Foundation for financial support. N.D. thanks the Swedish Government Strategic Research Area in Materials Science on Functional Materials at Linköping University (Faculty Grant SFO-Mat-LiU No. 2009 00971).

#### Author Contributions:

T.M. and F.T. contributed equally to this study. T.M. and L.D. designed the experiments. T.M., L.D., S.K. and D.L. prepared all diamond anvil cells. G.C., D.L., E.K., T.F., K.G., M.H., M.B. and L.D. performed the diffraction, T.M. and G.C. the NMR experiments. F.T. and G.S.N. designed and conducted the electronic structure and molecular dynamics calculations. T.M. and F.T. analyzed NMR and XRD data and computational results. T.M., G.S.N., F.T., L.D., and N.D. assessed all data and wrote the manuscript.

#### References:

- [1] A. Wurtz, CR Hebd. Seances Acad. Sci **18**, 702 (1844).
- [2] R. Mohtadi and S. Orimo, Nat. Rev. Mater. **2**, 16091 (2017).
- [3] A. P. Drozdov, M. I. Erements, I. A. Troyan, V. Ksenofontov, and S. I. Shylin, Nature **525**, 73 (2015).
- [4] M. Somayazulu, M. Ahart, A. K. Mishra, Z. M. Geballe, M. Baldini, Y. Meng, V. V. Struzhkin, and R. J. Hemley, Phys. Rev. Lett. **122**, 027001 (2019).
- [5] A. P. Drozdov, P. P. Kong, V. S. Minkov, S. P. Besedin, M. A. Kuzovnikov, S. Mozaffari, L. Balicas, F. F. Balakirev, D. E. Graf, V. B. Prakapenka, E. Greenberg, D. A. Knyazev, M. Tkacz, and M. I. Erements, Nature **569**, 528 (2019).
- [6] E. Zurek, R. Hoffmann, N. W. Ashcroft, A. R. Oganov, and A. O. Lyakhov, Proc. Natl. Acad. Sci. **106**, 17640 (2009).
- [7] R. T. Howie, O. Narygina, C. L. Guillaume, S. Evans, and E. Gregoryanz, Phys. Rev. B **86**, 064108 (2012).
- [8] S. Aldridge and A. J. Downs, Chem. Rev. **101**, 3305 (2001).
- [9] R. Burtovyy and M. Tkacz, Solid State Commun. **131**, 169 (2004).
- [10] C. Donnerer, T. Scheler, and E. Gregoryanz, J. Chem. Phys. **138**, 134507 (2013).
- [11] J. Binns, M. Peña-Alvarez, M.-E. Donnelly, E. Gregoryanz, R. T. Howie, and P. Dalladay-Simpson, Engineering **5**, 505 (2019).
- [12] N. Spengler, J. Höfflin, A. Moazenzadeh, D. Mager, N. MacKinnon, V. Badilita, U. Wallrabe, and J. G. Korvink, PLoS One **11**, (2019).

- e0146384 (2016).
- [13] M. Jouda, R. Kamberger, J. Leupold, N. Spengler, J. Hennig, O. Gruschke, and J. G. Korvink, *Concepts Magn. Reson. Part B Magn. Reson. Eng.* **47B**, e21357 (2017).
- [14] T. Meier, N. Wang, D. Mager, J. G. Korvink, S. Petitgirard, and L. Dubrovinsky, *Sci. Adv.* **3**, eaa05242 (2017).
- [15] T. Meier, F. Trybel, S. Khandarkhaeva, G. Steinle-Neumann, S. Chariton, T. Fedotenko, S. Petitgirard, M. Hanfland, K. Glazyrin, N. Dubrovinskaia, and L. Dubrovinsky, *Phys. Rev. X* **9**, 031008 (2019).
- [16] T. Meier, S. Khandarkhaeva, J. Jacobs, N. Dubrovinskaia, and L. Dubrovinsky, *Appl. Phys. Lett.* **115**, 131903 (2019).
- [17] T. Meier, in *Annu. Reports NMR Spectrosc.*, edited by G. Webb, 93rd ed. (Elsevier, London, 2018), pp. 1–74.
- [18] T. Meier, *Prog. Nucl. Magn. Reson. Spectrosc.* **106–107**, 26 (2018).
- [19] T. Meier, S. Petitgirard, S. Khandarkhaeva, and L. Dubrovinsky, *Nat. Commun.* **9**, 2766 (2018).
- [20] O. Narygina, L. S. Dubrovinsky, C. A. McCammon, A. Kurnosov, I. Y. Kantor, V. B. Prakapenka, and N. A. Dubrovinskaia, *Earth Planet. Sci. Lett.* **307**, 409 (2011).
- [21] N. Dubrovinskaia, L. Dubrovinsky, R. Caracas, and M. Hanfland, *Appl. Phys. Lett.* **97**, 251903 (2010).
- [22] C. Prescher and V. B. Prakapenka, *High Press. Res.* **35**, 223 (2015).
- [23] V. Petříček, M. Dušek, and L. Palatinus, *Zeitschrift Fur Krist.* **229**, 345 (2014).
- [24] G. M. Sheldrick, *Acta Crystallogr. Sect. A Found. Crystallogr.* **64**, 112 (2007).
- [25] G. M. Sheldrick, *Acta Cryst* **71**, 3 (2015).
- [26] L. J. Farrugia, *J. Appl. Crystallogr.* **32**, 837 (1999).
- [27] H. Geen and R. Freeman, *J. Magn. Reson.* **93**, 93 (1991).
- [28] N. Bloembergen and T. J. J. Rowland, *Acta Metall.* **1**, 731 (1953).
- [29] G. E. Pake, *J. Chem. Phys.* **16**, 327 (1948).
- [30] C. E. Hughes and K. D. M. Harris, *Solid State Nucl. Magn. Reson.* **80**, 7 (2016).
- [31] R. K. Harris, E. D. Becker, S. M. Cabral de Menezes, P. Granger, R. E. Hoffman, and K. W. Zilm, *Pure Appl. Chem.* **80**, 59 (2008).
- [32] P. Giannozzi, S. Baroni, N. Bonini, M. Calandra, R. Car, C. Cavazzoni, D. Ceresoli, G. L. Chiarotti, M. Cococcioni, I. Dabo, A. Dal Corso, S. de Gironcoli, S. Fabris, G. Fratesi, R. Gebauer, U. Gerstmann, C. Gougoussis, A. Kokalj, M. Lazzeri, L. Martin-Samos, N. Marzari, F. Mauri, R. Mazzarello, S. Paolini, A. Pasquarello, L. Paulatto, C. Sbraccia, S. Scandolo, G. Sclauzero, A. P. Seitsonen, A. Smogunov, P. Umari, and R. M. Wentzcovitch, *J. Phys. Condens. Matter* **21**, 395502 (2009).
- [33] P. Giannozzi, O. Andreussi, T. Brumme, O. Bunau, M. Buongiorno Nardelli, M. Calandra, R. Car, C. Cavazzoni, D. Ceresoli, M. Cococcioni, N. Colonna, I. Carnimeo, A. Dal Corso, S. de Gironcoli, P. Delugas, R. A. DiStasio, A. Ferretti, A. Floris, G. Fratesi, G. Fugallo, R. Gebauer, U. Gerstmann, F. Giustino, T. Gorni, J. Jia, M. Kawamura, H.-Y. Ko, A. Kokalj, E. Küçükbenli, M. Lazzeri, M. Marsili, N. Marzari, F. Mauri, N. L. Nguyen, H.-V. Nguyen, A. Otero-de-la-Roza, L. Paulatto, S. Poncé, D. Rocca, R. Sabatini, B. Santra, M. Schlipf, A. P. Seitsonen, A. Smogunov, I. Timrov, T. Thonhauser, P. Umari, N. Vast, X. Wu, and S. Baroni, *J. Phys. Condens. Matter* **29**, 465901 (2017).
- [34] P. E. Blöchl, *Phys. Rev. B* **50**, 17953 (1994).
- [35] J. P. Perdew, K. Burke, and M. Ernzerhof, *Phys. Rev. Lett.* **77**, 3865 (1996).
- [36] T. Sjöstrom and S. Crockett, *Phys. Rev. E* **97**, 053209 (2018).
- [37] H. J. Monkhorst and J. D. Pack, *Phys. Rev. B* **13**, 5188 (1976).
- [38] R. E. Cohen, O. Gülseren, and R. J. Hemley, *Am. Mineral.* **85**, 338 (2000).
- [39] H. C. Andersen, *J. Chem. Phys.* **72**, 2384 (1980).
- [40] X. W. Zhou, T. W. Heo, B. C. Wood, V. Stavila, S. Kang, and M. D. Allendorf, *J. Appl. Phys.* **123**, 225105 (2018).
- [41] A. Dewaele, P. Loubeyre, and M. Mezouar, *Phys. Rev. B* **70**, 094112 (2004).
- [42] M. Tkacz, S. Majchrzak, and B. Baranowski, *Zeitschrift Für Phys. Chemie* **163**, 467 (1989).
- [43] R. Goring, R. Lukas, and K. Böhmhammel, *J. Phys. CSolid State Phys.* **14**, 5675 (1981).
- [44] D. S. Schreiber and R. M. Cotts, *Phys. Rev.* **131**, 1118 (1963).
- [45] D. S. Schreiber and L. D. Graham, *J. Chem. Phys.* **43**, 2573 (1965).
- [46] S. Kazama and Y. Fukai, *J. Phys. Soc. Japan* **42**, 119 (1977).
- [47] S. Kazama and Y. Fukai, *J. Less-Common Met.* **53**, 25 (1977).
- [48] X. H. Xiao, D. F. Duan, Y. Bin Ma, H. Xie, H. Song, D. Li, F. B. Tian, B. B. Liu, H. Y. Yu, and T. Cui, *Front. Phys.* **14**, 2 (2019).
- [49] W. S. Price, *Concepts Magn. Reson. Part A* **34A**, 60 (2009).
- [50] A. Abragam and L. C. Hebel, *Principles of*

- Nuclear Magnetism*, 18th ed. (Oxford University Press, Oxford New York, 1961).
- [51] J. Korrington, *Physica* **16**, 601 (1950).
- [52] W. Heitler and E. Teller, *Proc. R. Soc. A Math. Phys. Eng. Sci.* **155**, 629 (1936).
- [53] F. Kimmerle, G. Majer, U. Kaess, A. J. Maeland, M. S. Conradi, and A. F. McDowell, *J. Alloys Compd.* **264**, 63 (1998).
- [54] N. Bloembergen, E. M. Purcell, and R. V. Pound, *Phys. Rev.* **73**, 679 (1948).
- [55] R. C. Bowman, A. Attalla, and W. E. Tadlock, *Int. J. Hydrogen Energy* **1**, 421 (1977).
- [56] A. F. McDowell, C. F. Mendelsohn, M. S. Conradi, R. C. Bowman, and A. J. Maeland, *Phys. Rev. B* **51**, 6336 (1995).
- [57] R. C. Bowman, D. M. Gruen, and M. H. Mendelsohn, *Solid State Commun.* **32**, 501 (1979).
- [58] G. Majer, W. Renz, A. Seeger, R. G. Barnes, J. Shinar, and A. V. Skripov, *J. Alloys Compd.* **231**, 220 (1995).
- [59] H. Wipf, B. Kappesser, and R. Werner, *J. Alloys Compd.* **310**, 190 (2000).
- [60] F. Peng, Y. Sun, C. J. Pickard, R. J. Needs, Q. Wu, and Y. Ma, *Phys. Rev. Lett.* **119**, 107001 (2017).
- [61] Z. M. Geballe, H. Liu, A. K. Mishra, M. Ahart, M. Somayazulu, Y. Meng, M. Baldini, and R. J. Hemley, *Angew. Chemie - Int. Ed.* **57**, 688 (2018).
- [62] E. Zurek and T. Bi, *J. Chem. Phys.* **150**, 050901 (2019).
- [63] H. Liu, I. I. Naumov, Z. M. Geballe, M. Somayazulu, J. S. Tse, and R. J. Hemley, *Phys. Rev. B* **98**, 100102 (2018).
- [64] I. Errea, F. Belli, L. Monacelli, A. Sanna, T. Koretsune, T. Tadano, R. Bianco, M. Calandra, R. Arita, F. Mauri, and J. A. Flores-Livas, *Nature* **578**, 66 (2020).

## Proton Mobility in Metallic Copper Hydride from High Pressure Nuclear Magnetic Resonance Supplemental Material

Thomas Meier<sup>1\*</sup>, Florian Trybel<sup>1</sup>, Giacomo Criniti<sup>1</sup>, Dominique Laniel<sup>2</sup>, Saiana Khandarkhaeva<sup>1</sup>, Egor Koemets<sup>1</sup>, Timofey Fedotenko<sup>2</sup>, Konstantin Glazyrin<sup>3</sup>, Michael Hanfland<sup>4</sup>, Maxim Bykov<sup>5</sup>, Gerd Steinle-Nemann<sup>1</sup>, Natalia Dubrovinskaia<sup>2,6</sup> and Leonid Dubrovinsky<sup>1</sup>

<sup>1</sup>Bayerisches Geoinstitut, Universität Bayreuth, 95440 Bayreuth, Germany

<sup>2</sup>Material Physics and Technology at Extreme Conditions, Laboratory of Crystallography, Universität Bayreuth, 95440 Bayreuth, Germany

<sup>3</sup>Deutsches Elektronen-Synchrotron (DESY), 22603, Hamburg, Germany

<sup>4</sup>European Synchrotron Radiation Facility (ESRF), 38043 Grenoble Cedex, France

<sup>5</sup>Department of Mathematics, Howard University 2400 Sixth Street NW, Washington, DC 20059 (USA)

<sup>6</sup>Department of Physics, Chemistry and Biology (IFM), Linköping University, SE-581 83, Linköping, Sweden

[\\*thomas.meier@uni-bayreuth.de](mailto:thomas.meier@uni-bayreuth.de)

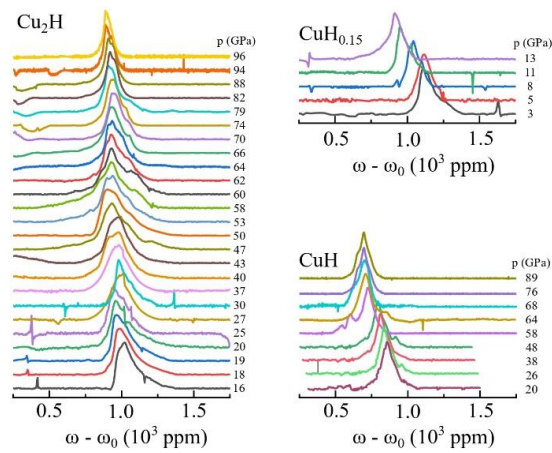


Figure S1: <sup>1</sup>H-NMR spectra of copper hydrides synthesized in this study.

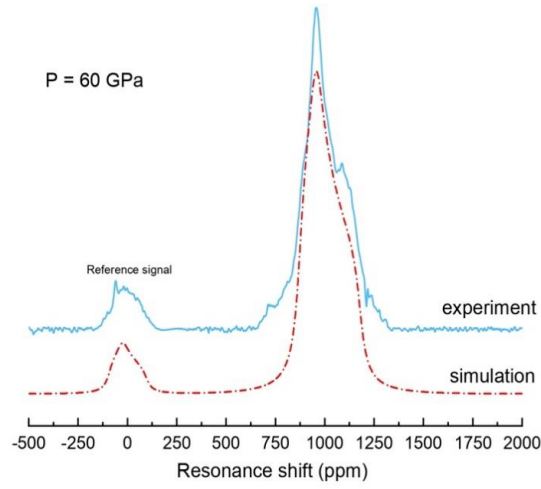


Figure S2: Exemplary comparison of measured and calculated NMR line shapes at 60 GPa. Both the reference signal from the Paraffin reservoir and the signal from the copper hydride phase are in good agreement with the simulated spectrum. Spectral broadening was accounted for by convoluting the total line shape function,  $P_{\text{tot}} = \sum_i P(\omega)_i$ , with a Voigt line of defined Lorentzian and Gaussian widths. In order to account for spectral line distortions due to limited radio-frequency excitation, we used a filter function of the form  $F(\omega_p, \tau_{RF}) = \frac{\sin((\omega_0 - \omega_p)\tau_{RF})}{(\omega_0 - \omega_p)\tau_{RF}}$ , where  $\omega_p$  is the carrier frequency of the radio frequency pulse,  $\omega_0$  the Larmor frequency of the respective NMR active nucleus at  $B_0$ ,  $\tau_{RF}$  the pulse length in the time domain and  $F(\omega_p, \tau_{RF})$  the Fourier transform of the rectangular excitation.

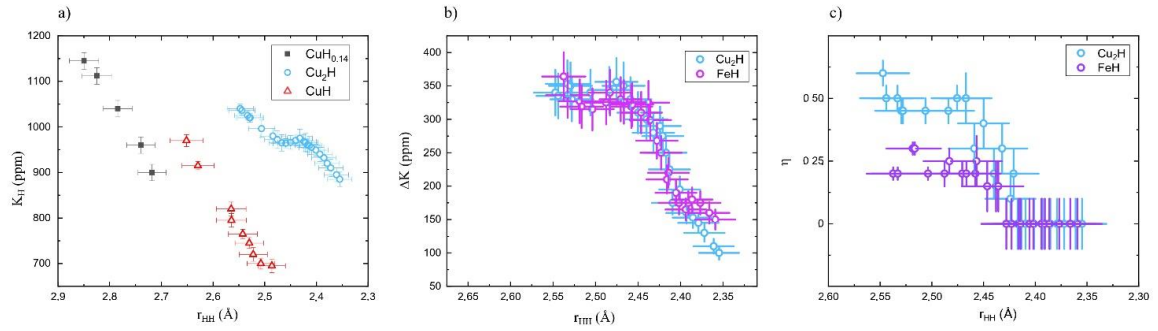


Figure S3: a) Knight shift  $K_H$  versus  $r_{HH}$  of the copper hydrides synthesized in this study, b) Knight shift anisotropy of  $\text{Cu}_2\text{H}$  and  $\text{FeH}$  and c) asymmetry parameter  $\eta$  of  $\text{Cu}_2\text{H}$  and  $\text{FeH}$ .

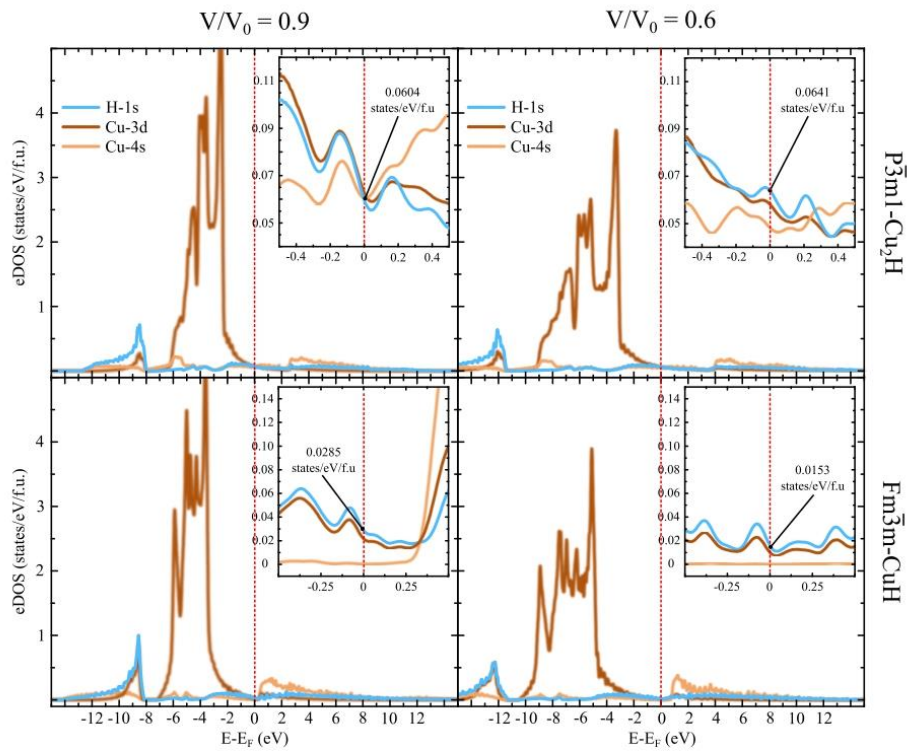


Figure S4: Orbital projected electron density-of-states from DFT-based calculations for both  $\text{Cu}_2\text{H}$  (top) and  $\text{CuH}$  (bottom) at compressions of  $V/V_0 = 0.9$  (left) and  $0.6$  (right). Insets show close-ups of the vicinity around the Fermi energy  $E_F$ .

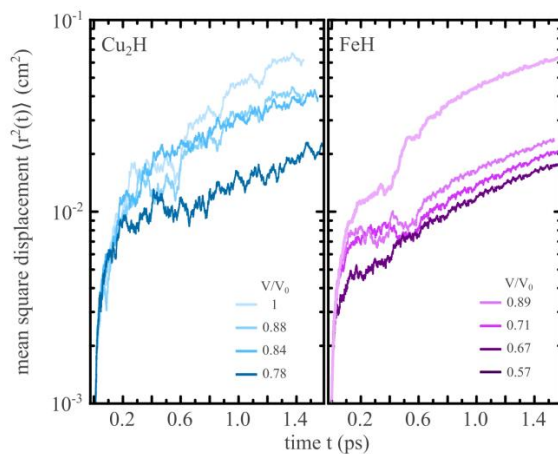


Figure S5: Mean square displacement of hydrogen atoms as a function of time as obtained by means of DFT-based molecular dynamics simulations of  $\text{Cu}_2\text{H}$  and  $\text{FeH}$  at different compressions.

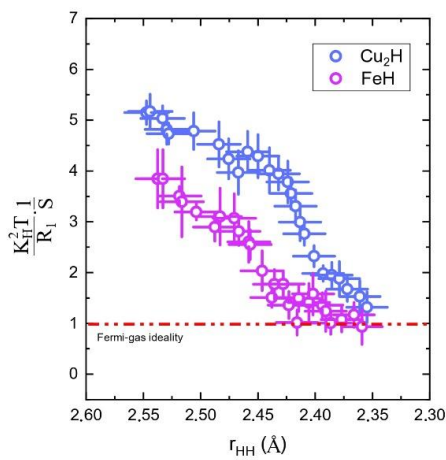


Figure S6: Korrington ratios  $K_H^2 T / R_1 S$  for  $\text{Cu}_2\text{H}$  and  $\text{FeH}$  normalized to the ideal Fermi gas value for hydrogen nuclei ( $S = 0.263 \mu\text{sK}$ ).

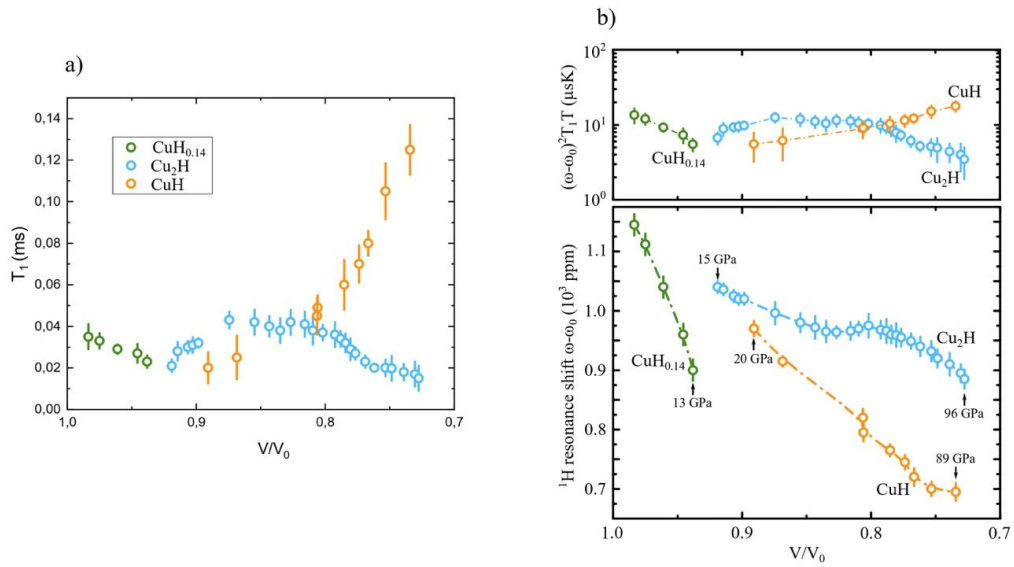


Figure 7: a) Spin lattice relaxation times  $T_1$  of the three copper hydrides synthesized and b) summary of Knight shift data (bottom) as well as Korringa ratios (top) as a function of compression  $V/V_0$  using  $V_0$  from the equations of state given in Table S1).

**Equations of state**

Table S1: Equation of state parameter for pure copper, the three copper hydrides and fcc iron hydride used in the conversion of volumes to pressure in this study.  $V_0$  is the equilibrium volume,  $K_0$  the bulk modulus at zero pressure, and  $K_0'$  its pressure derivative.

	Reference	Space Group	$V_0$ p.f.u ( $\text{\AA}^3$ )	$K_0$ (GPa)	$K_0'$
Cu	[14]	$Fm\bar{3}m$	11.8	135	4.9
CuH	DFT, This study	$Fm\bar{3}m$	14.8	132	4.5
Cu <sub>2</sub> H	[15]	$P\bar{3}m1$	13.1	145	4.8
Cu <sub>2</sub> H	DFT, This study	$P\bar{3}m1$	13.3	138	4.6
CuH <sub>0.65</sub>	[16]	$Fm\bar{3}m$	14.1	145	4.0
FeH	[13]	$Fm\bar{3}m$	13.5	99	11.7

Table S2: Summary of experimental data from diffraction experiments. Pressure ( $P$ ) inside the DAC was determined using the equations of state (EOS) of unreacted copper (Cu), rhenium gasket material (Re) and microdiamonds (Dia) produced during laser heating by the reaction of Cu and paraffin oil. XRD measurements were performed before (Cold) and after heating, and the temperature ( $T$ ) at which each phase was synthesized was measured through multiwavelength spectroradiometry. Copper hydride phases identified and analyzed at each pressure point are reported as Cu<sub>2</sub>H (trigonal phase), CuH<sub>x</sub> (cubic phase, with  $0.5 < x < 1$ ) and CuH (cubic phase, full H occupancy). Their atomic volume per a Cu atom ( $V/Cu$ ) reported in  $\text{\AA}^3$ , are listed in the last column.

Cell	P (GPa)	EOS	T (K)	Phase	$V/Cu$ ( $\text{\AA}^3$ )
GC001	35(1)	Cu	1900(100)	Cu <sub>2</sub> H	11.27(2)
	35(1)	Cu	1900(100)	Cu <sub>2</sub> H	11.35(2)
	58(1)	Cu, Dia	Cold	Cu <sub>2</sub> H	10.53(4)
	58(1)	Cu, Dia	Cold	Cu <sub>2</sub> H	10.42(2)
	58(1)	Cu, Dia	Cold	Cu <sub>2</sub> H	10.44(2)
	58(1)	Cu, Dia	2000(100)	CuH <sub>x</sub>	10.83(2)
	58(1)	Cu, Dia	2000(100)	CuH <sub>x</sub>	10.91(3)
	58(1)	Cu, Dia	2000(100)	CuH <sub>x</sub>	11.11(2)
GC003	94(2)	Dia	Cold	CuH <sub>x</sub>	10.21(3)
	94(2)	Dia	2000(100)	CuH <sub>x</sub>	10.30(6)
	94(2)	Dia	2000(100)	CuH <sub>x</sub>	10.27(4)
	94(2)	Dia	2000(100)	CuH <sub>x</sub>	10.28(3)
	112(2)	Cu, Re	Cold	CuH <sub>x</sub>	9.80(6)
	112(2)	Cu, Re	2000(300)	CuH	10.08(2)
	112(2)	Cu, Re	2000(300)	CuH	10.08(3)
	140(2)	Dia	1800(100)	CuH	9.66(2)
	140(2)	Dia	1800(100)	CuH	9.67(3)
	157(3)	Dia	2000(100)	CuH	9.48(2)
	157(3)	Dia	2000(100)	CuH	9.44(3)
	157(3)	Dia	2000(100)	CuH	9.48(2)
TM003	63(1)	Dia	Cold	Cu <sub>2</sub> H	10.49(6)
	63(1)	Dia	Cold	Cu <sub>2</sub> H	10.49(4)
	63(1)	Dia	1800(200)	CuH <sub>x</sub>	11.33(6)
	63(1)	Dia	1800(200)	CuH	10.90(3)
	63(1)	Dia	1800(200)	CuH	10.82(4)

Table S3: Refinement and crystal structure details of  $\text{Cu}_2\text{H}$  at 35 GPa based on single crystal/powder X-ray diffraction data.

Chemical formula	$\text{Cu}_2\text{H}$
<b>Crystal data</b>	
$M_r$	64.05
Crystal system, space group	Trigonal, $P\bar{3}m1$
Pressure (GPa)	35
$a, c$ ( $\text{\AA}$ )	2.5006(6), 4.1635(15)
$V$ ( $\text{\AA}^3$ )	22.546(14)
$Z$	1
Radiation type	Synchrotron, $\lambda = 0.41134 \text{ \AA}$
$\mu$ ( $\text{mm}^{-1}$ )	45.95
<b>Data collection</b>	
Diffractometer	ID15B@ESRF
Absorption correction	Multi-scan <i>CrysAlis PRO</i> 1.171.38.46 (Rigaku Oxford Diffraction, 2018) Empirical absorption correction using spherical harmonics, implemented in SCALE3 ABSPACK scaling algorithm.
No. of measured, independent and observed [ $I > 2\sigma(I)$ ] reflections	61, 32, 32
$R_{\text{int}}$	0.014
$(\sin \theta/\lambda)_{\text{max}}$ ( $\text{\AA}^{-1}$ )	0.435
<b>Refinement</b>	
$R[F^2 > 2\sigma(F^2)]$ , $wR(F^2)$ , $S$	0.089, 0.227, 1.56
No. of reflections	32
No. of parameters	5
$\Delta\rho_{\text{max}}$ , $\Delta\rho_{\text{min}}$ ( $\text{e \AA}^{-3}$ )	5.94, $-3.02$
<b>Atomic coordinates</b>	
Cu1	(0.6667 0.3333 0.2503(17))
H1 (implied)	(0 0 0)

Table S4: Refinement and crystal structure details of CuH at 112 GPa based on single crystal/powder X-ray diffraction data.

Chemical formula	CuH
<b>Crystal data</b>	
$M_r$	64.55
Crystal system, space group	Cubic, $Fm\bar{3}m$
Pressure (GPa)	112
$a$ (Å)	3.4227(10)
$V$ (Å <sup>3</sup> )	40.10(3)
$Z$	4
Radiation type	Synchrotron, $\lambda = 0.2982\text{Å}$
$\mu$ (mm <sup>-1</sup> )	51.68
<b>Data collection</b>	
Diffractometer	P02.2@PETRA III
Absorption correction	Multi-scan <i>CrysAlis PRO</i> 1.171.38.46 (Rigaku Oxford Diffraction, 2018) Empirical absorption correction using spherical harmonics, implemented in SCALE3 ABSPACK scaling algorithm.
No. of measured, independent and observed [ $I > 2\sigma(I)$ ] reflections	56, 19, 17
$R_{\text{int}}$	0.068
$(\sin \theta/\lambda)_{\text{max}}$ (Å <sup>-1</sup> )	0.528
<b>Refinement</b>	
$R[F^2 > 2\sigma(F^2)]$ , $wR(F^2)$ , $S$	0.070, 0.185, 1.43
No. of reflections	19
No. of parameters	2
$\Delta\rho_{\text{max}}$ , $\Delta\rho_{\text{min}}$ (e Å <sup>-3</sup> )	2.68, -4.07
<b>Atomic coordinates</b>	
Cu1	(0 0 0)
H1 (implied)	(0.5 0 0)





## (Eidesstattliche) Versicherungen und Erklärungen

(§ 9 Satz 2 Nr. 3 PromO BayNAT)

Hiermit versichere ich eidesstattlich, dass ich die Arbeit selbstständig verfasst und keine anderen als die von mir angegebenen Quellen und Hilfsmittel benutzt habe (vgl. Art. 64 Abs. 1 Satz 6 BayHSchG).

(§ 9 Satz 2 Nr. 3 PromO BayNAT)

Hiermit erkläre ich, dass ich die Dissertation nicht bereits zur Erlangung eines akademischen Grades eingereicht habe und dass ich nicht bereits diese oder eine gleichartige Doktorprüfung endgültig nicht bestanden habe.

(§ 9 Satz 2 Nr. 4 PromO BayNAT)

Hiermit erkläre ich, dass ich Hilfe von gewerblichen Promotionsberatern bzw. -vermittlern oder ähnlichen Dienstleistern weder bisher in Anspruch genommen habe noch künftig in Anspruch nehmen werde.

(§ 9 Satz 2 Nr. 7 PromO BayNAT)

Hiermit erkläre ich mein Einverständnis, dass die elektronische Fassung meiner Dissertation unter Wahrung meiner Urheberrechte und des Datenschutzes einer gesonderten Überprüfung unterzogen werden kann.

(§ 9 Satz 2 Nr. 8 PromO BayNAT)

Hiermit erkläre ich mein Einverständnis, dass bei Verdacht wissenschaftlichen Fehlverhaltens Ermittlungen durch universitätsinterne Organe der wissenschaftlichen Selbstkontrolle stattfinden können.

Bayreuth, 25. August 2020,

.....

